

**EFFECT OF UPSTREAM EDGE  
GEOMETRY ON THE TRAPPED MODE  
RESONANCE OF DUCTED CAVITIES**

# Effect of Upstream Edge Geometry on The Trapped Mode Resonance of Ducted Cavities

By

Manar Fadel Mohamed Elsayed, B.Sc., M.Sc.

A Thesis

Submitted to the School of Graduate Studies

In Partial Fulfillment of the Requirements

For the Degree

Master of Applied Science

McMaster University

© Copyright by Manar Elsayed, March 13

Master of Applied Science  
(Mechanical Engineering)

McMaster University  
Hamilton, Ontario

**TITLE:** Effect of Upstream Edge Geometry on the  
Trapped Mode Resonance of Ducted Cavities

**AUTHOR:** Manar Elsayed, B.Sc., M.Sc. (Cairo University)

**SUPERVISOR:** Dr. Samir Ziada

**NUMBER OF PAGES:** xix, 132

# Abstract

This thesis investigates the effect of different passive suppression techniques of different configurations on the flow-excited acoustic resonance of an internal axisymmetric cavity. The flow past the cavity under study can excite acoustical diametral modes. This type of acoustic resonance is observed in many practical applications such as valves installed in steam pipe lines, gas transport system, and combustion engines. An experimental setup of a cavity-duct system has been altered to facilitate the study of the suppression and/or delay of resonance. This is done over the range of Mach number of 0.07-0.4. Three different cavity depths ( $d$ ) have been studied 12.5 mm, 25 mm, and 50 mm deep. For each depth, the cavity length ( $L$ ) is changed from 25 mm to 50 mm. The investigation matrix includes the study of two rounding radii, two chamfer geometries and three different types of spoilers, all located at the leading edge of the cavity. The spoiler types are square toothed, curved and delta spoilers. For each of the examined cavity geometries, a case with no suppression devices installed is tested. This case is considered as the base case. Rounding off cavity edges for both radii has increased the acoustic pressure level. However, it delayed the onset of resonance as a result of the increase of the cavity characteristic length. Chamfering the upstream edge of the cavity delayed the onset of resonance to higher flow velocities. This effect results from increasing the cavity characteristic length which delays the coupling of the shear layer perturbations and the acoustic field. The delay of resonance range as well as the suppression of the excited modes achieved by the chamfer depends on the size of the cavity. The three spoiler configurations examined have proven effectiveness in delaying and suppressing resonance for all cavities throughout the velocity range. The choice of spoiler configuration would depend on cavity size to be effective in suppressing very robust acoustic resonances.

# ACKNOWLEDGEMENTS

First of all praise to God the greatest, the most merciful, the all beneficent, the omniscient, who guided the human to know which he did not know.

First and foremost I offer my sincerest gratitude to my supervisor, Dr Samir Ziada, who has supported me throughout my thesis with his patience and knowledge whilst allowing me the room to work in my own way. I attribute the level of my Masters degree to his encouragement and effort and without him this thesis, too, would not have been completed or written. One simply could not wish for a better or friendlier supervisor. I also thank Michael Bolduc for his efforts for helping me to continue finishing the experimental results. I owe the MSc. Supervisory committee members Dr. Marilyn F. Lightstone and Dr. James S. Cotton my special thanks for their beneficial recommendations and suggestions that appraised me through altering this study.

I would like to thank the technicians of Mechanical Engineering Department at McMaster University, especially Ron Lodewyks, Jim McLaren, JP, Mark Mackenzie, and Joe Verhaeghe for providing their help in building parts needed for my experiment.

Last but the least, I share the credit of my work and gratitude with my husband; my partner, and my love Kareem who helped me learn and understand everything around me. I thank him for his continuous support, love, and care he has given me throughout the years of study. Also, I would like to thank my family; back home, for their love and encouraging words they have given me to overcome the difficulties in my work.

# NOMENCLATURE

$\vec{u}_a$	Acoustic particle velocity vector [m/s]
$\vec{V}$	Mean flow velocity vector [m/s]
$\vec{\omega}$	Vorticity vector [rad/sec]
$a$	spacing between teeth [m]
$c$	Speed of sound [m/s]
$c_p$	Acoustic phase velocity [m/s]
$C_{p_{rms}}$	Pressure coefficient
$d$	Cavity depth [m]
$D$	Main pipe diameter [m]
$f$	Perturbation frequency [Hz]
$g$	width of tooth [m]
$h$	tooth height [m]
$H$	total tooth height [m]
$L$	Cavity length [m]
$\ell$	Length scale, chamfer length [m]
$L_e$	effective cavity length [m]
$m$	diametral mode number
$M$	Mach number
$n$	free shear layer mode number (number of wavelengths)
$N$	number of teeth
$P$	Acoustic pressure amplitude (maximum pressure) [Pa]
$P_0$	total pressure [Pa]
$r$	radius of curvature [m]
$R$	radius of curvature [m]
$r_{down}$	downstream radius of curvature [m]
$r_{up}$	upstream radius of curvature [m]
$t$	pitch [m]
$u'$	fluctuating flow velocity [m/s]
$u_p$	phase velocity [m/s]
$V$	mean flow velocity, jet velocity [m/s]
$W$	Cavity width [m]

$x$	Axial distance [m]
$\mathcal{P}$	Acoustic power generated [N/m]

### **Greek Letters and Symbols**

$\mathcal{V}$	volume [m <sup>3</sup> ]
$\alpha$	spacing between teeth [degree]
$\beta$	width of tooth [degree]
$\delta$	Boundary Layer thickness [m]
$\theta$	angle of inclination (angle of attack) [degree]
$\theta_0$	momentum thickness at the nozzle edge [m]
$\lambda$	Wavelength [m]
$\rho$	air density [kg/m <sup>3</sup> ]
$\varphi$	height of tooth [degree]

# Table of Contents

Abstract.....	iii
Acknowledgements.....	iv
Nomenclature.....	v
List of Figures.....	x
List of Tables.....	xix
CHAPTER 1 Introduction.....	1
1.1 Introduction.....	1
1.2 Thesis outline.....	3
CHAPTER 2 Literature Review.....	4
2.1 Overview of Cavity Oscillations.....	4
2.1.1 Shear Layer Instability.....	5
2.1.2 Impinging shear layers.....	7
2.1.3 Feedback Mechanisms.....	9
2.2 Suppression Methods.....	13
2.2.1 Rounding Cavity Edges.....	14
2.2.2 Chamfering Cavity Edges.....	20
2.2.3 Leading Edge Spoilers.....	25
2.3 Focus of the present research.....	31
CHAPTER 3 Experimental Test Setup.....	33
3.1 Test Facility.....	33
3.2 Test Section.....	35
3.3 Basic Geometry.....	37

3.4	Approach Flow characteristics .....	41
3.5	Characteristics of acoustic-shear layer coupling.....	44
3.6	Suppression seat geometry .....	48
3.6.1	Rounding cavity edges.....	50
3.6.2	Upstream chamfering.....	52
3.6.3	Leading edge spoiler .....	52
3.7	Instrumentation.....	61
3.8	Experimental Procedures and Data Analysis .....	62
CHAPTER 4 Experimental Results.....		64
4.1	One Inch Cavity Depth (d=25mm).....	64
4.1.1	Acoustic response of base geometries B1 (1, 1) and B2 (1, 2).....	65
4.1.2	Rounding the Cavity Edges .....	72
4.1.3	Chamfering Upstream Cavity edge.....	79
4.1.4	Leading Edge Spoilers .....	86
4.1.5	Summary of one inch Cavity depth (d=25mm) .....	91
4.2	Results of Half inch cavity depth (d=12.5mm) .....	91
4.2.1	Base Cases B3 (1/2, 1) and B4 (1/2, 2) .....	92
4.2.2	Suppression devices .....	98
4.2.3	Summary of half inch cavity depth .....	99
4.3	Results of Two Inch cavity depth (d = 50mm).....	101
4.3.1	Base Cases B5 (2, 1) and B6 (2, 2).....	101
4.3.2	Suppression results .....	107
4.3.3	Summary of two inch Cavity depth (d=50mm).....	114
CHAPTER 5 Summary and Conclusions .....		115
5.1	Summary and Conclusions.....	115

5.2	Suggestions for future work.....	118
	References.....	119
	Appendix A-Additional Results .....	124
	Appendix B-Uncertainty Analysis.....	131

# List of Figures

Figure 2-1 Schematic illustrating flow-induced cavity resonance for an upstream turbulent boundary layer. Cattafesta (2008 ).....	5
Figure 2-2 Flow visualization of a plane mixing layer, (Chevray, 1984).....	6
Figure 2-3 Jet large scale structure growth rate for different perturbation Strouhal number: o, Axisymmetric nozzle; x, plane nozzle. (Freymuth, 1966)7	7
Figure 2-4 General features of the self-sustained oscillation of impinging free shear layer (Rockwell, 1983).....	8
Figure 2-5 Strouhal number of the impinging free shear layer oscillation as a function of the dimensionless impinging length (Ziada & Rockwell, 1982).....	9
Figure 2-6 Matrix categorization of fluid-dynamic, fluid-resonant, and fluid-elastic types of cavity oscillations (Rockwell & Naudascher, 1978)10	10
Figure 2-7 Typical amplitude spectra of pressure fluctuations at rear of cavities, where n is the non-dimensional frequency ( $n=fL/V$ ) (Rossiter, 1964).....	11
Figure 2-8 Effect of cavity width and length on amplitude spectra of unsteady pressures; $L/d=4$ , n is non-dimensional frequency ( $n=fL/V$ ) (Rossiter, 1964).....	12
Figure 2-9 Classification of flow control schemes, (Cattafesta et al., 2003).....	14
Figure 2-10 Effect of cavity geometry on attenuation of fluid dynamic oscillations as depicted by variation of fluctuating pressure coefficient ( $C_{p_{rms}}$ ) versus cavity length to depth ratio (Ethembaoglu, 1973).....	15
Figure 2-11 Influence of the radius of curvature of the edges on the amplitude of pulsations in a single side branch set-up, Square pipe $L=0.06m$ , $\text{---}r=0$ , $\text{- - -}r=6mm$ , $\text{- . . -}r=12mm$ (Bruggeman et al., 1991).....	16

Figure 2-12 Comparison of Strouhal number versus flow velocity with $L/d=1$ for four edge geometries (a) based on gap length and (b) based on modified gap length, $I$ is the distance of the constant diameter pipe between two cavities, (Nakiboglu et al., 2009 ) .....	18
Figure 2-13 Dimensionless pressure fluctuation amplitude for the 3rd acoustic mode as a function of Strouhal number for round upstream–sharp downstream case and sharp upstream–round downstream case (Nakiboglu et al., 2010).....	19
Figure 2-14 Influence of the radius of curvature of the edges on the amplitude of pulsations in a double side branch set-up, ____Rounded edges, - - - First T-joint sharp edges, - . - . -Second T-joint sharp edges (Bruggeman et al., 1991).....	19
Figure 2-15 Rounding valve seats in gate valves (a) rounding edge only, (b) and (c) combined upward ramp and rounding edge (Smith & Loluff, 2000).....	20
Figure 2-16 Effect of double ramp on attenuation in shallow cavity oscillations (Franke & Carr, 1975).....	21
Figure 2-17 Pressure pipe spectra measured with (a) reference valve and (b) 15° chamfer up- and downstream the cavity, $q$ is the dynamic pressure in the throat valve (Smith & Loluff, 2000).....	22
Figure 2-18 Normalized acoustic response for Seat Design of 13° chamfer angle, 8 mm depth (Janzen et al., 2007).....	24
Figure 2-19 Normalized acoustic response for Seat Design of 17.3° chamfer angle, 19.2% chamfer length to cavity length (Janzen et al., 2007). .	24
Figure 2-20 Compound chamfer design (Janzen et al., 2007) .....	25
Figure 2-21(a) Cavity with leading edge spoiler and trailing edge ramp configuration, (b) Comparisons of spectra of configurations with and without suppressors for 1.2 Mach number and 30000 ft altitude, ---- basic cavity, ____cavity with spoiler and ramp (Shaw, 1979).....	26

Figure 2-22 Configuration of vertical and flap type spoilers, (a) Sawtooth spoiler, coarse pitch, (b) Sawtooth spoiler, fine pitch, (c) Solid spoiler (fence), and (d) Flap-type spoiler, (Dix & Bauer, 2000).....	28
Figure 2-23 Two locations where the spoilers mounted, (Dix & Bauer, 2000).....	29
Figure 2-24 Sketch of leading edge spoiler tested with cavity $L/d=1$ , (Rossiter, 1964).....	29
Figure 2-25 Configuration of spoilers, (Bruggeman et al., 1991) .....	30
Figure 2-26 Influence of pressure $p_0$ on the performance of spoilers and sharp edges (vortex damping); (a) Reference measurements with rounded edges; (b) spoiler no. 1 upstream of the first side branch; (c) spoiler no. 3 upstream of the first side branch; (d) spoiler no. 3 upstream of the second side branch; (e) spoiler no. 2 upstream of the second side branch (Bruggeman et al., 1991). .....	30
Figure 3-1 Schematic of the test facility (Aly, 2008) .....	34
Figure 3-2 Schematic of the diffuser design (Aly, 2008) .....	36
Figure 3-3 (a) Schematic drawing of the test section showing the inlet bell-mouth and the axisymmetric cavity-duct system (Aly, 2008), (b) Dimensions of the axisymmetric cavity .....	38
Figure 3-4 Schematic drawing of the cavity design with base seat installed, cavity depth is 25 mm and cavity length is 50 mm. ....	40
Figure 3-5 Spacer-ring with base seat in place used to help fit aluminum seats in deeper cavity.....	41
Figure 3-6 At reference velocity of 31 m/s, the radial profile of mean velocity at upstream edge of the cavity and at the end of the bell mouth (Aly, 2008).....	42
Figure 3-7 Radial distribution of the dimensionless RMS amplitude of fluctuation velocity at the cavity upstream edge for reference velocity of 31 m/s at the end of the bell mouth (the continuous line is a moving average of the measurement data), (Aly, 2008).....	43

Figure 3-8 The mode shapes of the first, second and third acoustic resonance modes. $L/d=1$ , $d/D=2/12$ (Aly, 2008).....	46
Figure 3-9 Axial distribution of acoustic pressure decay of the first diamteral mode for various cavity dimensions, $m$ is the acoustic mode order, $x$ is measured from the cavity center, (Aly, 2008) .....	47
Figure 3-10 Different configurations of the cavity leading edge, (a) sharp edge (base case), (b) rounded edge, (c) chamfer, (d) spoiler .....	49
Figure 3-11 Schematic drawing of the saw-toothed spoiler, all dimensions in mm .....	50
Figure 3-12 Rounded edges seat with radius of curvature of 5mm, all dimensions in mm.....	51
Figure 3-13 Rounded edges seat with radius of curvature of 10mm, all dimensions in mm.....	51
Figure 3-14 Chamfer seat with chamfer length of 4.88mm, all dimensions in mm .....	53
Figure 3-15 Chamfer seat with chamfer length of 9.75mm, all dimensions in mm .....	53
Figure 3-16 Detailed drawing of Spoiler (1), all dimensions in mm .....	55
Figure 3-17 Altered aluminum seat to fit spoiler.....	55
Figure 3-18 Detailed drawing of Spoiler (2), all dimensions in mm .....	56
Figure 3-19 Detailed drawing of Spoiler (3), all dimensions in mm .....	57
Figure 3-20 Detailed drawing of Spoiler (4), all dimensions in mm .....	57
Figure 3-21 (a) Detailed drawing of Curved Spoiler, (b) Tooth details of spoiler, all dimensions in mm.....	58
Figure 3-22 Detailed drawing of Delta Spoiler, all dimensions in mm .....	59
Figure 3-23 Photographs of (a) Curved spoiler and (b) Delta spoiler .....	59
Figure 3-24 Location of pressure transducers, (Aly, 2008) .....	62

Figure 4-1 Acoustic pressure spectrum for cavity $L/d= 1$ , $d/D=2/12$ at different flow velocities, $f_n$ is the frequency of mode $m$ .	66
Figure 4-2 Pressure amplitudes of excited acoustic modes at different flow velocities for base case B1 (1, 1), $d=25\text{mm}$ , $L/d=1$ , $d/D=2/12$	68
Figure 4-3 Frequency of excited acoustic modes at different flow velocities for base case B1 (1, 1), $d=25\text{mm}$ , $L/d=1$ , $d/D=2/12$	68
Figure 4-4 Pressure amplitudes of excited acoustic modes at different flow velocities for base case B2 (1, 2), $d=25\text{mm}$ , $L/d=2$ , $d/D=2/12$	69
Figure 4-5 Frequency of excited acoustic modes at different flow velocities for base case B2 (1, 2), $d=25\text{mm}$ , $L/d=2$ , $d/D=2/12$	69
Figure 4-6 Dimensionless acoustic pressures ( $P/\frac{1}{2}\rho V^2$ ) versus Strouhal number ( $St=f L/V$ ) for base case B1 (1, 1), $d=25\text{mm}$ , $L/d=1$ , $d/D=2/12$	71
Figure 4-7 Dimensionless acoustic pressures ( $P/\frac{1}{2}\rho V^2$ ) versus reduced velocity ( $V_r =V/f L$ ) for base case B1 (1, 1), $d=25\text{mm}$ , $L/d=1$ , $d/D=2/12$	71
Figure 4-8 Dimensionless acoustic pressures ( $P/\frac{1}{2}\rho V^2$ ) versus reduced velocity ( $V_r =V/f L$ ) for base case B2 (1, 2), $d=25\text{mm}$ , $L/d=2$ , $d/D=2/12$	72
Figure 4-9 Pressure amplitudes of excited acoustic modes at different flow velocities, $d=25\text{mm}$ , $L/d=1$ , $d/D=2/12$ , $r/L=0.2$	74
Figure 4-10 Frequency of excited acoustic modes at different flow velocities, $d=25\text{mm}$ , $L/d=1$ , $d/D=2/12$ , $r/L=0.2$	74
Figure 4-11 Dimensionless acoustic pressures ( $P/\frac{1}{2}\rho V^2$ ) versus reduced velocity ( $V_r =V/f L$ ), $d=25\text{mm}$ , $L/d=1$ , $d/D=2/12$ , $r/L=0.2$	76
Figure 4-12 Influence of rounding cavity edges on pressure amplitudes of excited acoustic modes at different flow velocities, $d=25\text{mm}$ , $L/d=1$ , $d/D=2/12$ ; ___ base, ----- rounding	76
Figure 4-13 Influence of rounding cavity edges on dimensionless pressure ( $P/\frac{1}{2}\rho V^2$ ) amplitudes of excited acoustic modes against reduced velocity ( $V_r =V/f L$ ), $d=25\text{mm}$ , $L/d=1$ , $d/D=2/12$ ; ___ base, ----- rounding	78

- Figure 4-14 Influence of rounding cavity edges on dimensionless pressure ( $P/\frac{1}{2}\rho V^2$ ) amplitudes of excited acoustic modes against reduced velocity ( $V_r = V/fL_e$ ),  $L_e = L + r$ ,  $d=25\text{mm}$ ,  $L/d=1$ ,  $d/D=2/12$ , \_\_\_ base, ---- rounding..... 78
- Figure 4-15 Influence of upstream chamfer on pressure amplitudes of excited acoustic modes at different flow velocities,  $d=25\text{mm}$ ,  $L/d=1$ ,  $d/D=2/12$ , \_\_\_ base, - - - chamfer..... 81
- Figure 4-16 Influence of upstream chamfer on pressure amplitudes of excited acoustic modes at different flow velocities,  $d=25\text{mm}$ ,  $L/d=2$ ,  $d/D=2/12$ , \_\_\_ base, - - - chamfer..... 81
- Figure 4-17(a) Influence of long chamfer on pressure amplitudes of excited acoustic modes at different flow velocities,  $d=25\text{mm}$ ,  $L/d=1$ ,  $d/D=2/12$ , \_\_\_ base, - - - chamfer (b) Influence of long and short chamfer on dimensionless pressure ( $P/\frac{1}{2}\rho V^2$ ) amplitudes of excited acoustic modes against reduced velocity ( $V_r = V/fL_e$ ),  $L_e = L + r$ ,  $d=25\text{mm}$ ,  $L/d=1$ ,  $d/D=2/12$ , Base case, X short chamfer, Long chamfer ..... 83
- Figure 4-18(a) Influence of short chamfer on pressure amplitudes of excited acoustic modes at different flow velocities,  $d=25\text{mm}$ ,  $L/d=2$ ,  $d/D=2/12$ , \_\_\_ base, - - - chamfer, (b) Influence of long and short chamfer on dimensionless pressure ( $P/\frac{1}{2}\rho V^2$ ) amplitudes of excited acoustic modes against reduced velocity ( $V_r = V/fL_e$ ),  $L_e = L + r$ ,  $d=25\text{mm}$ ,  $L/d=2$ ,  $d/D=2/12$ , Base case, X short chamfer, Long chamfer ..... 85
- Figure 4-19 Influence of spoiler (1) on pressure amplitudes of excited acoustic modes at different flow velocities,  $d=25\text{mm}$ ,  $L/d=1$ ,  $d/D=2/12$ , \_\_\_ base, - - - spoiler ..... 89
- Figure 4-20 Influence of spoiler (1) on pressure amplitudes of excited acoustic modes at different flow velocities,  $d=25\text{mm}$ ,  $L/d=2$ ,  $d/D=2/12$ , \_\_\_ base, - - - spoiler ..... 89

Figure 4-21 Influence of spoiler (2) on pressure amplitudes of excited acoustic modes at different flow velocities, $d=25\text{mm}$ , $L/d=1$ , $d/D=2/12$ , ___base, - - - spoiler .....	90
Figure 4-22 Influence of spoiler (2) on pressure amplitudes of excited acoustic modes at different flow velocities, $d=25\text{mm}$ , $L/d=2$ , $d/D=2/12$ , ___base, - - - spoiler .....	90
Figure 4-23 Pressure amplitudes of excited acoustic modes at different flow velocities for base case B3 (12, 1), $d=12.5\text{mm}$ , $L/d=2$ , $d/D=1/12$ ...	95
Figure 4-24 Frequency of excited acoustic modes at different flow velocities for base case B3 (12, 1), $d=12.5\text{mm}$ , $L/d=2$ , $d/D=1/12$ .....	95
Figure 4-25 Pressure amplitudes of excited acoustic modes at different flow velocities for base case B4 (12, 2), $d=12.5\text{mm}$ , $L/d=4$ , $d/D=1/12$ ...	96
Figure 4-26 Frequency of excited acoustic modes at different flow velocities for base case B4 (12, 2), $d=12.5\text{mm}$ , $L/d=4$ , $d/D=1/12$ .....	96
Figure 4-27 Dimensionless acoustic pressures ( $P/\frac{1}{2}\rho V^2$ ) versus reduced velocity ( $V_r = V/f L$ ) for base case B3 (12, 1), $d=12.5\text{mm}$ , $L/d=2$ , $d/D=1/12$	97
Figure 4-28 Dimensionless acoustic pressures ( $P/\frac{1}{2}\rho V^2$ ) versus reduced velocity ( $V_r = V/f L$ ) for base case B4 (12, 2), $d=12.5\text{mm}$ , $L/d=4$ , $d/D=1/12$	97
Figure 4-29 Influence of chamfer on pressure amplitudes of excited acoustic modes at different flow velocities, $d=12.5\text{mm}$ , $L/d=4$ , $d/D=1/12$ , ___base, - - - chamfer .....	100
Figure 4-30 Influence of spoiler (3) on pressure amplitudes of excited acoustic modes at different flow velocities, $d=12.5\text{mm}$ , $L/d=4$ , $d/D=1/12$ , ___base, - - - spoiler .....	100
Figure 4-31 Pressure amplitudes of excited acoustic modes at different flow velocities for base case B5 (2, 1), $d=50\text{mm}$ , $L/d=0.5$ , $d/D=4/12$ ...	104
Figure 4-32 Frequency of excited acoustic modes at different flow velocities for base case B5 (2, 1), $d=50\text{mm}$ , $L/d=0.5$ , $d/D=4/12$ .....	104

Figure 4-33 Pressure amplitudes of excited acoustic modes at different flow velocities for base case B6 (2, 2), $d=50\text{mm}$ , $L/d=1$ , $d/D=4/12$ .....	105
Figure 4-34 Frequency of excited acoustic modes at different flow velocities for base case B6 (2, 2), $d=50\text{mm}$ , $L/d=1$ , $d/D=4/12$ .....	105
Figure 4-35 Dimensionless acoustic pressures ( $P/\frac{1}{2}\rho V^2$ ) versus reduced velocity ( $V_r = V/fL$ ) for base case B5 (2, 1), $d=50\text{mm}$ , $L/d=0.5$ , $d/D=4/12$ .	106
Figure 4-36 Dimensionless acoustic pressures ( $P/\frac{1}{2}\rho V^2$ ) versus reduced velocity ( $V_r = V/fL$ ) for base case B6 (2, 2), $d=50\text{mm}$ , $L/d=1$ , $d/D=4/12$ ....	106
Figure 4-37 Influence of chamfer on pressure amplitudes of excited acoustic modes at different flow velocities, $d=50\text{mm}$ , $L/d=1$ , $d/D=4/12$ , ___base, - - - chamfer .....	109
Figure 4-38 Influence of spoiler (4) on pressure amplitudes of excited acoustic modes at different flow velocities, $d=50\text{mm}$ , $L/d=1$ , $d/D=4/12$ , ___base, - - - spoiler .....	109
Figure 4-39 Influence of curved spoiler on pressure amplitudes of excited acoustic modes at different flow velocities, $d=50\text{mm}$ , $L/d=0.5$ , $d/D=4/12$ , ___base, - - - spoiler .....	111
Figure 4-40 Influence of curved spoiler on pressure amplitudes of excited acoustic modes at different flow velocities, $d=50\text{mm}$ , $L/d=1$ , $d/D=4/12$ , ___base, - - - spoiler .....	111
Figure 4-41 Influence of delta spoiler on pressure amplitudes of excited acoustic modes at different flow velocities, $d=50\text{mm}$ , $L/d=0.5$ , $d/D=4/12$ , ___base, - - - spoiler .....	113
Figure 4-42 Influence of delta spoiler on pressure amplitudes of excited acoustic modes at different flow velocities, $d=50\text{mm}$ , $L/d=1$ , $d/D=4/12$ , ___base, - - - spoiler .....	113
Figure A-1 Pressure amplitudes of excited acoustic modes at different flow velocities, $d=25\text{mm}$ , $L/d=2$ , $d/D=2/12$ , $r/L=0.2$ .....	124
Figure A-2 Frequency of excited acoustic modes at different flow velocities, $d=25\text{mm}$ , $L/d=2$ , $d/D=2/12$ , $r/L=0.2$ .....	124

Figure A-3 Dimensionless acoustic pressures ( $P/\frac{1}{2}\rho V^2$ ) versus reduced velocity ( $V_r = V/fL$ ), $d=25\text{mm}$ , $L/d=2$ , $d/D=2/12$ , $r/L=0.2$ .....	125
Figure A-4 Influence of rounding cavity edges on pressure amplitudes of excited acoustic modes at different flow velocities, $d=25\text{mm}$ , $L/d=2$ , $d/D=2/12$ ; ___ base, ---- rounding .....	125
Figure A-5 Pressure amplitudes of excited acoustic modes at different flow velocities, $d=25\text{mm}$ , $L/d=2$ , $d/D=2/12$ , $r/L=0.1$ .....	126
Figure A-6 Frequency of excited acoustic modes at different flow velocities, $d=25\text{mm}$ , $L/d=2$ , $d/D=2/12$ , $r/L=0.1$ .....	126
Figure A-7 Dimensionless acoustic pressures ( $P/\frac{1}{2}\rho V^2$ ) versus reduced velocity ( $V_r = V/fL$ ), $d=25\text{mm}$ , $L/d=2$ , $d/D=2/12$ , $r/L=0.1$ .....	127
Figure A-8 Influence of rounding cavity edges on pressure amplitudes of excited acoustic modes at different flow velocities, $d=25\text{mm}$ , $L/d=2$ , $d/D=2/12$ ; ___ base, ---- rounding .....	127
Figure A-9 Influence of rounding cavity edges on dimensionless pressure ( $P/\frac{1}{2}\rho V^2$ ) amplitudes of excited acoustic modes against reduced velocity ( $V_r = V/f L_e$ ), $L_e = L + r$ , $d=25\text{mm}$ , $L/d=2$ , $d/D=2/12$ , ___ base, ---- rounding .....	128
Figure A-10 Influence of rounding cavity edges on dimensionless pressure ( $P/\frac{1}{2}\rho V^2$ ) amplitudes of excited acoustic modes against reduced velocity ( $V_r = V/f L_e$ ), $L_e = L + r$ , $d=25\text{mm}$ , $L/d=2$ , $d/D=2/12$ , ___ base, ---- rounding .....	128
Figure A-11 Influence of chamfer on pressure amplitudes of excited acoustic modes at different flow velocities, $d=12.5\text{mm}$ , $L/d=2$ , $d/D=1/12$ , ___ base, - - - chamfer .....	129
Figure A-12 Influence of spoiler (3) on pressure amplitudes of excited acoustic modes at different flow velocities, $d=12.5\text{mm}$ , $L/d=2$ , $d/D=1/12$ , ___ base, - - - spoiler .....	129
Figure A-13 Influence of chamfer on pressure amplitudes of excited acoustic modes at different flow velocities, $d=50\text{mm}$ , $L/d=0.5$ , $d/D=4/12$ , ___ base, - - - chamfer .....	130
Figure A-14 Influence of spoiler (4) on pressure amplitudes of excited acoustic modes at different flow velocities, $d=50\text{mm}$ , $L/d=0.5$ , $d/D=4/12$ , ___ base, - - - spoiler .....	130

# List of Tables

Table 3-1 Dimensions of tested cavities .....	40
Table 3-2 List of displacement thickness, momentum thickness, shape factor, and boundary layer thickness at different flow velocities (Aly, 2008) .....	43
Table 3-3 Dimensions of the square-toothed spoiler .....	50
Table 3-4 Suppression devices tested in different cavity dimensions.....	60

# CHAPTER 1

## Introduction

---

### 1.1 Introduction

Flow past a cavity-like geometry activates diversity of flow oscillation phenomena. For instance, self-sustained tones, acoustic resonance, and powerful noise generation can be generated by flow over cavities. The general sequence of noise generation process starts with the shear layer instability causing small vorticity perturbations at the leading edge of the cavity to amplify as they travel downstream with the flow. These magnified vorticity perturbations impinge on the cavity downstream corner where the feedback phenomenon closes the excitation mechanism cycle by creating new perturbations at the cavity upstream corner.

Cavity oscillations are categorized according to the nature of the feedback phenomenon that activates the self-sustained oscillation. Rockwell and Naudascher (1978) classified this excitation mechanism into three categories: 1) fluid-dynamic in which the pressure pulse at the downstream edge travel upstream to generate new vortical perturbations at the upstream edge 2) fluid-resonant where resonant acoustic waves (standing waves) close the feedback loop and 3) fluid-elastic where oscillations are combined with the motion of solid boundary to close the feedback loop.

The large-amplitude pressure oscillation originating from the flow over cavities in a diversity of practical applications is the reason behind the endless work to find different methodologies to suppress this type of oscillation. These amplitudes can cause structural damage or generate severe noise levels. Some practical examples of such problems are experienced in aircrafts, jet engines,

rockets, piping systems, and control valves. Krishnamurty (1955) was among the first to improve our understanding and controlling the flow over cavities. Because of its importance to aero-acoustical applications, cavity aero-acoustics have been of interest in the aerospace field since the 1950s.

The general objective of controlling is to diminish in a way the flow unsteadiness. The particular purpose of what defines an *effective control* is application dependent. In cases where one or more distinct tones are dominating the background level, suppression of these tones is generally appropriate. But in other applications where the broadband noise is analogous to tonal amplitudes, the reduction in the overall noise levels is needed. Techniques to eliminate cavity oscillations can be classified in various ways. Cattafesta (2008 ) categorized these techniques into two groups, active and passive control. In active control, an external energy input is used to an accommodating actuator to control the flow. The second group, passive control of cavity oscillations is achieved via geometric adjustments using, for an instance, fences, spoilers, ramps, and a passive bleed system. This study is concerned with passive control of an internal axisymmetric cavity oscillation.

The internal axisymmetric cavity under study can excite acoustical diametral modes. These diametral modes are classified as trapped modes. The accompanied acoustic pressure level decays exponentially with axial distance away from the cavity. This type of acoustic resonance is observed in valves installed in steam pipe lines. Three different passive suppression techniques of different configurations are tested. These techniques are rounding off the cavity edges, chamfering the cavity upstream edge, and leading edge spoilers. An experimental setup of a cavity-duct system has been altered to facilitate the study of the suppression techniques over the range of Mach number of 0.07-0.4. Three different cavity depths ( $d$ ) have been investigated; which are 12.5mm (half inch deep), 25mm (one inch deep), and 50mm (two inch deep). The three depths corresponds to cavity depth ( $d$ ) to pipe diameter ( $D$ ) ratios of 1/12, 2/12 & 4/12, respectively. For each depth, the cavity length ( $L$ ) was changed from 25 mm (one inch) to 50mm (two inch) with 25 mm step change. The equivalent aspect ratio of the tested cavities ranged from  $L/d=0.5$  to 4. The characteristics of the upstream

boundary layer have been previously determined by Aly (2008) using a hotwire anemometer.

The acoustic response has been measured using four pressure transducers flush mounted on the cavity floor. The transducers are arranged in a way to ensure that the maximum pressure amplitude is captured. The mean flow velocity is measured at the entrance of the test section using Pitot tube. For each of the examined cavity geometry, a case with no suppression devices installed is tested. This case is referred to in the rest of the thesis as base case. The results of the base case are used as a reference to determine the level and the nature of suppression achieved by each suppression device under investigation.

## **1.2 Thesis outline**

This thesis consists of five chapters and two appendixes. In Chapter 2, the literature review on cavity oscillations, shear layer instability, impinging shear layer, feedback mechanisms, and different suppression methods are reviewed. In Chapter 3, the experimental setup and the measurement techniques used in this research are described. The experimental results relating to the suppression and/or delay of the excited diametral modes and the effect of cavity depth and length on the suppression process are presented and analyzed in Chapter 4. In Chapter 5, the summary and the conclusions of this work as well as some recommendations for future work are provided. Appendix A contains additional experimental results referred to in the text. Appendix B includes the error and uncertainty analysis of instrumentation.

# CHAPTER 2

## Literature Review

---

Lots of research addressed flow over cavities from different aspects. The science of cavity oscillations and means of attenuating pressure fluctuations and noise generation were among researchers interest. Flows over cavities appears in various applications, extending from landing-gear and weapons bays in aircraft (Shaw 1979) to flow in gas transport systems (Bruggeman et al., 1991), control valves (Smith & Loluff, 2000), and internal combustion engine (Knotts & Selamet, 2003).

### **2.1 Overview of Cavity Oscillations**

Before exploring the literature about different suppression methods, this section exemplifies the basic concept of cavity oscillations and the sequence of events that constitute the cavity oscillation phenomena. Section 2.1.1 details briefly the behavior of impinging free shears. The general characteristics of impinging shear flows are summarily reviewed in section 2.1.2. Section 2.1.3 describes characteristics of the cavity feedback mechanism.

Over the years diversity of studies including analytical, computational, and experimental, demonstrated that flow over cavity generates acute pressure fluctuations within and around the cavity. A feedback excitation mechanism sustains these cavity oscillations, and depends on the nature of the system oscillation. The cycle begins with the shear layer instability causing small vorticity perturbations at the leading edge of the cavity. These vorticity perturbations grow rapidly as they travel downstream with the flow. Figure 2-1 shows that when the amplified vorticity perturbations reach the cavity downstream corner, the feedback phenomenon closes the excitation mechanism

cycle. The closure of this cycle is by generating new perturbations at the cavity upstream corner. Cavity oscillations are classified according to the nature of the feedback phenomenon that triggers the self-sustained oscillation. Rockwell and Naudascher (1978) classified this excitation mechanism into three categories: 1) fluid-dynamic, 2) fluid-resonant, and 3) fluid-elastic oscillation.

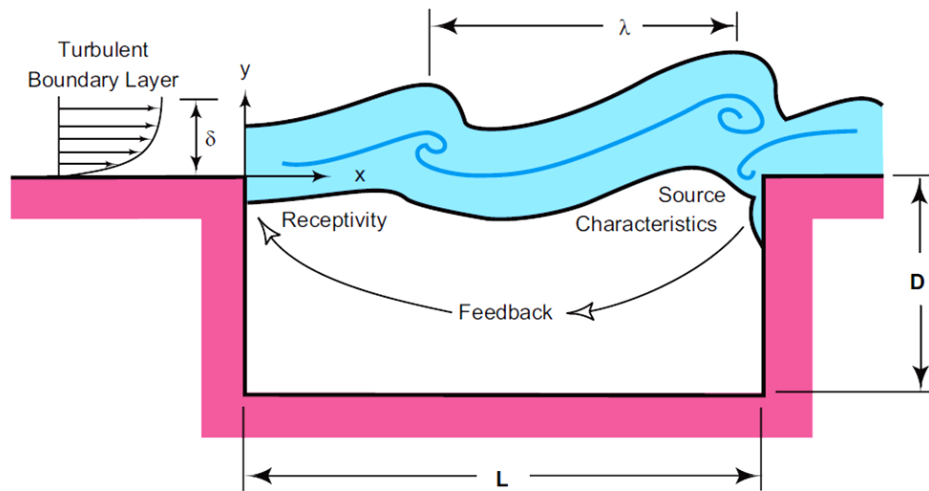
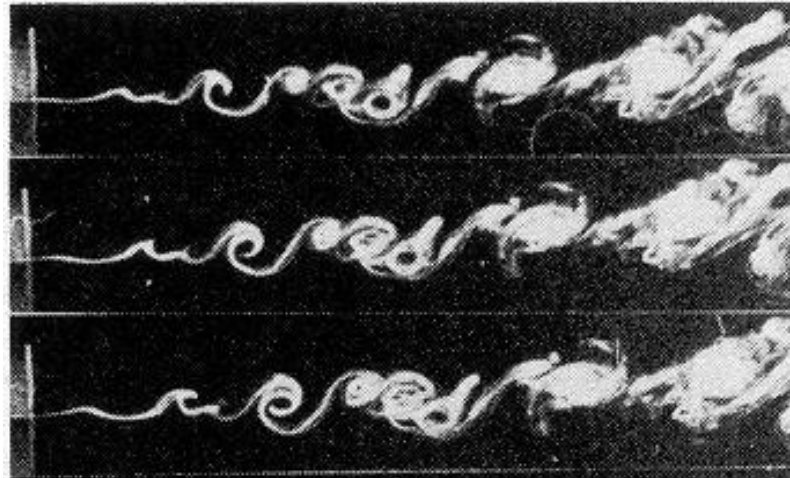


Figure 2-1 Schematic illustrating flow-induced cavity resonance for an upstream turbulent boundary layer. Cattafesta (2008 )

### 2.1.1 Shear Layer Instability

In this section, the general characteristics of the free shear layer are presented. This is done by elaborating on the behavior of the impinging free shear layer which is categorized as the fluid dynamic mechanism of cavity oscillations.

When two aligned flows of different velocities amalgamate, a free shear layer is established between them. Examples of this flow are mixing layers, jets, and wakes. Inherently unstable flow is the main characteristic of free shear layer. The capability of small perturbations in the flow to amplify and form larger vertical structure defines the flow instability. Three snap shots of flow visualization of a plane mixing layer are shown in figure 2-2. These shots are in consecutive order in time. They show how a perturbation grows and evolve moving downstream.



**Figure 2-2 Flow visualization of a plane mixing layer, (Chevray, 1984).**

Rayleigh (1880) formulated the inviscid stability theory that precisely estimates the frequency range for unstable free shear layer. Freymuth (1966) conducted a comparison between experiments on laminar axisymmetric jet of an externally controlled perturbation and the spatial stability theory. The comparison is shown in figure 2-3 for different Strouhal numbers. The Strouhal number,  $St$  ( $St = f\theta_0/V$ ), is based on the perturbation frequency,  $f$ , the momentum thickness of the boundary layer at the nozzle edge,  $\theta_0$ , and the jet velocity,  $V$ . The figure shows for  $St < 0.012$  a good agreement between the spatial theory and the experiment. In addition, the figure shows a better agreement with the curve of temporal growing disturbances for higher values of Strouhal number. The maximum growth rate corresponds to a Strouhal number of 0.0167.

Nonlinear effects were found to be crucial by Miksad (1972) in the evolution of mixing layer when the amplitude of the fundamental component reaches 3.5% of the mean velocity. The harmonic modes were defined as unstable waves of the basic flow. The generation of harmonic, subharmonic and 1.5-harmonics was also documented. Their amplitudes were about one order of magnitude lower than the fundamental frequency amplitude, and they die fast right after approaching the maximum value.

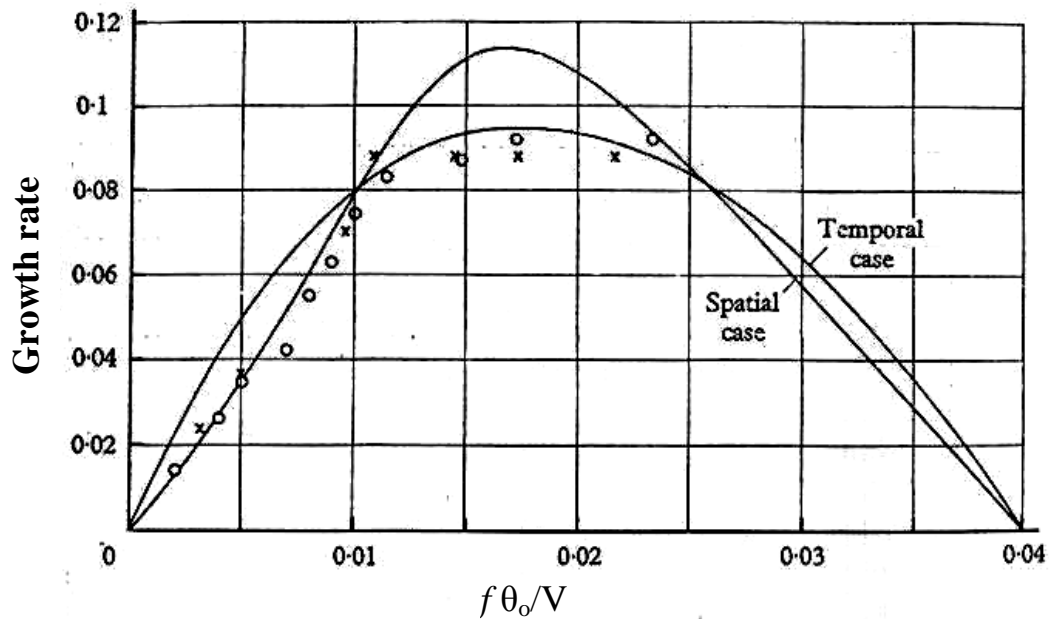
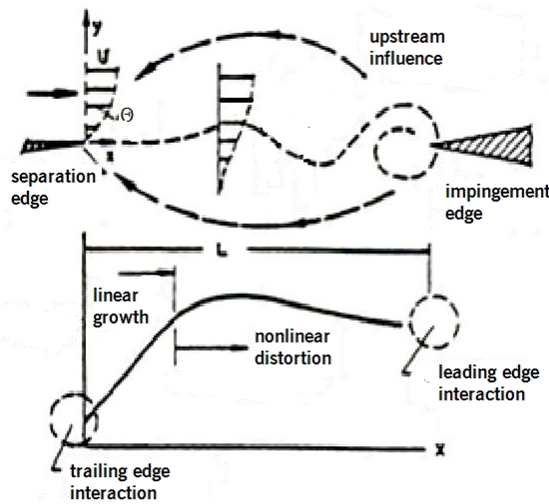


Figure 2-3 Jet large scale structure growth rate for different perturbation Strouhal number: o, Axisymmetric nozzle; x, plane nozzle. (Freymuth, 1966)

## 2.1.2 Impinging shear layers

The capability of maintaining an average level of systematized oscillations is a distinct feature of impinging shear layers. These types of flows have shown their reliance on geometrical and hydrodynamic parameters. In this part of the chapter, the overall features of impinging shear flows are briefly discussed.

Rockwell (1983) has shown that the mechanism generating the impinging of shear layer oscillations consists of series of actions. The series begins with the impingement of the free shear layer vortex structure upon a downstream surface. Upon impingement, a pressure pulse is produced and propagates upstream. At the free shear layer separation edge, this pulsation perturbs the shear layer forcing it to oscillate. As the shear layer advances downstream, the initial perturbation grows and forms a new vortex. These sequences of events compose the self-excitation mechanism which creates and sustains the shear layer oscillations.



**Figure 2-4 General features of the self-sustained oscillation of impinging free shear layer (Rockwell, 1983)**

The length and velocity scales of impinging shear layers are controlling parameters in determining the frequency of the self-sustained oscillation. The distance between the separation and impingement defines the length scale. While the hydrodynamic wave phase velocity is estimated to be the velocity scale. A delay time is considered for sonic flows. The delay time is defined as the time taken for the pressure wave to travel upstream. Tam (1974) suggested the following formula to estimate the oscillation frequency:

$$\frac{\ell}{u_p} + \frac{\ell}{c} = \frac{n}{f} \quad 2-1$$

where,  $\ell$ , is the aforementioned length scale and  $u_p$  is the phase velocity,  $c$  is the speed of sound associated with the traveling pressure wave,  $f$  is the oscillation frequency, and  $n= 1,2,\dots$  represents the number of wavelengths existing between the separation and impinging edges.

The number of wavelengths ( $n$ ) occurring between the separation and the impinging edges of mixing layer has been investigated by Ziada and Rockwell (1982). Upon changing the distance between the separation and the impinging edges, they found that the oscillation adapts its frequency to fit two things. The

first one is maintaining the phase difference between the velocity fluctuations at separation and impingement fulfilling the relation  $2n\pi$ . Secondly, the frequency is retained around specific range where the most amplified free shear layer natural frequency exists. Figure 2-5 shows a stepwise trend of frequency of oscillations conforming to these circumstances.

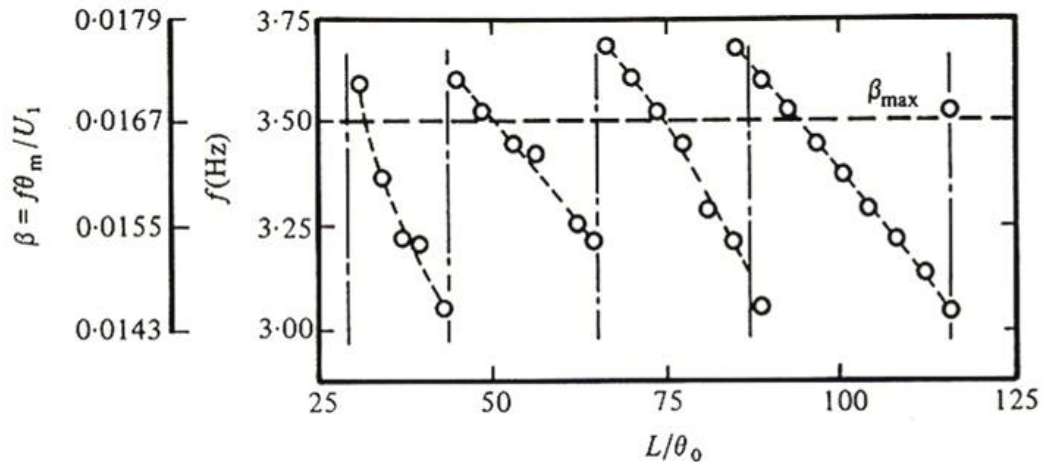


Figure 2-5 Strouhal number of the impinging free shear layer oscillation as a function of the dimensionless impinging length (Ziada & Rockwell, 1982)

### 2.1.3 Feedback Mechanisms

The type of cavity oscillation depends on the nature of the upstream feedback. The categories are 1) fluid-dynamic where oscillations originate from inherent instability of the flow 2) fluid-resonant where oscillations are influenced by resonant wave effects (standing waves) and 3) fluid-elastic where oscillations are coupled with the motion of solid boundary (Rockwell & Naudascher, 1978). Examples of these three types of cavity oscillations are shown in figure 2-6.

Most of previous studies focused on the fluid dynamic oscillations more than fluid resonant oscillation. However, some researchers took the findings of the work done in fluid dynamic and accommodated the data for fluid resonant cavity oscillations. These include methods of estimating the frequency of cavity oscillations or the range of Strouhal number that defines the shear layer modes

(Rossiter (1964) and Tam & Block (1978)). In the following, the literature about fluid resonant oscillations is briefly reviewed as it constitutes the core of this study.

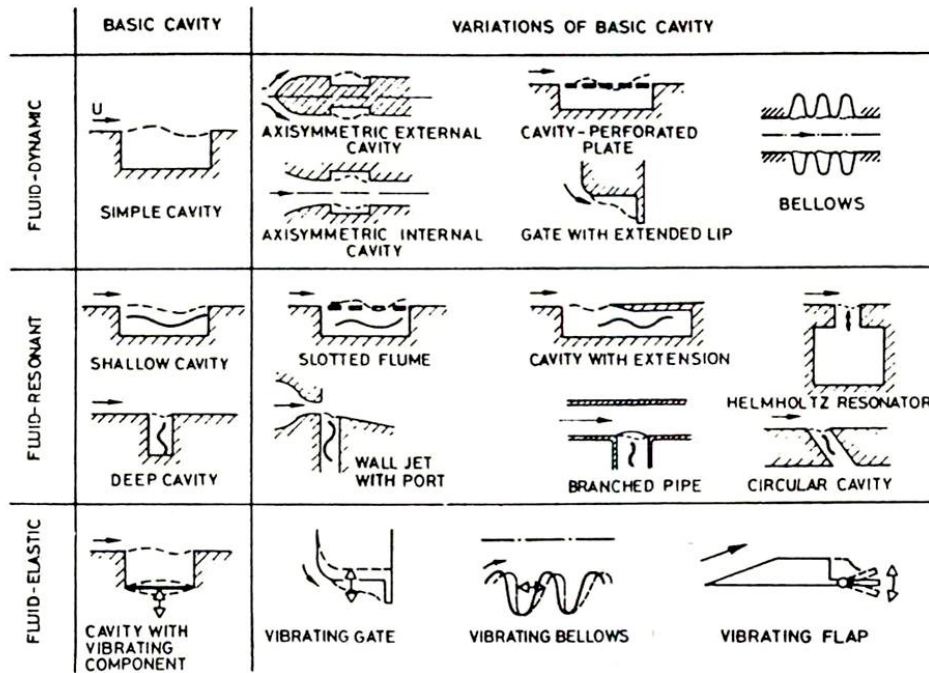


**Figure 2-6 Matrix categorization of fluid-dynamic, fluid-resonant, and fluid-elastic types of cavity oscillations (Rockwell & Naudascher, 1978)**

Lots of work has been done on the nature of the deep cavity resonance while altering the flow parameters ( (Bruggeman et al., 1991), (Ziada, 1994)). Similarities between shallow and deep cavities lie within the mechanism of excitation in both cases. But the acoustic resonance mode shape is one of the major discrepancies between them. Rossiter (1964) conducted measurements of unsteady pressure fields acting on the roof and the rear surfaces of six rectangular cavities. These cavities are of aspect ratios ( $L/d$ ) 1, 2, 4, 6, 8, and 10. The measurements were performed for a range of Mach number 0.4-1.2. The study showed that the pressure measurements for deep cavities ( $L/d=1$  and 2) were generally of periodic behavior; of one pressure peak. This is shown in figure 2-7. On the other hand, for shallow cavities ( $L/d=10$ ) the spectrum was plain in which one or more peaks of pressure fluctuations of nearly identical in amplitudes exist.

That is to say as the cavity depth decrease the fluctuations behave more randomly. The influence of altering cavity width and length for fixed aspect ratio ( $L/d=4$ ) on pressure amplitudes was also studied by Rossiter (1964). In figure 2-8, there were no consequences whatsoever on pressure amplitudes upon changing the cavity width. But changing the cavity length changed pressure amplitudes.

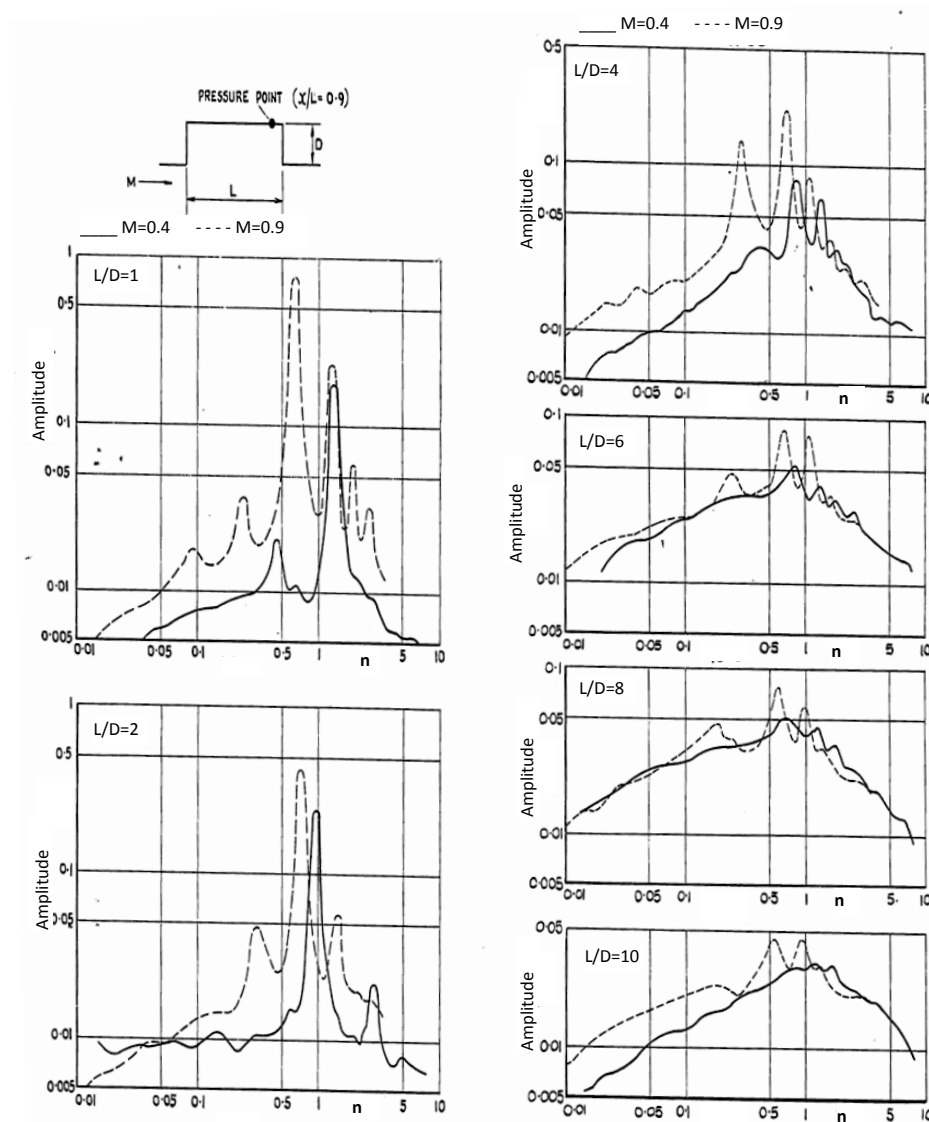


Figure 2-7 Typical amplitude spectra of pressure fluctuations at rear of cavities, where  $n$  is the non-dimensional frequency ( $n=fL/V$ ) (Rossiter, 1964)

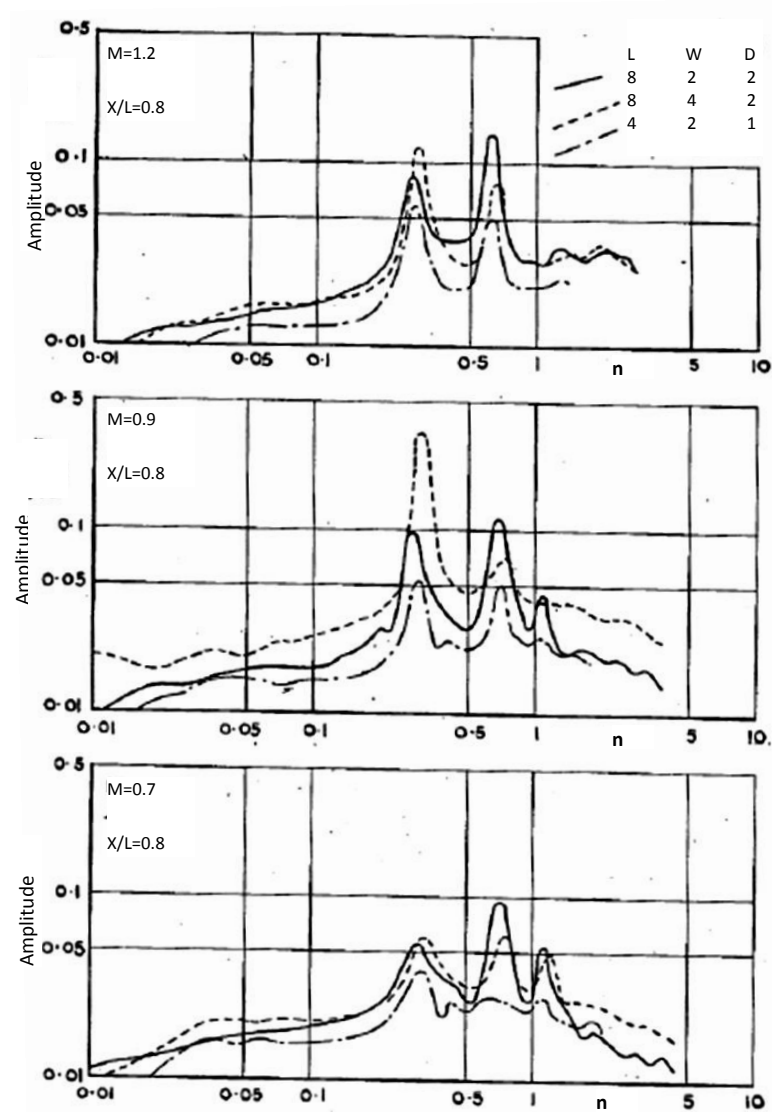


Figure 2-8 Effect of cavity width and length on amplitude spectra of unsteady pressures;  $L/d=4$ ,  $n$  is non-dimensional frequency ( $n=fL/V$ ) (Rossiter, 1964)

Aly & Ziada (2006) also conducted a series of experiments on internal axisymmetric cavities of three depths  $d=12.5\text{mm}$ ,  $25\text{mm}$ , and  $50\text{mm}$ . Also, varying cavity lengths ( $L$ ) from  $25\text{mm}$  to  $150\text{mm}$  was included. This would give a minimum aspect ratio of  $L/d=0.5$  and a maximum of  $L/d=12$ . Aly & Ziada (2006) studied the effect of changing cavity depth as well as length on pressure amplitude, strouhal number, and frequency of excitation of the excited acoustic

modes. They found that the sound pressure level for cavities with 12.5mm depth is generally lower than the sound pressure level for cavities with 25mm depth. For the third cavity depth  $d=50\text{mm}$ , all the cases exhibited very high levels of acoustic pressure. Also, the frequencies of acoustic modes for 12.5mm cavity depth are higher than those for the 25mm cavity depth. And for the 50mm cavity depth, the frequencies were all lower than those of the 25mm cavity depth. Moreover, the Strouhal number seems to change primarily with the cavity length to depth ratio ( $L/d$ ), which controls the flow field inside the cavity. On the other hand, the study showed that the ratio of cavity depth to pipe diameter ( $d/D$ ) appear to have no significant importance on the Strouhal number. This is illustrated by the values for the three different depths that concur relatively well. The study also shows that pressure amplitudes change consistently with cavity length. In addition, cavity length alters the frequencies of excited acoustic modes. Analyses of the overall aeroacoustic response of different cavities tested by Aly & Ziada (2006) showed a vital attribute which differentiate long cavities ( $L/d=3-6$ ) from short ones ( $L/d=1$  & 2). This factor is the excitation of pipe longitudinal modes by existence of small spectral peaks which agrees with the results of Rossiter (1964).

## 2.2 Suppression Methods

As previously mentioned, there are several ways to classify methods of suppressing cavity oscillations in groups. One of the well known classifications is done by Cattafesta (2008 ). This classification is shown in Fig. 2-9. He divided these techniques into two groups, passive and active control. In active group, an exterior energy input in form of mechanical or electrical signal adapts the actuator to control the flow. The second category on the other hand is controlling cavity oscillations passively by means of adding geometric modifications at the cavity edges. For example, rounding (Pereira & Sousa, 1994), ramps (Janzen et al., 2007 and Knotts & Selamet, 2003), spoilers (Bruggeman et al. 1991, Karadogan & Rockwell 1983), and a passive bleed system (Chokani & Kim, 1991). Cattafesta (2008 ) also arranged the active group into two more branches, open-loop and closed-loop. The terminology of closed-loop control describes a feedback control where the flow is sensed by a transducer which actuates the control signal

(DiStefano et al., 1990). Similarly, open loop control correlates to the case when there is no feedback loop involved.

For the present study, the interest is emphasized on different passive control techniques which are tested and discussed in the following chapters. In this section, different approaches developed in the literature to study the effect of passive suppression methods for different cavity configurations are discussed.

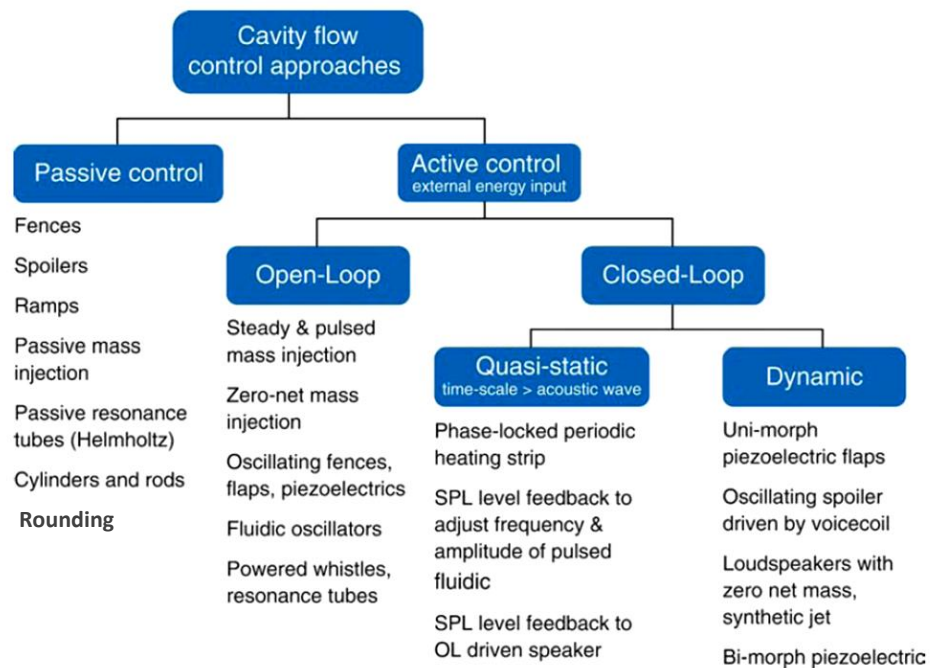
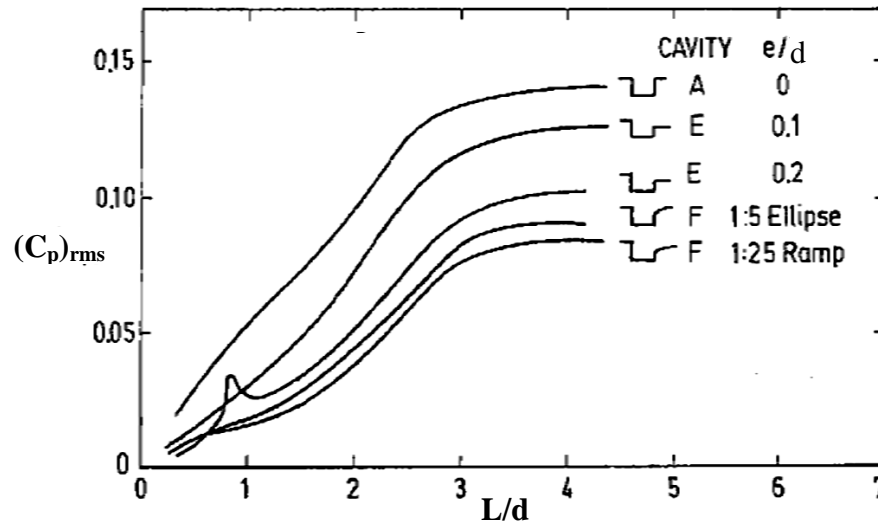


Figure 2-9 Classification of flow control schemes, (Cattafesta et al., 2003)

### 2.2.1 Rounding cavity edges

In fluid dynamic oscillations, rounded cavity edges are known to have positive effect on reducing the pressure amplitudes. Ethemaboglu (1973) investigated rounded cavity edges among different geometries of trailing edge suppressors. The results were compared with those of rectangular cavity of sharp edges. All techniques were found to attenuate pressure oscillations to a limit. As shown in figure 2-10, the gradual ramp as well as rounding the trailing edge both were the

most effectual methodologies tested. Also, Pereira & Sousa (1994) studied the influence of impingement edge geometry in water tunnel for cavity aspect ratio of  $L/d=8.33$ . The fluctuation peaks were suppressed with rounded and nose-shape impingement edges in comparison to the sharp edges.



**Figure 2-10 Effect of cavity geometry on attenuation of fluid dynamic oscillations as depicted by variation of fluctuating pressure coefficient ( $C_{p,rms}$ ) versus cavity length to depth ratio (Ethembabaoglu, 1973)**

Bruggeman et al. (1991) investigated the suppression of fluid resonant oscillations analytically and experimentally in a deep side branch and multiple side branches. In single side branch of square cross section, rounding the cavity edges was included in the study. The ratios of radius of curvature ( $r$ ) to cavity length ( $L$ ) investigated were 0.1 and 0.2. The results have shown that the variation of radius of curvature ( $r$ ) of downstream edge for the T-joint changed the pressure amplitude as rounding of the upstream edge. This is shown in figure 2-11 when compared with sharp cavity edges. A sharper downstream edge correlates with higher values of the acoustic particle velocity. This results in increasing the power generated by factor of two. Knotts & Selamet (2003) also studied the effect of three different edge geometries on deep side branch. Rounding the upstream and the downstream edges was one of the configurations tested. The ratios of curvature to cavity length ( $r/L$ ) examined were equal to 0.25, 0.5, 0.75, and 1.0.

The results of the investigation were similar to what was found by Bruggeman et al. (1991).

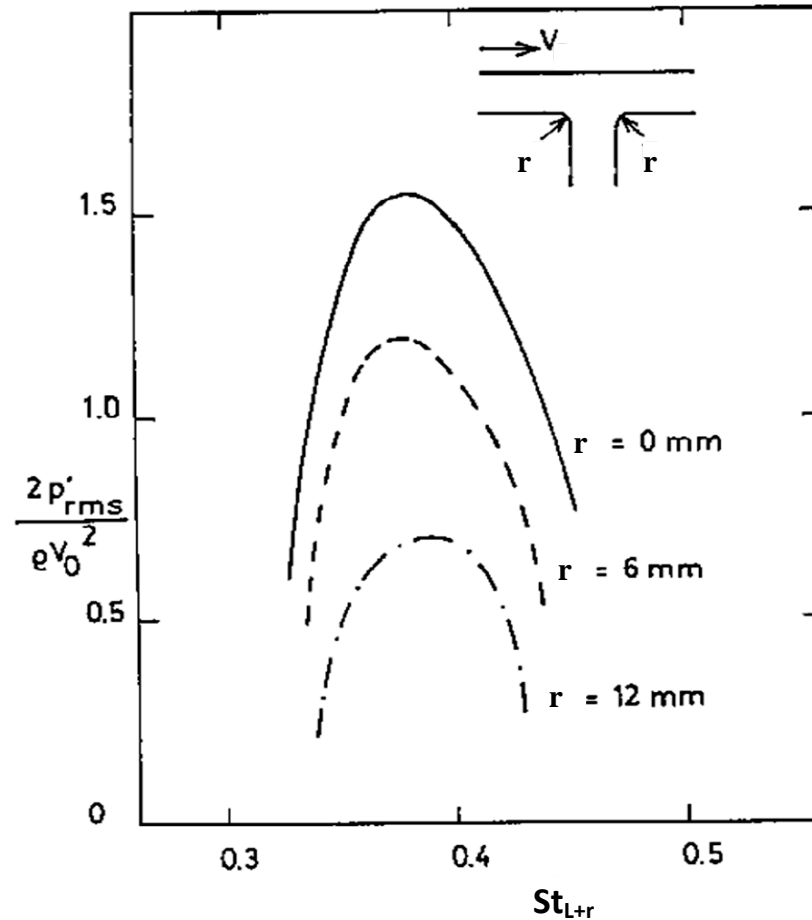


Figure 2-11 Influence of the radius of curvature of the edges on the amplitude of pulsations in a single side branch set-up, Square pipe  $L=0.06$ m, \_\_\_  $r=0$ , ---  $r=6$ mm, - . . -  $r=12$ mm (Bruggeman et al., 1991)

Effective cavity length ( $L_e$ ) for deep side branches was also defined by Bruggeman et al. (1991) when calculating the Strouhal number. The Strouhal number is defined as  $St=f L_e/V$ , where  $f$  is the resonance frequency,  $L_e$  is the characteristic length of the cavity, and  $V$  is the mean flow velocity. Figure 2-11 shows the dimensionless pressure amplitude versus Strouhal number based on effective cavity length ( $L_e = L+r$ ). The figure shows that replacing the cavity

length;  $L$ , with effective cavity width;  $L+r$ , aligns the peaks of pressure amplitudes. This was also reported by Nakiboglu et al, (2009 ) and Nakiboglu et al, (2010) in corrugated pipes and multiple side branches. For corrugated pipes, the research aimed to find out the appropriate characteristic length ( $L$ ) for the Strouhal number. Different characteristic lengths were investigated, e.g. the distance between the centers of the tandem corrugations. These dimensions were the gap length ( $\text{gap} = r_{\text{up}} + L + r_{\text{down}}$ ), and the modified gap length ( $\text{modgap} = r_{\text{up}} + L$ ). Each corrugation is a slit shaped cavity with a Length ( $L$ ) and depth ( $d$ ). The radius of the edges was designated by  $r_{\text{up}}$  and  $r_{\text{down}}$  for upstream and downstream edges, respectively. The comparison is shown in figure 2-12 (a) & (b). The experimental results showed that the appropriate characteristic length ( $L_c$ ) for corrugated pipes was  $L + r_{\text{up}}$ . For multiple side branches, the same behavior was reported by Nakiboglu et al. (2010) as shown in figure 2-13. The figure points out two things here; first, rounding the upstream edge would produce higher pressure pulsation than with sharp upstream and round downstream edges as reported earlier by Bruggeman et al. (1991). Second, the characteristic cavity length for multiple side branches is the same as corrugated pipes. This agrees with the previous results reported in the literature.

Regarding the acoustic pressure amplitude in double T-joint set up, Bruggeman et al. (1991) investigated the effect of rounding the edges. Rounding edges of the two T-joints produced high pulsation levels, as shown in figure 2-14. This is in comparison with rounding only the edges of the second T-joint and sharp edges of the first T-joint. However, lower level was recorded when the first joint had rounded edges while the second had sharp edges.

In gate valves, rounding both upstream and downstream edges with radius of curvature ( $r=0.9\text{mm}$ ) was tested by Smith & Loluff (2000). In addition, testing rounding only the upstream edge and only the downstream edge was included. Rounding both upstream and downstream edges as well as the upstream edge was effective in reducing noise. However, rounding the upstream edge introduced higher pressure loss. While rounding the downstream edge, a slight reduction in the maximum pressure coefficient was accomplished. Smith & Loluff (2000) also concluded that the combination of an upward ramp and rounding the cavity edges

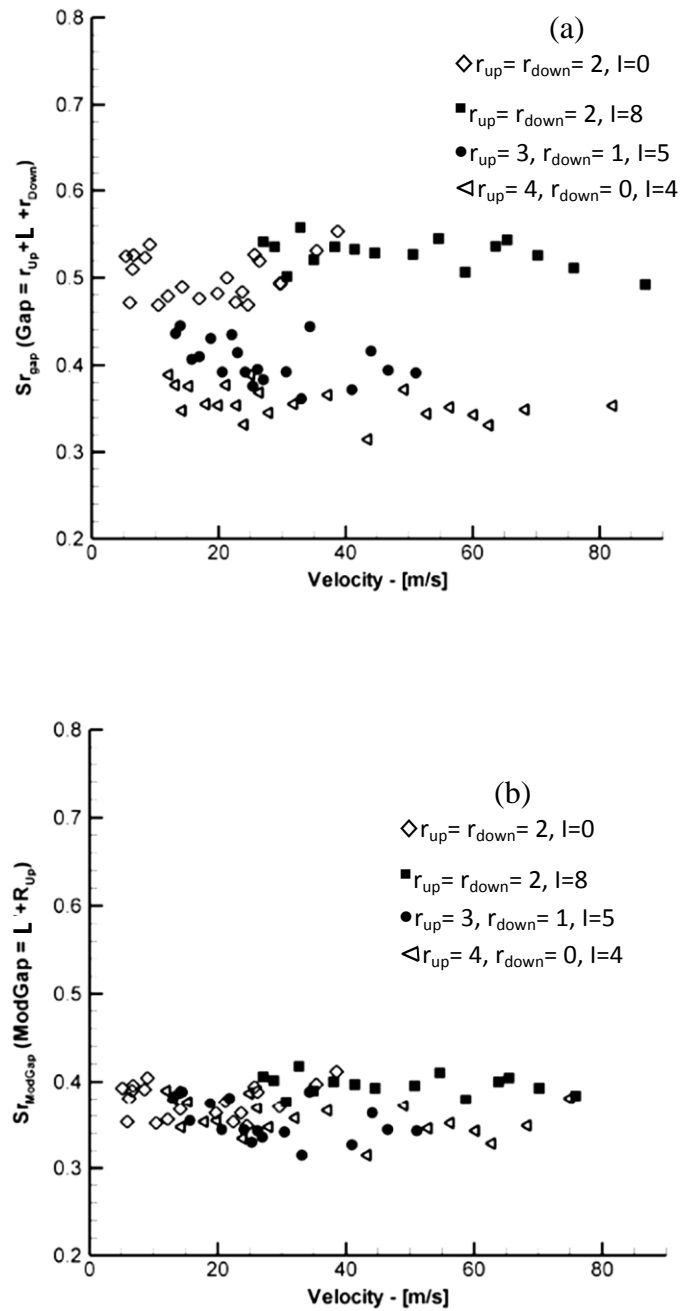


Figure 2-12 Comparison of Strouhal number versus flow velocity with  $L/d=1$  for four edge geometries (a) based on gap length and (b) based on modified gap length,  $l$  is the distance of the constant diameter pipe between two cavities, (Nakiboglu et al., 2009 )

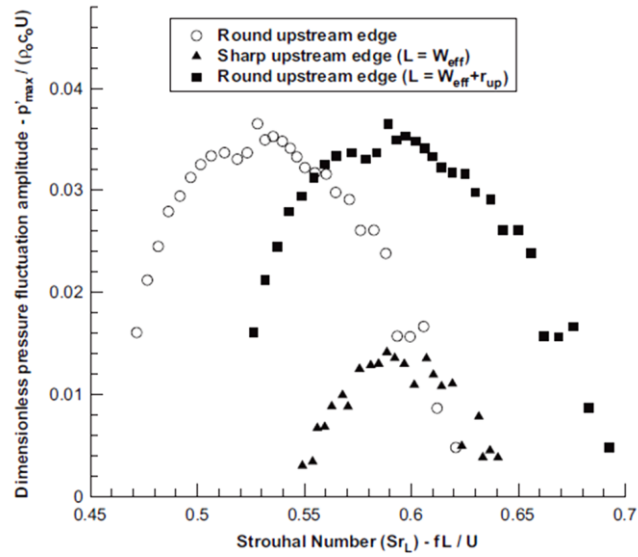


Figure 2-13 Dimensionless pressure fluctuation amplitude for the 3rd acoustic mode as a function of Strouhal number for round upstream–sharp downstream case and sharp upstream–round downstream case (Nakiboglu et al., 2010)

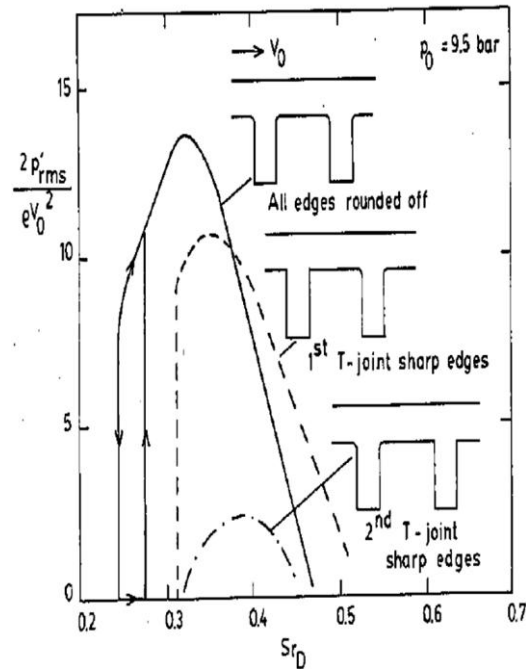


Figure 2-14 Influence of the radius of curvature of the edges on the amplitude of pulsations in a double side branch set-up, \_\_\_ Rounded edges, --- First T-joint sharp edges, - . . - Second T-joint sharp edges (Bruggeman et al., 1991)

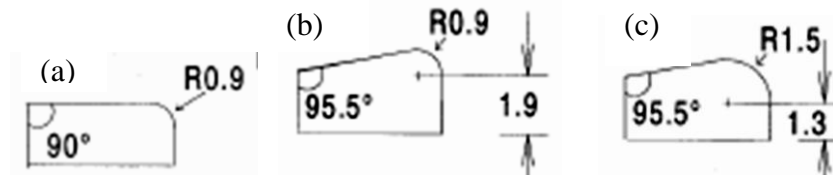


Figure 2-15 Rounding valve seats in gate valves (a) rounding edge only, (b) and (c) combined upward ramp and rounding edge (Smith & Loluff, 2000)

with two different radius of curvature as shown in figure 2-15, did not provide significant reduction in tonal noise.

## 2.2.2 Chamfering the cavity edges

The second most effective suppression device among *fluid dynamic* oscillations is the trailing edge and/ or leading edge downward ramp. It is also sometimes called chamfer or bevel. Shaw (1979) investigated experimentally three kinds of suppression devices on a rectangular cavity of  $L/d=2$  at supersonic and subsonic speeds. Trailing edge ramp was one of the suppression configurations examined. This is in addition to the combination of the trailing edge ramp with another two suppression devices. All devices tested by Shaw (1979) have proven effectiveness in pressure amplitude attenuation. The choice of appropriate method would depend on the level of attenuation required. Franke and Carr (1975) found that double ramps or chamfers (i.e. upstream and downstream of a cavity) in air flow would reduce the pressure fluctuations effectively in the cavity. Figure 2-16 shows the comparison of the pressure amplitudes between rectangular cavity and double ramped cavity. The attenuation of the peaks reached 20 dB but at the expense of increasing the background turbulence. Same results were reported by Heller & Bliss (1975). They examined trailing edge ramp for cavity of aspect ratio  $L/d > 4$  for the range of Mach number  $0.8 \leq M \leq 2.0$ . Trailing edge ramp has also proven effectiveness when combined with leading edge spoiler for cavities of aspect ratio  $< 4$ . Such combination will be discussed later.

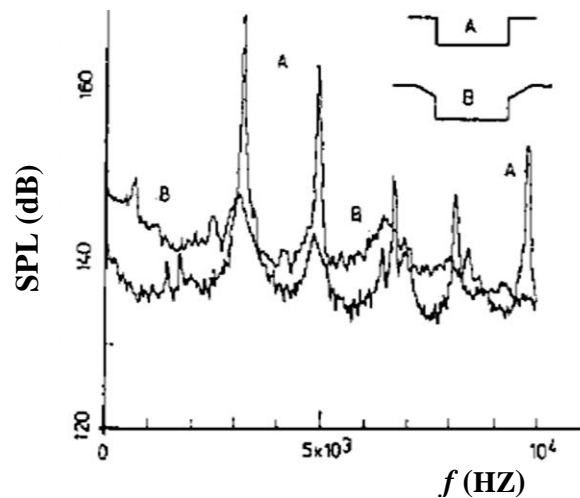


Figure 2-16 Effect of double ramp on attenuation in shallow cavity oscillations (Franke & Carr, 1975)

In gate valves, Smith & Loluff (2000) examined the effect of chamfering the upstream and the downstream cavity edges on suppressing pressure fluctuations. The experiments were done for 25 cavity configurations. The study comprehended the effect of modifying cavity inserts, valve desks, and valve seats on suppressing pressure pulsations. The results reported by Smith & Loluff (2000) concluded that modifying the valve seats would be the most practical solution in the steam line valves. In addition, the study included testing different chamfer configurations. This is in form of different angle of inclination, chamfer length and depth. All chamfered seats showed significant reduction and delay in pressure pulsations. The results also showed that the ratio of chamfer length to cavity length ( $\ell/L$ ) is an important parameter. A  $15^\circ$  chamfer of three different lengths was examined; short, medium, and full length. The full and medium chamfer lengths were of the same effectiveness in reducing the noise levels. On the other hand, the short length was only capable of delaying the noise up to higher Mach number. Figure 2-17 shows the pressure spectra of the reference valve seat (no modifications) and the medium length chamfer seat. As shown, the chamfer seat suppressed the pressure amplitudes along the tested range of Mach number. This chamfered seat has also proven effectiveness in reducing the high tonal noise in deep axisymmetric cavity.

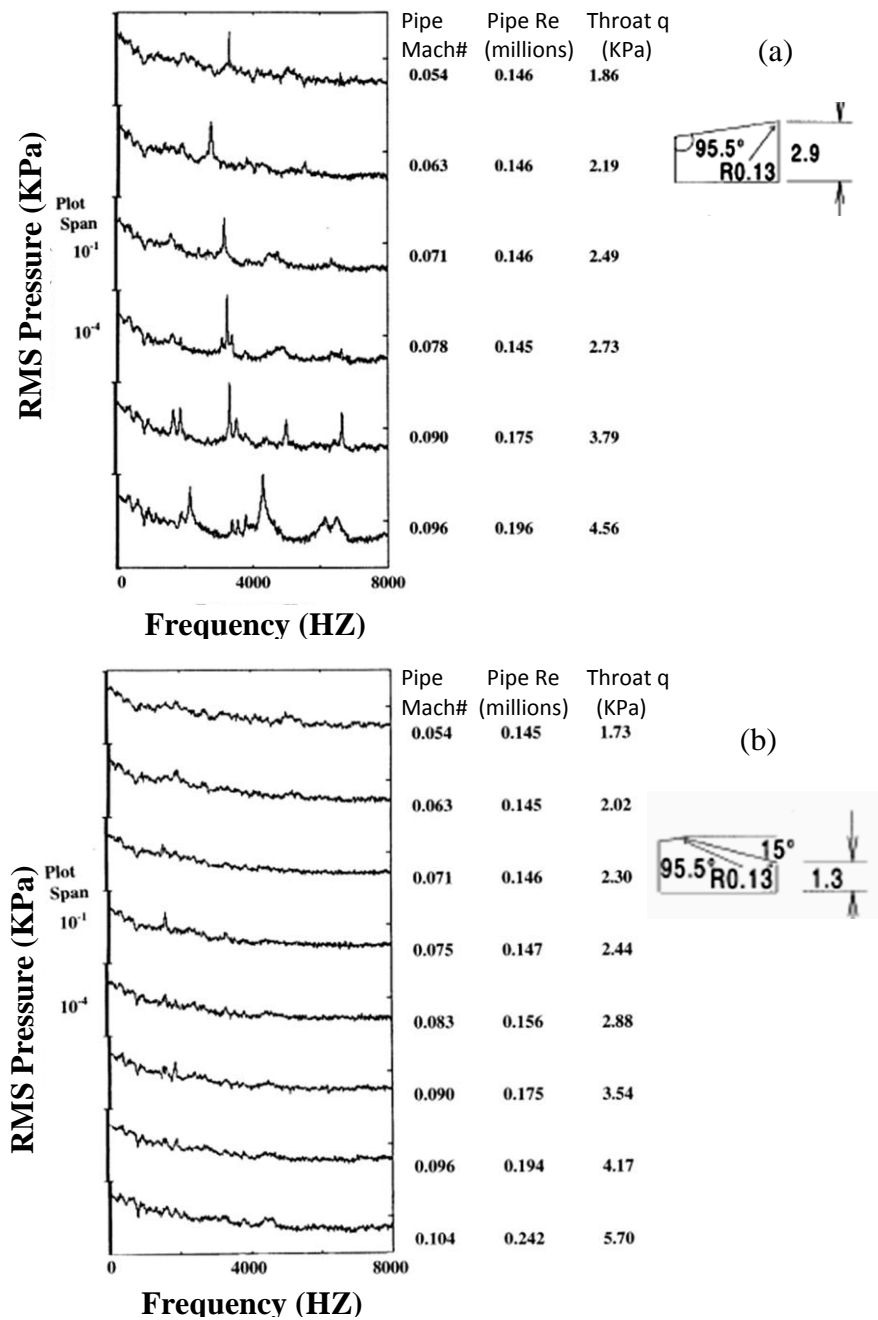


Figure 2-17 Pressure pipe spectra measured with (a) reference valve and (b) 15° chamfer up and downstream the cavity, q is the dynamic pressure in the throat valve (Smith & Loluff, 2000)

Janzen et al. (2007) replicated the test conditions investigated by Smith & Loluff (2000). They studied the dependence of noise production on valve seat geometry in cold reheat steam lines. Experiments were conducted on the original valve seat (with no chamfer) and 19 chamfer designs inserted upstream the cavity. The recommendation stated by Smith & Loluff (2000) is that the axial length of the chamfer should not be less than 20% of cavity length. The acoustic response of a chamfered seat designed based on this suggestion with  $13^\circ$  angle of inclination, 20% chamfer length to cavity length and 8mm depth is shown in figure 2-18. The figure shows that slight suppression and delay of the maximum pressure amplitude is achieved compared to the reference seat. This result was no success as the maximum pressure amplitude lies within the range of operation. Same results were reported for chamfer seats having the same angle of inclination and depth but different chamfer length. Janzen et al. (2007) also investigated the effect of lengthening the chamfer. These seats developed same acoustic response as the previous chamfers. Following that series of experiments, the effect changing the angle of inclination with constant chamfer depth was examined. These tests succeeded in suppressing the tonal noise within the range of operation. Figure 2-19 shows the lowest response achieved with  $17.3^\circ$  chamfer seat and 19.2% chamfer length to cavity length. The study also included testing  $16^\circ$  and  $14^\circ$  chamfers with the same configurations  $17.3^\circ$  chamfer seat. These two chamfers were extended on both sides of 12-O'clock position instead of  $360^\circ$  around the seat. This design showed sensitivity to the slight changes in geometry and produced variable acoustic response. Moreover, the compound chamfer seat shown in figure 2-20 was tested. This design partially suppressed and delayed the maximum pressure amplitude was achieved. In addition, it was difficult to be machined and it interfered with the flow conditions.

In deep side branch, Knotts & Selamet (2003) first tested upstream and downstream chamfers. The ratios of chamfer length to cavity length tested were 0.75, 1.5, 3.0, and 4.5. All chamfers tested suppressed pressure peaks compared to the amplitudes with sharp edges, where all designs developed same behavior of suppression. The difference among these chamfers is that as the size of the chamfer increases the suppression of pressure amplitudes increases. Secondly, Knotts & Selamet (2003) tested only upstream chamfers and only downstream

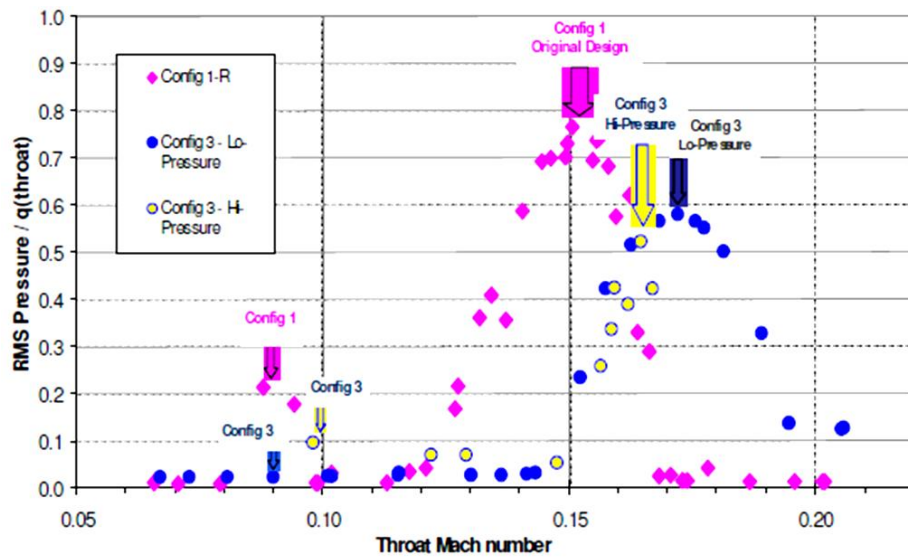


Figure 2-18 Normalized acoustic response for Seat Design of 13° chamfer angle, 8 mm depth (Janzen et al., 2007)

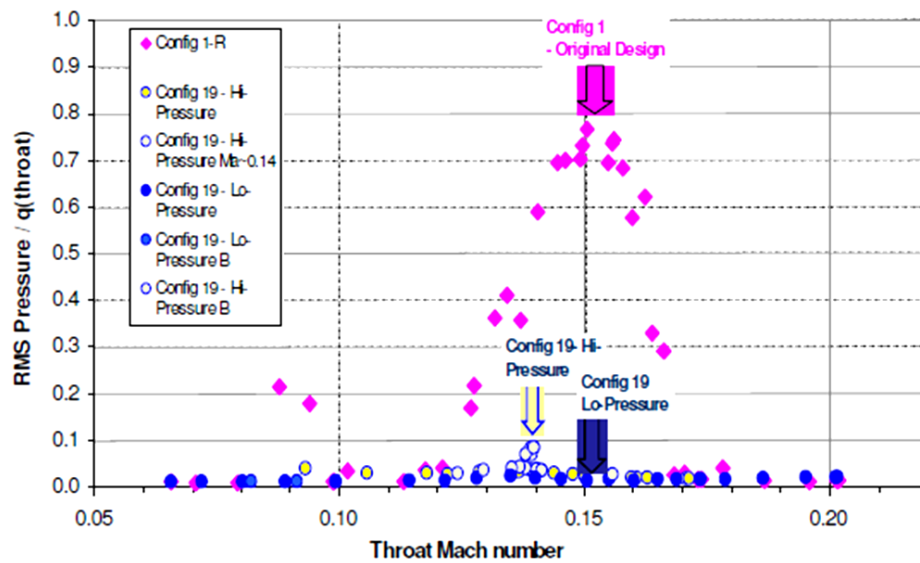


Figure 2-19 Normalized acoustic response for Seat Design of 17.3° chamfer angle, 19.2% chamfer length to cavity length (Janzen et al., 2007)

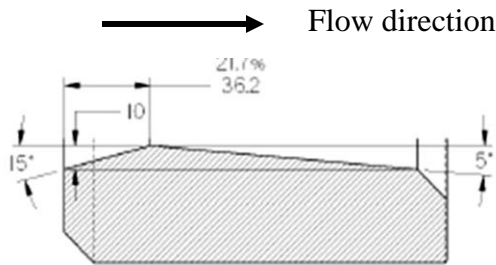


Figure 2-20 Compound chamfer design (Janzen et al., 2007)

chamfers. The upstream chamfers showed same results as the double chamfers. They concluded that only upstream chamfers are capable of suppressing, which agrees with previous literature. On the other hand, the downstream chamfer showed no significant suppression, which also agrees with the reported literature.

### 2.2.3 Leading edge Spoilers

Another tested passive control method is introducing a spoiler at the cavity leading edge. Spoilers were among the first types of flow control devices in *fluid dynamic oscillation* to be studied associated with cavities. Shaw (1979) investigated the combination of leading edge spoiler and a trailing edge downward ramp as shown in figure 2-21 (a). The test was done for a rectangular cavity of aspect ratio 2 at subsonic and supersonic speeds. The comparison of the pressure levels is shown in figure 2-21 (b) for the basic cavity and the cavity with ramp and spoiler. The figure shows greater reduction was achieved when adding to cavity leading edge spoiler and trailing edge ramp compared to the basic cavity. The overall suppression reached was in the range of 20 dB.

Dix & Bauer (2000) tested experimentally and numerically the effect of two types of leading edge spoilers. This is done for three rectangular cavities of aspect ratio 14.4, 9.0, and 4.5. The two spoilers were flap-type and vertical-type with configuration shown in figure 2-22. The vertical spoiler includes various styles: fine- and coarse saw tooth, and solid spoiler (or fence) was also included. The spoilers' height were designed and manufactured based on boundary layer thickness ( $\delta$ ). The spoilers were tested at two locations; at the leading edge of the cavity and further upstream the cavity edge, see figure 2-23. The experimental

and the numerical results showed that the presence of leading edge spoiler reduces pressure peaks and the overall sound pressure level in the spectrum associated with the cavity. The results agree with literature about the effectiveness of the leading edge spoilers in suppressing pressure amplitudes.

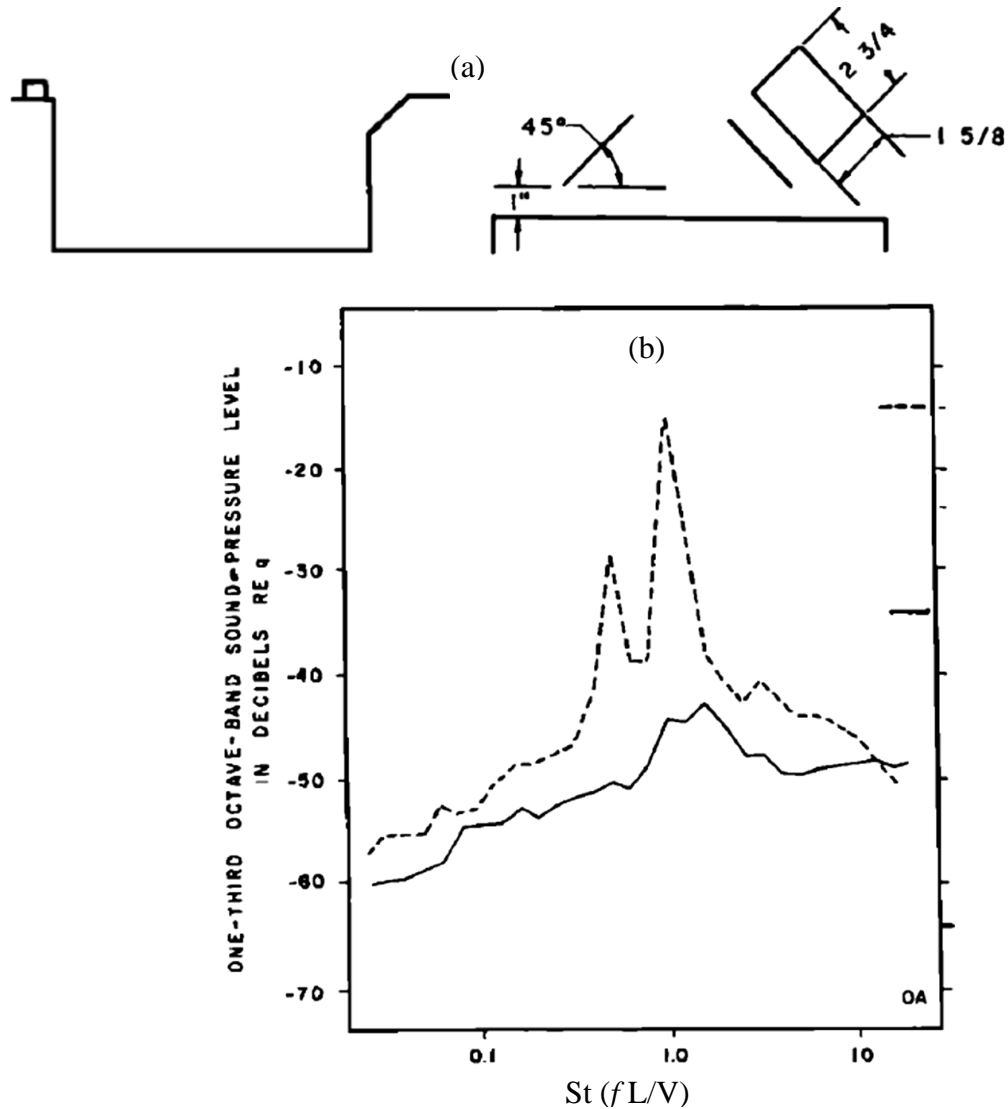


Figure 2-21(a) Cavity with leading edge spoiler and trailing edge ramp configuration, (b) Comparisons of spectra of configurations with and without suppressors for 1.2 Mach number and 30000 ft altitude, ----basic cavity, \_\_\_\_ cavity with spoiler and ramp (Shaw, 1979)

Schmit & Raman (2006) compared the effectiveness of zero-, low-, and high-frequency flow control methodologies applied to a generic weapons bay cavity. The cavity had aspect ratio of  $L/d = 5$  and was tested at 0.85 and 1.19 Mach number. The zero-frequency actuator tested is a conventional “saw-tooth” spoiler, and will only be discussed here as it is related to the current study. The spoiler has similar configuration as shown in figure 2-22 but of different dimensions. The spectrum levels of the “saw-tooth” spoiler showed a satisfying suppression in comparison with baseline cavity at 0.85 Mach. Also, the suppression of pressure amplitudes was minimal at 1.19 Mach.

Rossiter (1964) was among pioneers to examine the effect of leading edge spoiler on reducing pressure amplitudes. Tests were conducted on rectangular cavity of  $L/d=1$ . Three simple spoilers at the cavity leading edge shown in figure 2-24 were investigated. The results of the investigation show that any sized spoiler would produce satisfactory reductions to pressure fluctuations.

Bruggeman et al, (1991) also studied four different spoiler configurations in double T-joint shown in figure 2-25. It was found that spoilers would be largely efficient when introduced upstream rounded edges of the T-joint. Moreover, spoilers have shown their reliance on pressure when placed upstream of the first T-joint of multiple side branch setups. This is clearly shown in figure 2-26(b) with spoiler no. 1 and figure 2-26(c) with spoiler no.3. In addition, Bruggeman et al, (1991) reported that establishing spoilers upstream the second T-joint would produce higher reduction in pulsation. This is shown in figure 2-26(e) and figure 2-26(d) for spoiler no. 2 and spoiler no. 3, respectively.

In deep side branch, an upward ramp or fence at the cavity upstream edge was investigated by Knotts and Selamet (2003). The ratios of fence height to cavity length ( $h/L$ ) studied were 0.125, 0.25, 0.5, and 0.75. The comparison between upstream ramps and sharp edges shows that the ramps/fences of  $h/L=0.125$  and 0.25 were effective in suppressing the high pressure amplitudes. Also, the results exhibited new pressure peaks at higher frequencies with these two ramps. This is in comparison to the response of sharp edged cavity. In addition, the other two ramps with  $h/L= 0.5$  and 0.75 completely suppressed all base case peaks without introducing new distinguished pressure peaks.

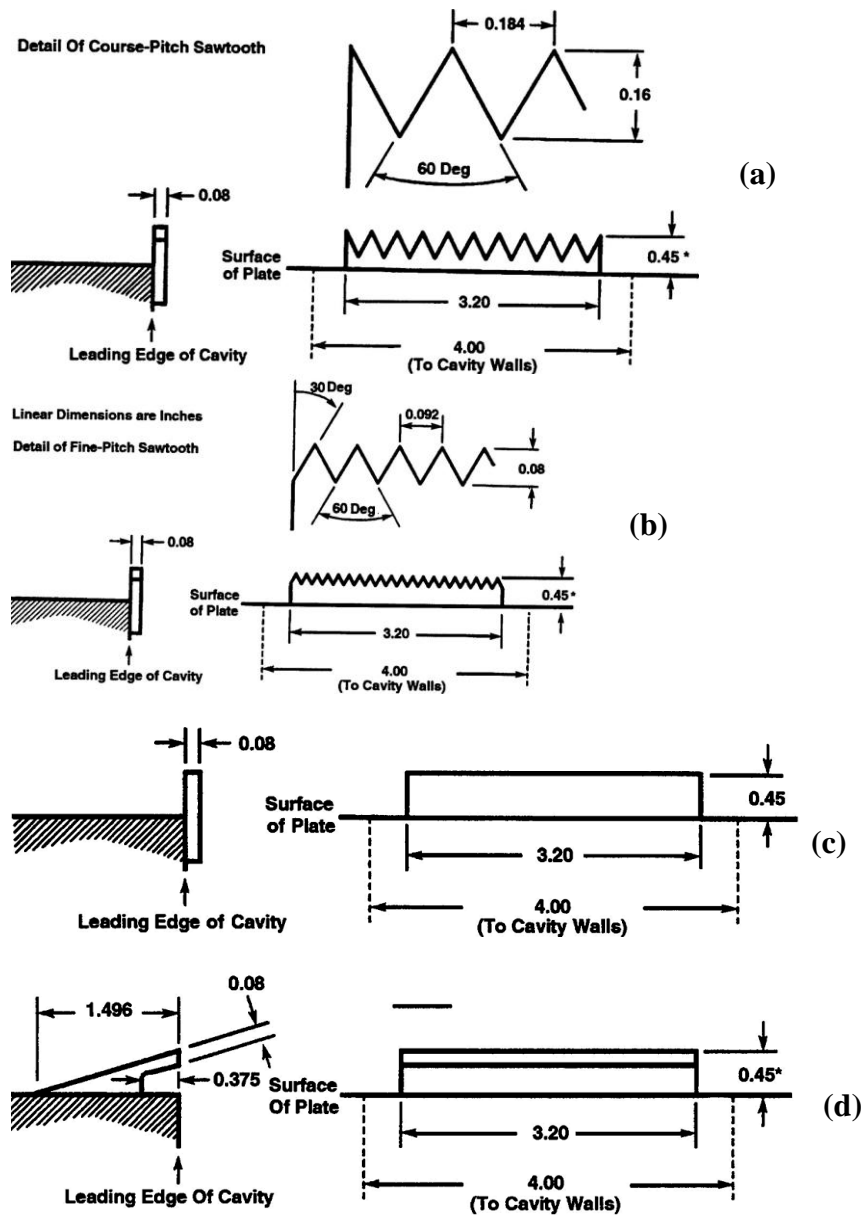


Figure 2-22 Configuration of vertical and flap type spoilers, (a) Sawtooth spoiler, coarse pitch, (b) Sawtooth spoiler, fine pitch, (c) Solid spoiler (fence), and (d) Flap-type spoiler, (Dix & Bauer, 2000)

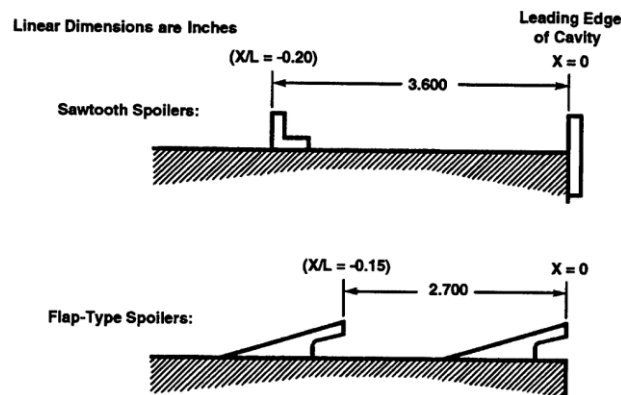


Figure 2-23 Two locations were the spoilers mounted, (Dix & Bauer, 2000)

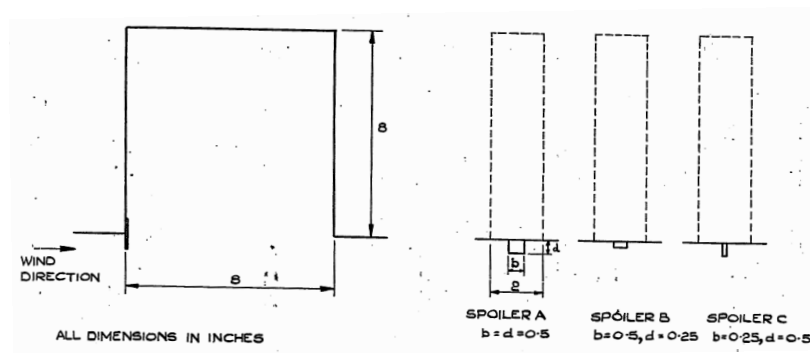


Figure 2-24 Sketch of leading edge spoiler tested with cavity  $L/d=1$ , (Rossiter, 1964)

Karadogan & Rockwell (1983) studied the effect of changing the tooth height ( $h$ ), pitch ( $t$ ) and angle of attack ( $\theta$ ) of vortex generators. The vortex generators had two different configurations and were examined in cavity of aspect ratio 1.8. Karadogan & Rockwell (1983) reported that the two vortex generators had the same acoustic response. In addition, upon increasing the tooth height, the level of attenuation of the excited acoustic modes was increased. Also, increasing the pitch successfully attenuated all pressure peaks. Yet, additional peaks started to appear at higher frequencies. Finally, increasing angle of attack significantly suppressed and delayed the pressure amplitude of lower modes to higher flow velocities. On the other hand, higher acoustic modes were only delayed to higher flow velocity. These results agree with the reported literature about the effectiveness of leading edge spoilers in suppressing pressure amplitudes.

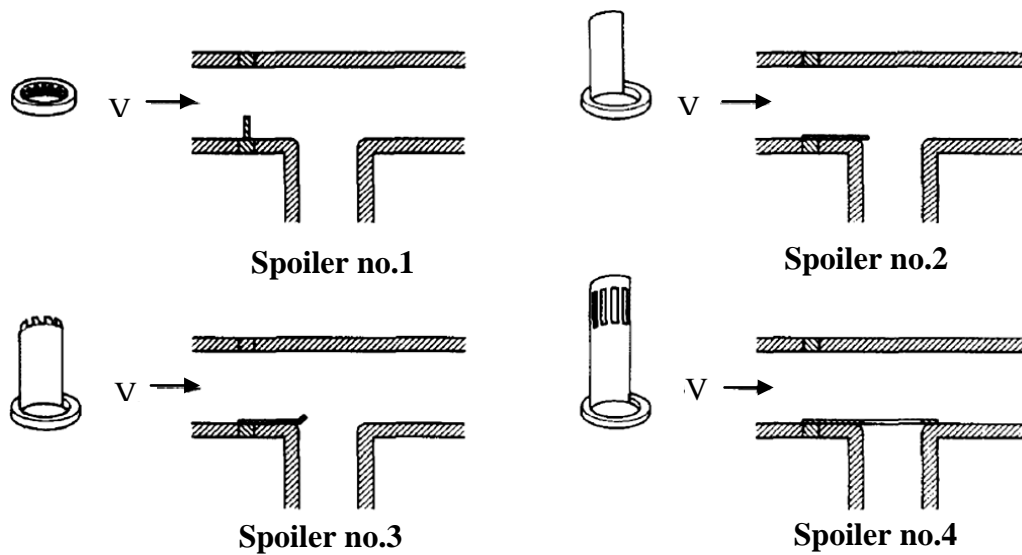


Figure 2-25 Configuration of spoilers, (Bruggeman et al., 1991)

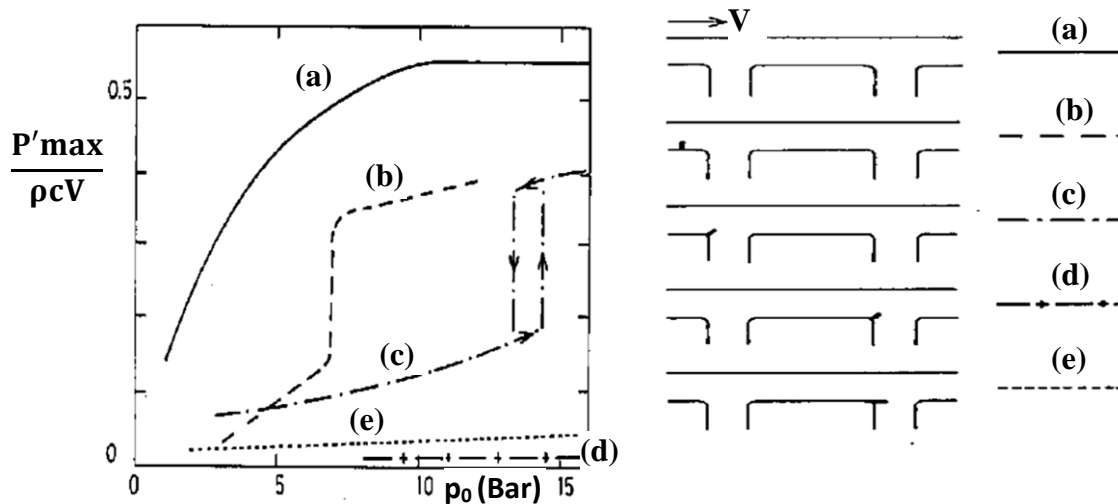


Figure 2-26 Influence of pressure  $p_0$  on the performance of spoilers and sharp edges (vortex damping); (a) Reference measurements with rounded edges; (b) spoiler no. 1 upstream of the first side branch; (c) spoiler no. 3 upstream of the first side branch; (d) spoiler no. 3 upstream of the second side branch; (e) spoiler no. 2 upstream of the second side branch (Bruggeman et al., 1991).

## 2.3 Focus of the present research

Flow over cavity, such as cavities in aircraft or gate valves, can generate intensive pressure fluctuations in and around the cavity. These cavity oscillations are self-sustained by a feedback excitation mechanism. The oscillations are categorized according to the nature of the feedback phenomenon that activates the self-sustained oscillations. Rockwell and Naudascher (1978) classified this excitation mechanism into three groups: 1) fluid-dynamic, 2) fluid resonant and 3) fluid-elastic oscillations. Different passive suppression techniques were investigated for the three groups. For fluid-resonant oscillations, these methods would depend highly on the acoustic mode shape. The cavity geometries that received most of the attention were deep single side branch, multiple side branches, and corrugated pipes. In single and multiple side branches, the resonance mode exists inside the branch. In corrugated pipes, the resonance mode is a longitudinal mode in the pipe. In these cases the acoustic wave length is much larger than the cavity length. On the other hand, study of passive techniques to suppress fluid resonance oscillation in internal cavities did not receive much attention in the literature. The excited acoustic modes in internal cavity are the cavity-duct geometry diametral modes. In this case, the ratio of the acoustic wave length to cavity length is relatively shorter than the same ratio for corrugated pipes and side branch. This difference separates the trapped modes of internal cavities from most of the previous study reported in the literature. Thus, the current study focuses the excitation of trapped modes of on internal axisymmetric cavity.

Cavity oscillations can be controlled passively through several geometric changes such as rounding cavity edges, upstream and/or downstream ramps/chamfers, and leading edge spoilers. Rounding the cavity edges have been known to eliminate and delay noise in fluid dynamic oscillations. In fluid resonant, rounding the cavity does not suppress the acoustic resonance in many cases. Chamfering cavity edges has ascertained its effectiveness as suppressive method in fluid-dynamic and fluid-resonant oscillations. Literature has shown that upstream chamfering is also capable of noise reduction. Another popular passive

suppression technique is leading edge spoiler. Leading edge spoilers are commonly found to be effective suppressive mechanism.

This study addresses the effect of three different passive suppressive techniques on the excitation of trapped modes of an axisymmetric cavity. The three techniques are rounding cavity edges, upstream chamfering the cavity, and leading edge spoiler. The investigation matrix includes the study of two rounding radii, two chamfer geometries and three different types of leading edge spoilers. The spoilers types are square toothed, curved and delta spoilers. The findings of the current research will improve the state of knowledge of passive suppression methods of excited acoustic modes of cavity-duct system.

# CHAPTER 3

## Experimental Test Setup

---

This chapter describes the experimental test setup used in this study. This constitutes the description of the test facility, test section, the designs of the different suppression seats and the measurements approach throughout this study. The test section was constructed by Aly (2008) to study the excitation of the diametral modes of the cavity-duct system. The test section is modified to study the effect of different suppression devices on the excited diametral modes. The chapter starts with the discussion of the test facility in section 3.1. This is followed by the description of the test section in section 3.2. The basic geometry of the cavity will be presented in section 3.3. The test conditions and the boundary layer characteristics at the upstream edge of the cavity are presented in section 3.4. The characteristics of the acoustic shear layer coupling are discussed in section 3.5. Section 3.6 depicts the designs of different suppression devices which are considered in this study. Instrumentation and test procedure are discussed in sections 3.7 & 3.8, respectively.

### **3.1 Test Facility**

The measurements are carried out using an open loop wind tunnel. Figure 3-1 shows a schematic diagram of the wind tunnel. A centrifugal blower of 50 horse power is fitted next to the wind tunnel. A variable driving speed control unit is used to set the blower speed. This would alter the flow rate through the wind tunnel. The maximum rotational speed of the blower can provide a flow velocity up to 150m/s within the test section. Nevertheless, cavity dimensions, suppression device under examination & amplitudes of acoustic pressure all contribute in determining the maximum flow velocity in test section.

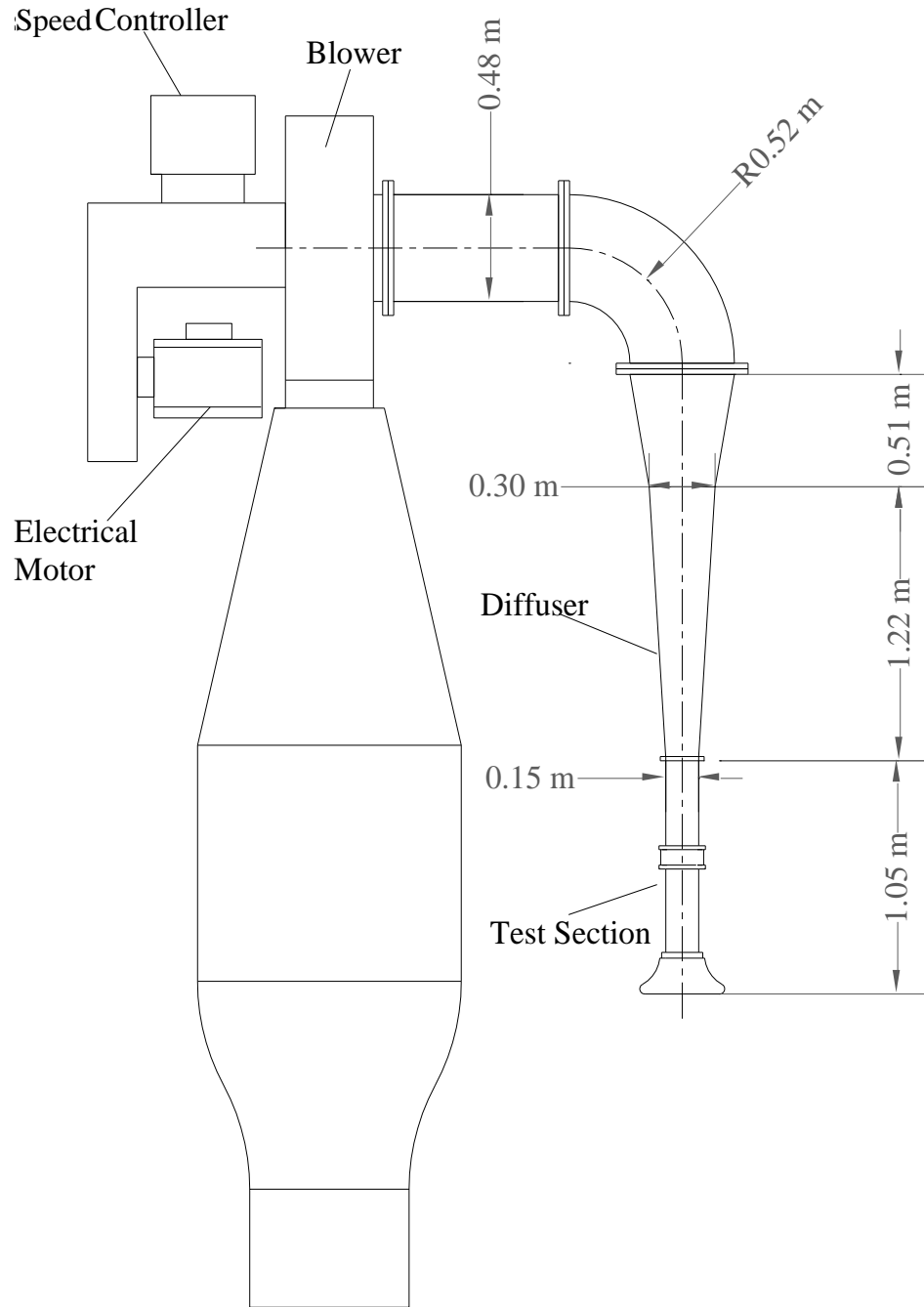


Figure 3-1 Schematic of the test facility (Aly, 2008)

On the suction side of the blower, an axisymmetric diffuser is attached in series with the test section. This provides a ratio of cross sectional area of the test section to the blower inlet area of 0.1. As a result there were difficulties accompanied the design of the diffuser of such large area ratio. In order to find the appropriate design, a commercial CFD package is adopted by Aly (2008) to perform an extensive numerical simulation. As shown in figure 3-2, the diffuser is fabricated from steel sheet of 1.5 mm thickness. It is divided into two portions, the upstream of 1.22 m (four feet) long and the downstream of 0.51 m (two feet) long. Further description of the diffuser is found in Aly (2008). A parabolic bell-mouth made of wood (Aly, 2008) is positioned at the inlet side of the test section. This is to provide a uniform velocity profile at the inlet and to diminish both turbulence level and pressure drop.

### **3.2 Test Section**

Aly (2008) built the test section to investigate the excitation of diametral modes of an axisymmetric cavity in a duct. For the current study, the test section is modified to accommodate the examination of the passive suppression devices. The test section design allows the study of the effect of these seats for three different cavity depths; 25mm (one inch), 12.5mm (half inch), and 50mm (two inch) deep. The investigation includes the measurements of amplitudes and frequency of the excited acoustic modes within the cavity. The cavity length changes from 25 mm (one inch) to 50 mm (two inch) long for the three cavity depths. The passive suppression devices tested in this study are rounded edges, chamfer and spoilers at the cavity edges. The suppression devices are introduced in form of seats. All passive suppression seats are installed at the upstream edge of the cavity; except for rounding seats. The rounded seats are at the installed up- and downstream edges of the cavity. Figure 3-3 (a) & (b) show a schematic drawing of the test section geometry and the basic dimensions of the axisymmetric cavity, respectively. The cavity length, cavity depth, duct diameter are noted as  $L$ ,  $d$ , and  $D$ , respectively.

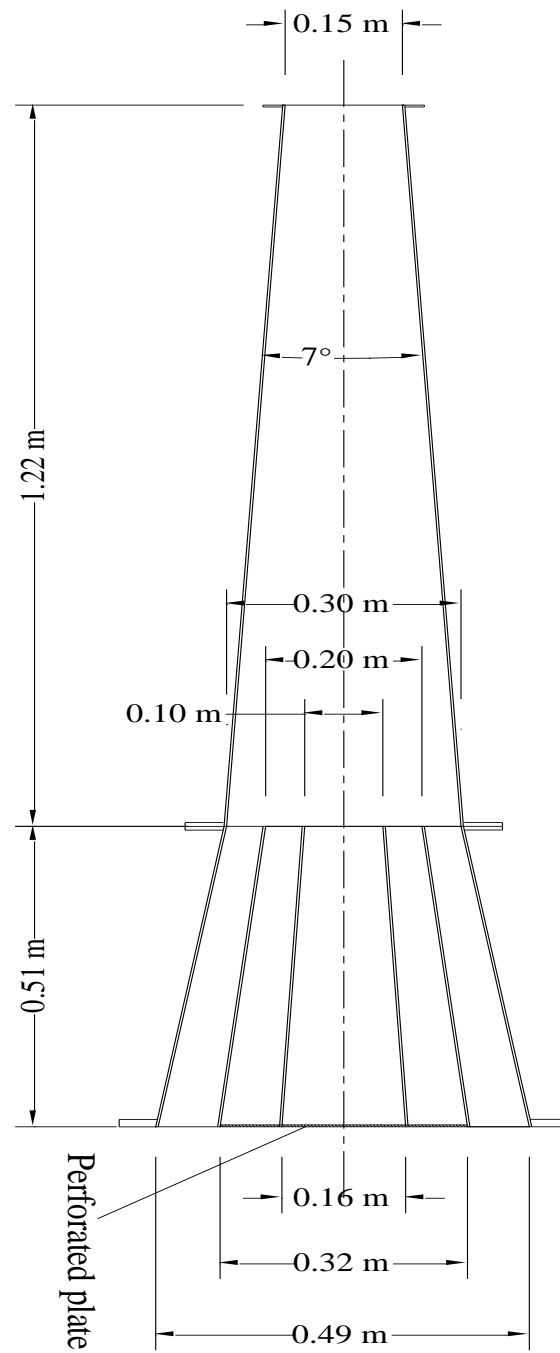


Figure 3-2 Schematic of the diffuser design (Aly, 2008)

Three parts constitute the axisymmetric cavity in the test section, two acrylic pipes of 150 mm in diameter and acrylic flanges of larger diameter joining the two pipes. The two acrylic pipes are of 6.25 mm wall thickness and 450 mm long. The two pipes are connected to the cavity with the help of two small flanges glued to the pipes. Accuracy of dimensions for the acrylic flanges is assured by manufacturing them using a CNC machine. In order to minimize acoustic losses accompanied by cavity wall vibrations, the stiffness of flanges forming the cavity wall is needed to be high. So the flanges have 25 mm wall thickness. Another advantage of high stiffness is avoiding geometrical distortion during assembly. There are three groups of flanges forming three different cavity depths. The cavity depths under study are 12.5 mm (half inch), 25 mm (one inch), and 50 mm (two inch). This corresponds to flanges of inner diameters 175 mm, 200 mm, and 250 mm, respectively. Also, the ratios of cavity depth to pipe diameter ( $d/D$ ) for the three cavity depths under study are  $1/12$ ,  $2/12$  and  $4/12$ , respectively. The cavity length to depth ( $L/d$ ) ratio investigated varies from 0.5 to 4 and is tabulated in table 3-1.

### 3.3 Basic Geometry

For each cavity configuration, a base seat with sharp upstream and downstream edges is investigated. Base seats are designed for this purpose. A schematic drawing of the cavity design with base seats installed is shown in figure 3-4. The two base seats with sharp edges are made of aluminum. They are of 50 mm thickness, 200 mm outer diameter and 150 mm inner diameter. These seats fit inside two flanges of 25 mm thickness and are inserted at the cavity upstream and downstream edge. The case where the base seats are inserted at the upstream and downstream of the cavity will be considered a reference case. This reference case is used to demonstrate the effectiveness of the suppression seats in reducing and/or delaying acoustic resonance. The suppression seats are made of aluminum as well and have the same outer/general configuration as the base seats. All aluminum seats are bolted to the side disks at cavity upstream and downstream edges.

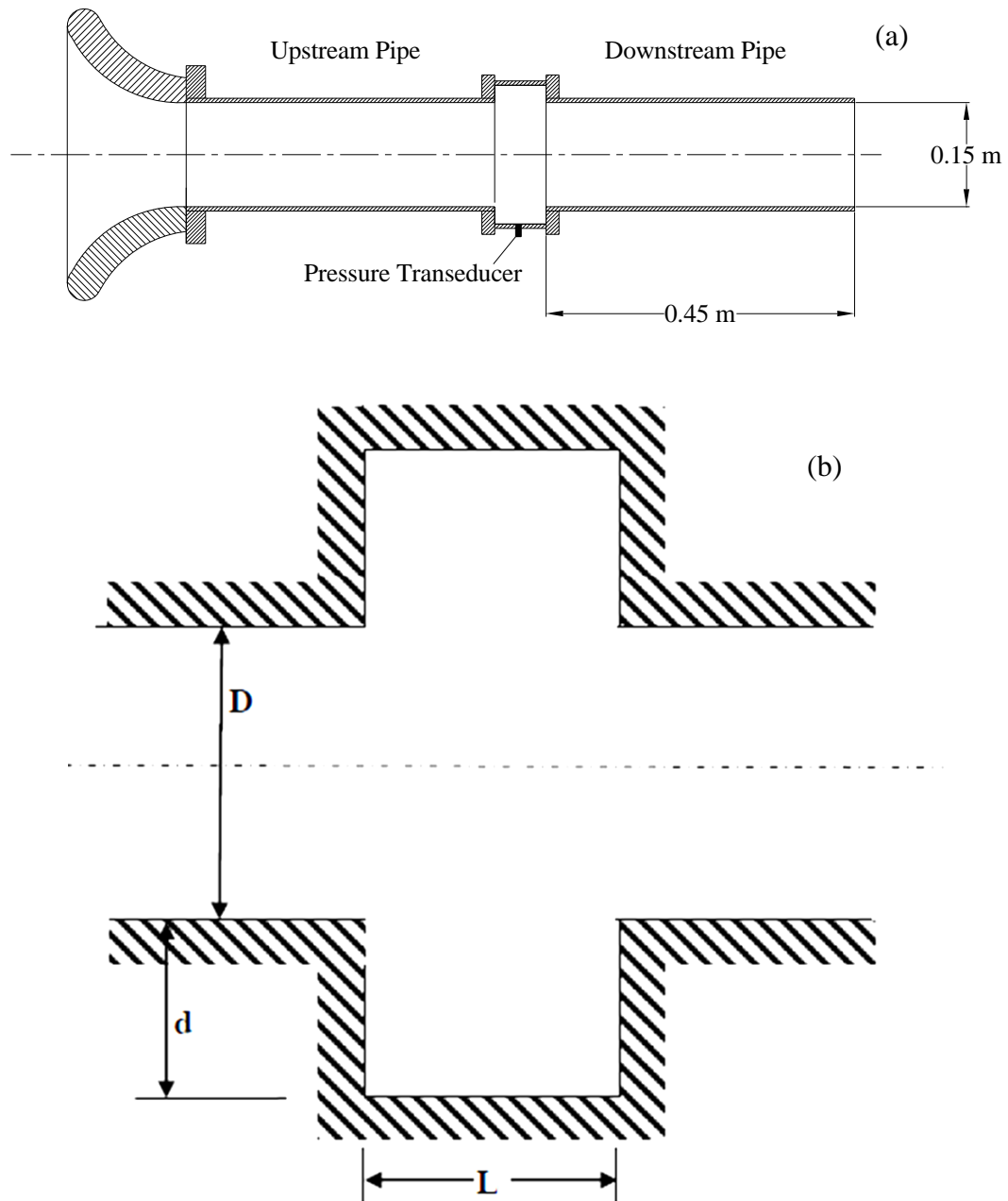


Figure 3-3 (a) Schematic drawing of the test section showing the inlet bell-mouth and the axisymmetric cavity-duct system (Aly, 2008), (b) Dimensions of the axisymmetric cavity

It should be mentioned that for the 25 mm cavity depth ( $d/D=2/12$ ), the two base seats upstream and downstream the cavity are used for reference case as shown in figure 3-4. The upstream base seat is replaced by the suppression seats in case of chamfer seats and spoiler seats. For the rounding case, both upstream and downstream base seats are replaced with the suppression seats. For the 50 mm cavity depth ( $d/D=4/12$ ), only upstream base seat was installed and tested as reference case. The downstream base seat is not needed for the two inch deep cavity since rounding the edges are not tested for this cavity. For the 12.5 mm cavity depth ( $d/D=1/12$ ), no sharp edge seats used for the base case. The sharp edges of the cavity are formed by the ends of the 150 mm main duct diameter. To test the suppression devices an altered flange is placed at the upstream edge of the cavity.

All seats; base and suppression seats, were first designed and manufactured for the 25 mm (one inch) deep cavity. To investigate these seats for deeper cavity i.e. the 50 mm (two inch) deep, a spacer ring is used. Figure 3-5 shows the details of spacer ring that was constructed to help fitting seats in deeper cavities. The spacer ring is also made of acrylic, of 200 mm inner diameter, 262 mm outer diameter. The ring consists of 3 sections; two identical rings of 19 mm thickness and four rectangular blocks of 38 X 32 X 12 mm where the 3 sections are glued to each other. The inner and the outer side of the four rectangular blocks were rounded. In this way the spacer ring would fit in between the flange and the aluminum seats. O-rings are used to seal the interface between different parts. The spacer ring is bolted to the side disk of 50 mm (two inch) deep cavity. On the other hand, aluminum seats will not fit in shallower cavity; 12.5 mm (half inch) deep cavity. As a result, two 12.5 mm deep flanges are altered to fit the suppression seats. These suppression seats are of 12.5 mm thickness and explained in detail later. The two flanges are of 12.5 mm and 25 mm thickness.

With the setup described above, the cavity length can be changed from 25 mm (one inch) to 50 mm (two inch) with the ability of adding and removing two acrylic flanges of 12.5 mm thickness. This sequence of arrangement allowed the pressure transducers to be always located halfway the cavity length. All parts are braced together using threaded rods. Air leakage to and from the test section is

obstructed by placing O-rings at all the interfaces between the different parts of the test section, as shown in figure 3-4. Moreover, O-rings minimize the acoustic losses due to the fluctuation of the air leakage with the acoustic pressure.

**Table 3-1 Dimensions of tested cavities**

d (mm/inch)	Ratio d/D	Tested ratios of L/d
12.5 (Half inch)	1/12	2, 4
25 (one inch)	2/12	1, 2
50 (two inch)	4/12	0.5, 1

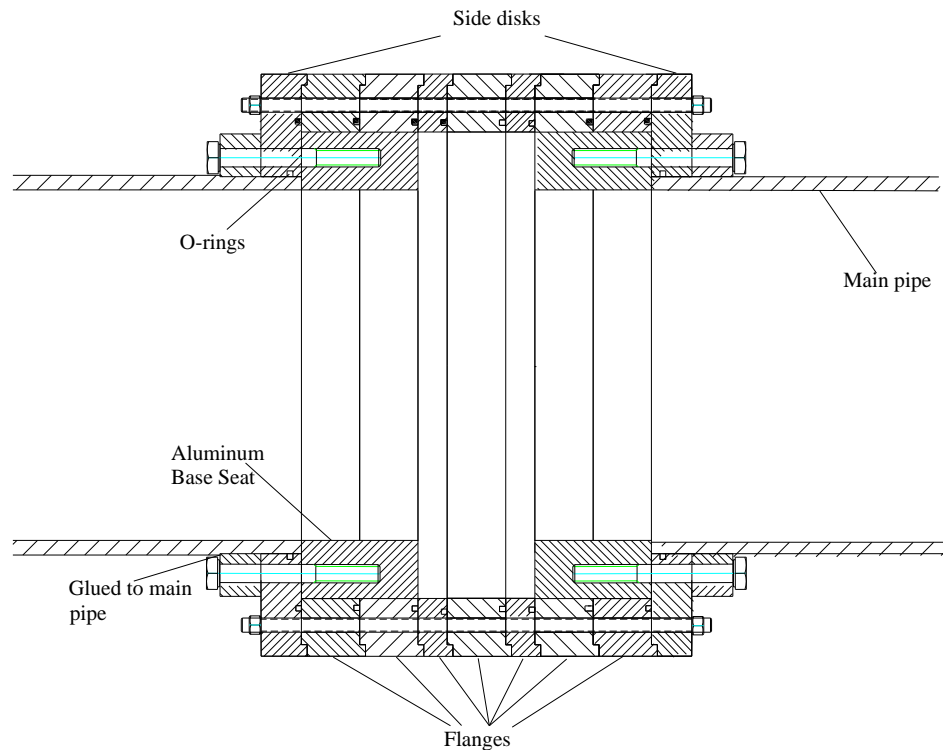


**Figure 3-4 Schematic drawing of the cavity design with base seat installed, cavity depth is 25 mm and cavity length is 50 mm.**

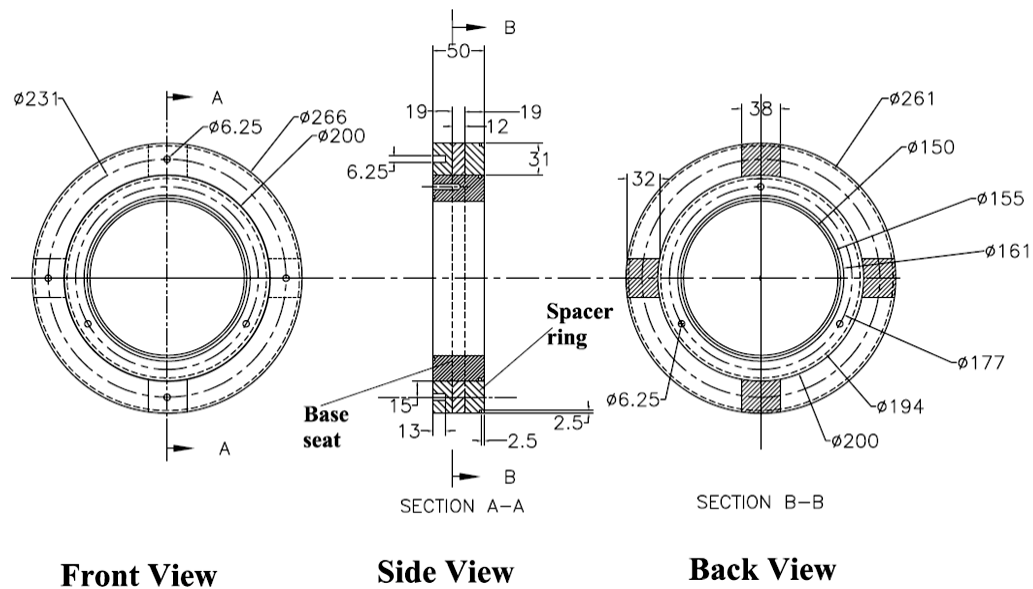


Figure 3-5 Spacer-ring with base seat in place used to help fit aluminum seats in deeper cavity

### 3.4 Approach Flow characteristics

In this section, the results of the approach flow measurements and the characteristics of the boundary layer at the cavity upstream separation edge are presented. These measurements were conducted by Aly (2008). The measurements ascertained the mean velocity profile, the distribution of the streamwise velocity fluctuation, the displacement thickness and the momentum thickness.

Aly (2008) developed the test setup used to perform the experimental study presented in this chapter. He reported hotwire measurement to characterize in detail the approach flow and most importantly the boundary layer at the cavity leading edge. Since the upstream of the cavity in this experiment was not changed, the approach flow characteristics remain the same.

The radial mean velocity profiles were measured for different flow velocities ranging from 31 m/s to 79 m/s. Figure 3-6 shows a typical radial profile of mean velocity for 31 m/s reference mean velocity. This figure shows that the boundary layer at the cavity upstream separation edge is relatively thin compared to the pipe

diameter; the boundary layer thickness is about 20 mm for the 31 m/s case. For the measured cases, Aly (2008) reported that “the data showed a decrease in the boundary layer thickness as the velocity increases. At 79 m/s, the boundary layer thickness is reduced to about 12 mm. Outside of the boundary layer; the standard deviation of the mean velocity is 0.35%”.

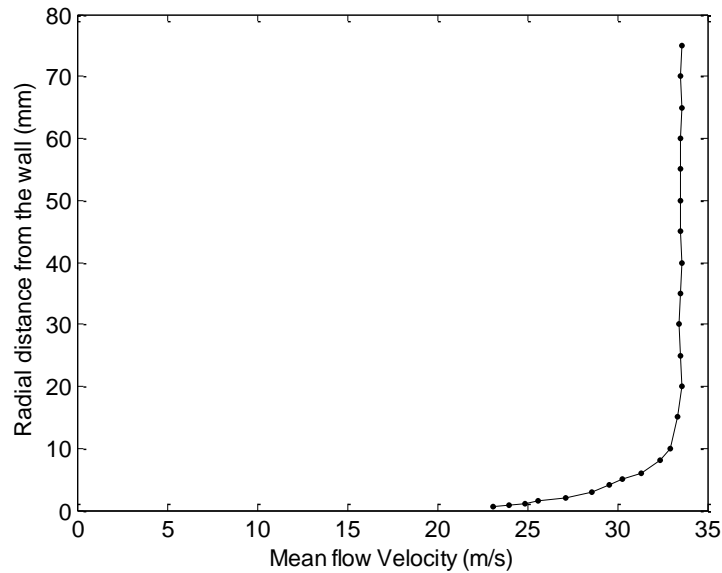


**Figure 3-6 At reference velocity of 31 m/s, the radial profile of mean velocity at upstream edge of the cavity and at the end of the bell mouth (Aly, 2008)**

Aly (2008) showed for all velocity measurements, that the RMS amplitudes mean flow fluctuations outside the boundary layer are fixed (see figure 3-7). This amplitude represents the mean flow fluctuations instead of turbulence fluctuations, and is about 2% of the mean flow velocity. Also, figure 3-7 shows that the velocity RMS amplitude increases within the boundary layer. The maximum amplitude is attained close to 2mm from the wall. Aly(2008) also found that as the mean flow velocity increases, this maximum amplitude decrease monotonically. For instance, at 31 m/s mean flow velocity the maximum amplitude was 8.5% while at 79 m/s mean flow velocity the maximum amplitude was 6.5%.

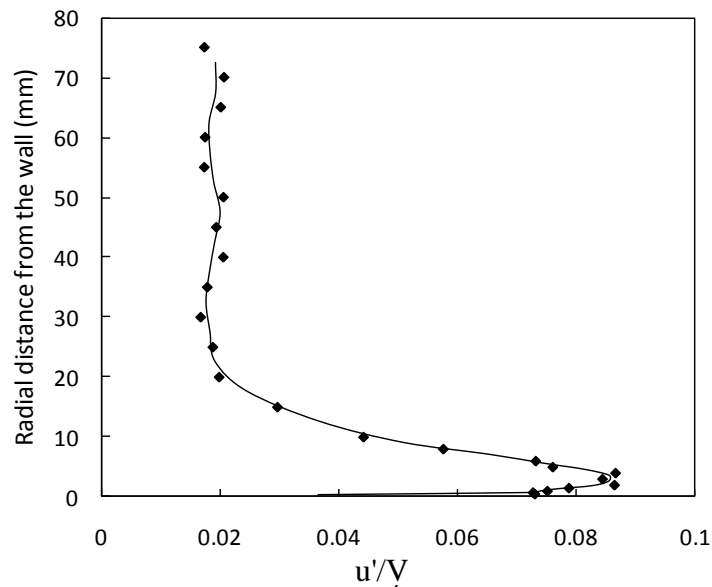


**Figure 3-7 Radial distribution of the dimensionless RMS amplitude of fluctuation velocity at the cavity upstream edge for reference velocity of 31 m/s at the end of the bell mouth (the continuous line is a moving average of the measurement data), (Aly, 2008)**

Table 3-2 records the measured and calculated quantities by Aly (2008) of the boundary layer thickness, displacement thickness, momentum thickness and the shape factor at different flow velocities in the test section. These values indicate a decrease in the displacement and momentum thicknesses with the increase of the velocity. Moreover, the shape factor is nearly constant and resembles the shape factor for the turbulent boundary layer over a flat plate.

**Table 3-2 List of displacement thickness, momentum thickness, shape factor, and boundary layer thickness at different flow velocities (Aly, 2008)**

Average velocity (m/s)	Displacement Thickness (mm)	Momentum Thickness (mm)	Shape Factor	Boundary layer Thickness (mm)
31	1.28	0.92	1.39	20
40	1.21	0.873	1.38	16
56.5	1.09	0.834	1.31	15
79	1.05	0.79	1.33	12

### 3.5 Characteristics of acoustic-shear layer coupling

Cavity oscillations are created when unstable shear layer graze over a cavity. These oscillations are self-sustained by a feedback excitation mechanism. The type of cavity oscillation depends on the nature of the upstream feedback. Rockwell & Naudascher (1978) classified this excitation mechanism into three categories: 1) fluid-dynamic, 2) fluid-resonant (current study case), and 3) fluid-elastic oscillation.

Impinging shear layer flows are sustained by the fluid dynamic mechanism. The impingement of cavity free shear layer; the first component, is characterized by its ability to sustain a moderate level of organized oscillations. These self-sustained oscillations involve a number of events (Rockwell, 1983). First, the oscillating flow impingement at downstream edge of the cavity generates a pressure pulse that travels upstream. The pressure pulse perturbs the free shear layer at the separation edge causing it to oscillate. As the free shear layer progresses downstream, the initial perturbation grows and forms a new vortex structure. The new vortex impinges on the downstream edge and generates a new pressure pulse that starts new feedback cycle. These events constitute the self-excitation mechanism which generates and sustains the shear layer oscillations.

The second type of self-excited cavity oscillation, the fluid-resonant feedback mechanism (current study case), is produced by the coupling between the free-shear layer oscillation and a resonant acoustic field. In these types of flows, part of the oscillating mean flow energy is transferred to acoustic energy. Most of energy transfer takes place near the downstream edge. This energy sustains the acoustic resonance. The oscillating acoustic resonance fluid in turn generates a strong vorticity fluctuation at the separation region of the shear layer. As the free shear layer progresses downstream, the initial perturbation grows and forms a new vortex structure. The new vortex transfers energy to the acoustic field as it moves close to the downstream edge and closes the feedback cycle.

The energy transfer between the free shear layer and the acoustic field depends strongly on the acoustic field characteristics. To understand the characteristics of the acoustic resonance of diametral modes, numerical

simulations of the cavity-duct system domain, with no flow, were conducted by Aly (2008) to determine the mode shapes of the acoustic resonance. A finite element commercial package (ABAQUS) is used to perform these simulations. The results of the simulations showed that the frequencies of diametral modes decrease slightly with the increase of cavity dimensions.

Figure 3-8 shows the mode shapes of the first three diametral acoustic modes for a cavity with  $L/d = 1$  attached to 450 mm long pipes at both ends. The diametral modes are shown in the form of normalized acoustic pressure contours. It is clear from figure 3-8 that the diametral modes are locked to the cavity where the darkest and brightest areas represent the maximum pressure amplitudes, and are out of phase with each other.

The simulation also provided the main characteristics of the acoustic modes. First, the maximum acoustic pressure appears to exist halfway the cavity length and at the cavity floor. Secondly, the acoustic pressure varies in the form of sine function over the cavity circumference. In addition, the mode number is defined as the number of the complete sine cycles made by the acoustic pressure over the circumference.

The acoustic particle velocity field is deduced from the mode shapes of each acoustic mode. The importance of the acoustic particle velocity in the excitation process has been demonstrated by Howe (1980). He showed that the acoustic power generated by flow vorticity due to its convection in a sound field can be calculated using the following equation:

$$\mathcal{P} = \int (\rho \int \overline{\boldsymbol{\omega}} \cdot (\overline{\mathbf{V}} \times \overline{\mathbf{U}}_a) dV) dt \quad 3-1$$

where,  $\mathcal{P}$ , is the power generated, or absorbed, by the vorticity field,  $\overline{\boldsymbol{\omega}}$  is the vorticity vector,  $\overline{\mathbf{V}}$  is the mean flow vector and  $\overline{\mathbf{U}}_a$  is the acoustic particle velocity vector. The vorticity vector  $\overline{\boldsymbol{\omega}}$ , can be decomposed into steady state vorticity and fluctuating vorticity vectors. Aly (2008) showed that the particle velocity amplitude at the cavity mouth increases with the increase of the cavity depth. As can be shown from equation 3-1, the acoustic power generated and consequently the acoustic pressure amplitude are proportional to the particle velocity amplitude.

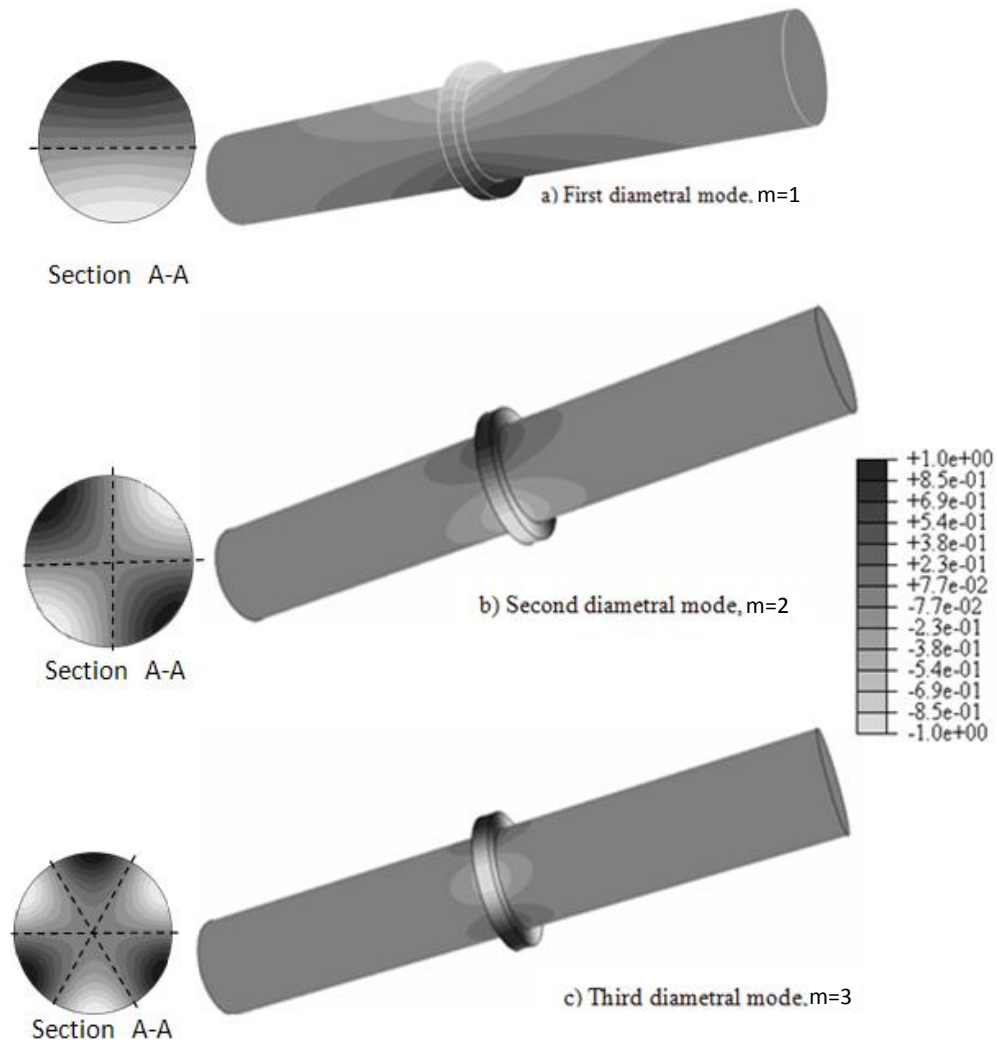


Figure 3-8 The mode shapes of the first, second and third acoustic resonance modes.  $L/d=1$ ,  $d/D=2/12$  (Aly, 2008)

Another factor that controls the amplitude of the acoustic pressure is the acoustic power radiation. The level of acoustic power radiation from the pipe terminations depends on the shape of the resonance mode and on the boundary conditions at the pipe terminations. The pressure amplitude of the diametral

modes decays exponentially along the main pipe further away from the cavity. Figure 3-9 shows the pressure decay with axial distance from the cavity centre. The decay distributions are obtained from the results of the finite element simulations of the acoustic modes for different cavity dimensions done by Aly (2008).

Aly (2008) found that for the one inch long cavity, the pressure amplitude of the first diametral mode at the pipe end for half inch deep cavity ( $L/d = 2$  and  $d/D = 1/12$ ), is about 20% of the amplitude at the cavity floor. And for the one inch deep ( $L/d = 1$  and  $d/D = 2/12$ ), it is about 2.5%. While for the two inch deep cavity ( $L/d = 0.5$  and  $d/D = 4/12$ ), it is about 0.1%. This indicates the relative increase in the acoustic radiation losses from the pipe ends as the cavity gets shallower. It is evident therefore that the acoustic pressure decays faster with the increase of the cavity depth. Thus as the cavity becomes deeper, the acoustic resonance will become stronger because less acoustic energy will be radiated from the system.

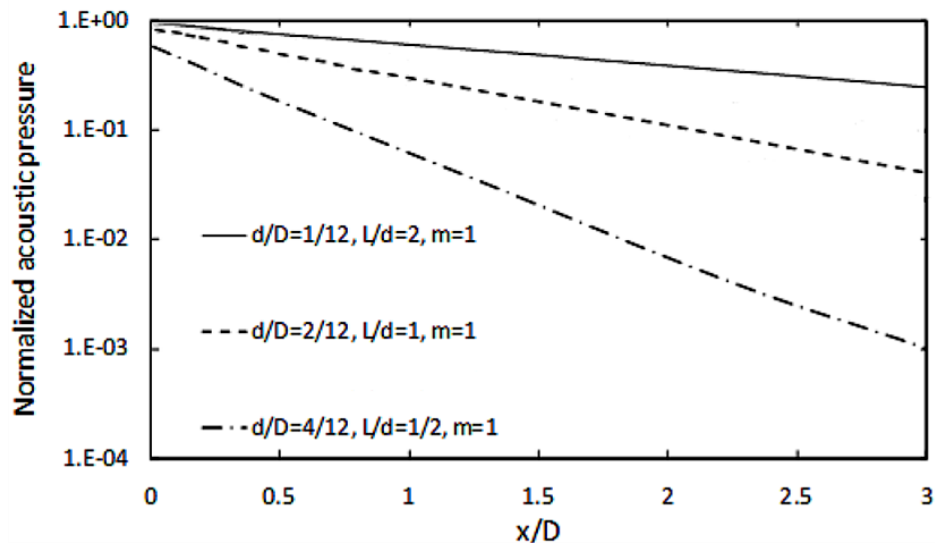
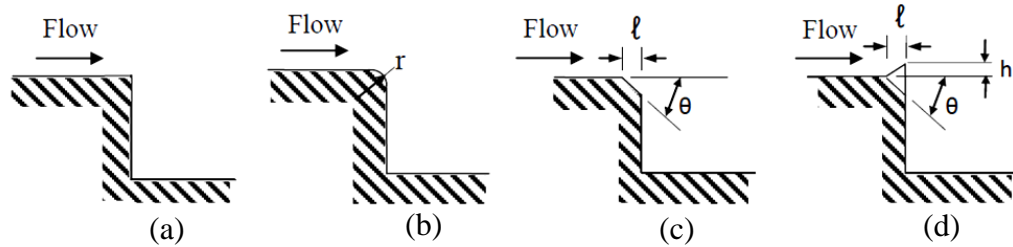


Figure 3-9 Axial distribution of acoustic pressure decay of the first diametral mode for various cavity dimensions,  $m$  is the acoustic mode order,  $x$  is measured from the cavity center, (Aly, 2008)

### 3.6 Suppression seat geometry

Before describing in detail the suppression seats tested in this study, sketches of the four (a-d) different configurations of the cavity leading edge is shown in figure 3-10. Sketch (a) shows the cavity leading edge with sharp edge which is the configuration of the base case or the reference case in this study. The second sketch (b) shows the cavity with rounded or filet edge of radius of curvature ( $r$ ). From reviewing the literature it is concluded that rounding the cavity edges was studied for different cavity configurations. The downstream edge of the cavity and/or the upstream edge are rounded in these studies. The ratio of rounding radius to cavity length ( $r/L$ ) that were investigated previously ranged between 0.1 – 1.0 (Bruggeman et al., 1991, Knotts & Selamet, 2003, and Nakiboğlu et al., 2010). In the current study, rounded upstream and downstream edges of the cavity are investigated for ( $r/L$ ) range of (0.1-0.2). The third sketch (c) is for chamfering the upstream edge of the cavity. In the literature, the chamfer is also referred to by bevel or downward ramp. Previous research showed that chamfering the upstream edge or both upstream and downstream edges of the cavity results in delaying the onset of resonance (Smith & Loluff, 2000, Janzen et al., 2007, and Knotts & Selamet, 2003). The ratio of chamfer length to cavity length ( $\ell/L$ ) as well as angle of inclination ( $\theta$ ) controls the effectiveness of the chamfer in delaying the onset of lock-on. The optimum values of these two parameters depend on cavity configuration and oscillation type. After reviewing the literature, two chamfer configurations are selected to be investigated. Both have the same angle of inclination ( $\theta=17^\circ$ ), but with different chamfer length ( $\ell$ ). Each of the two chamfers is tested for both cavity lengths (one and two inch long) under investigation. This combination results in testing ( $\ell/L$ ) ranges from (0.1-0.4). The fourth and the final sketch in figure 3-10 show the configuration of a square-tooth leading edge spoiler. Different configurations and sizes of the leading edge spoilers are tested in the current study. Leading edge spoiler is widely used to suppress successfully the various types of cavity flow oscillation (Rossiter, 1964, Bruggeman et al., 1991, and Karadogan & Rockwell, 1983).



**Figure 3-10 Different configurations of the cavity leading edge, (a) sharp edge (base case), (b) rounded edge, (c) chamfer, (d) spoiler**

The current study investigates four square-toothed spoilers. The general configuration of the square-toothed spoilers is presented in figure 3-11, which shows the main geometrical parameters of the spoiler. Also, the tabulated data in table 3-3 detail the specifications of each spoiler (1) to (4) tested in the current study. It should be mentioned that there are two more spoilers; named curved and delta spoilers, studied as well. The detailed specifications of the curved and delta spoilers are discussed later. The design of leading edge spoiler is based on the tested geometry of chamfer. The spoiler teeth are square shaped, as shown in figure 3-11. The teeth are designed by having consecutive upward and downward ramps, as shown in figure 3-11. The maximum height of a tooth is at the cavity separation edge. The angle of the downward ramp is constant and equals  $17^\circ$ , which is the same as the chamfer. The upward ramp angle changes from one spoiler to another to change the tooth height. The tooth height as well as its width is based on Bruggeman et al. (1991), height ( $H/L$ ) and width ( $g/L$ ) of the spoiler tooth to cavity length was of 0.14 and 0.08, respectively. In the present study, the number of teeth ( $N$ ) was chosen as an integer number. And the spacing between teeth ( $a=\alpha$  in degrees) was set to be double the tooth width ( $a=2g=2\beta$  in degrees). One purpose of this study is to determine the minimum spoiler teeth size that effectively suppresses acoustic resonance. Minimizing the size of the spoiler teeth is important in practical applications. This is because of the hydrodynamic pressure drop introduced by the spoiler proportional to the teeth size. Therefore, minimizing the spoiler teeth size ensures that only the minimum pressure drop is introduced to the system.

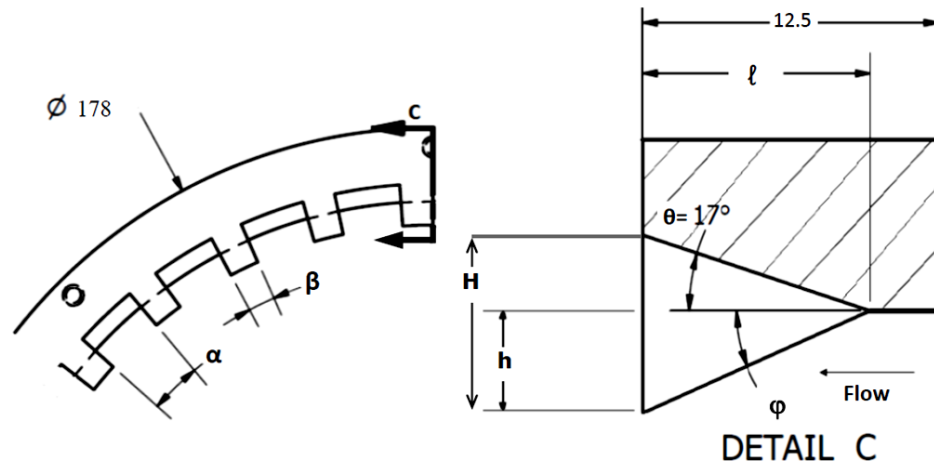


Figure 3-11 Schematic drawing of the saw-toothed spoiler, all dimensions in mm

Table 3-3 Dimensions of the square-toothed spoiler

Spoiler	$\alpha$ (deg)	$\beta$ (deg)	$\varphi$ (deg)	$l$ (mm)	$h$ (mm)	Number of teeth
Spoiler (1)	4	2	22	4.88	1.97	60
Spoiler (2)	8	4	22	9.75	3.94	30
Spoiler (3)	12	6	22	9.75	3.94	20
Spoiler (4)	12	6	32	9.75	6.10	20

### 3.6.1 Rounding cavity edges

Figures 3-12 and 3-13 show the detailed geometry of the rounded edge suppression seats. Two sets of suppression seats are constructed in this study. Each set has two seats, one for the upstream edge and another for the downstream edge. The first set has 5 mm (0.2 inch) rounding radius as shown in figure 3-12. The second set has 10 mm (0.4 inch) rounding radius as shown in figure 3-13. All seats have thickness of 50 mm, 200 mm outer diameter and 150 mm inner diameter. The seats are designed similar to the base seats. The seats fit inside the 25mm deep cavity flanges and bolted to the ends of the cavity inside walls similar to figure 3-4. O-rings are used to seal all the interfaces between the seats and all the adjustment points.

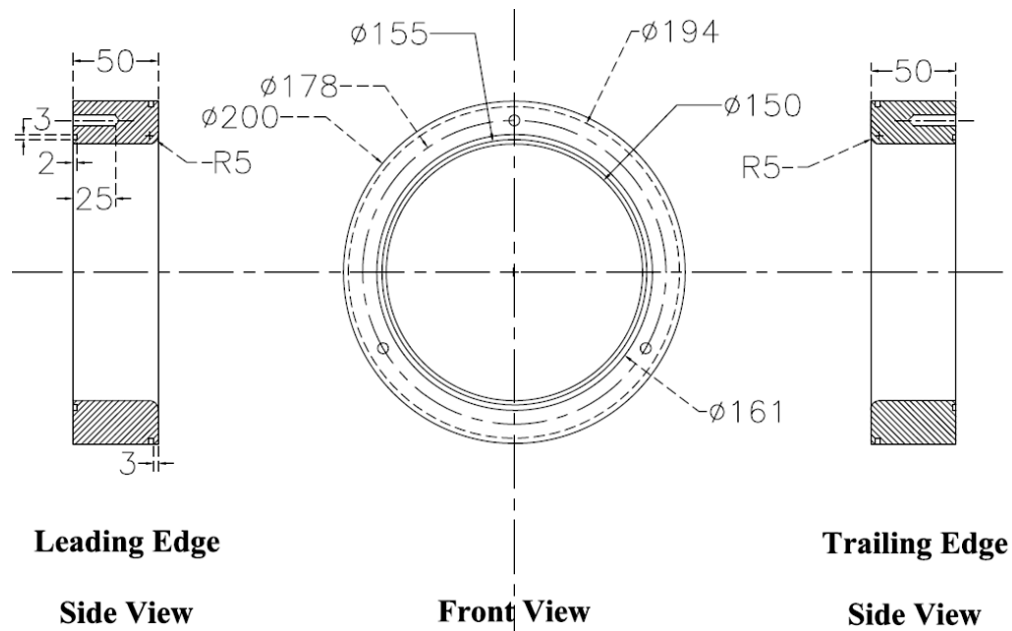


Figure 3-12 Rounded edges seat with radius of curvature of 5mm, all dimensions in mm

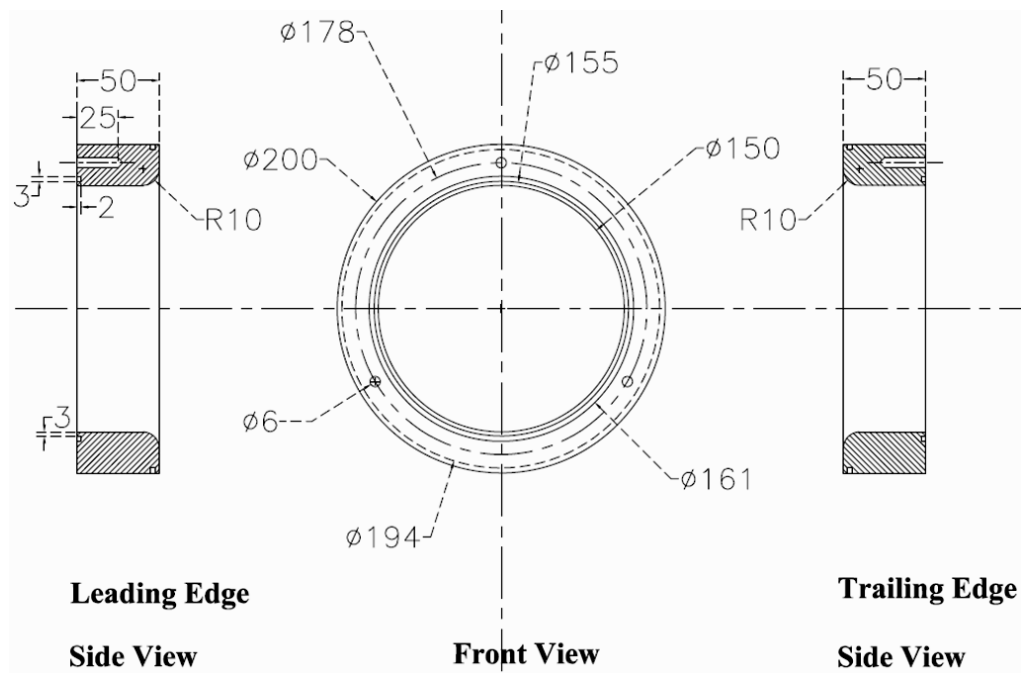


Figure 3-13 Rounded edges seat with radius of curvature of 10mm, all dimensions in mm

### 3.6.2 Upstream chamfering

Figures 3-14 and 3-15 show the detailed geometry of the chamfered edge suppression seats. Two sets of suppression seats are constructed in this study. Each set has two seats, one for the chamfered upstream edge and another for the sharp downstream edge. The first set has 4.88 mm (0.192 inch) chamfer length as shown in figure 3-14. The second set has 9.75 mm (0.384 inch) chamfer length as shown in figure 3-15. All seats have thickness of 50 mm, 200 mm outer diameter and 150 mm inner diameter. The seats are designed similar to the base seats. The seats fit inside the 25mm deep cavity flanges and bolted to the ends of the cavity inside walls similar to figure 3-4. O-rings are used to seal all the interfaces between the seats and all the adjustment points. For the 12.5 mm and the 50 mm cavity depths, the two sets of suppression seats consist of the upstream chamfered seats only. For the 50 mm (two inch) cavity depth, the spacer ring is used to help positioning the suppression seats into 50 mm deep flange. For the 12.5 mm (half inch) cavity depth, two chamfer rings made of acrylic are constructed by Rapid Prototype machine. The two suppression rings have the same chamfer lengths shown in figures 3-14 & 3-15. The suppression rings are of 12.5 mm thickness, 178 mm outer diameter, and 150 mm inner diameter. The rings would fit inside two 12.5 mm deep altered flanges. These two altered flanges are of 12.5 mm and 25 mm thickness. The suppression rings are fixed to the altered flanges with counter sink bolts.

### 3.6.3 Leading edge spoiler

Figure 3-16 shows the detailed geometry of the square toothed spoiler (1) ring. The design of leading edge spoiler is based on the chamfer geometry shown in figure 3-14. The spoiler teeth are square shaped. Spoiler (1) has the configuration of 60 teeth; 4.88 mm chamfer length, 3.5 mm tooth height from the base, 2° tooth width, and 4° spacing between the teeth. The spoiler ring is made of acrylic constructed by a Rapid Prototype machine. The ring has thickness of 12.5 mm, 175 mm outer diameter and 150 mm inner diameter. The spoiler ring fit

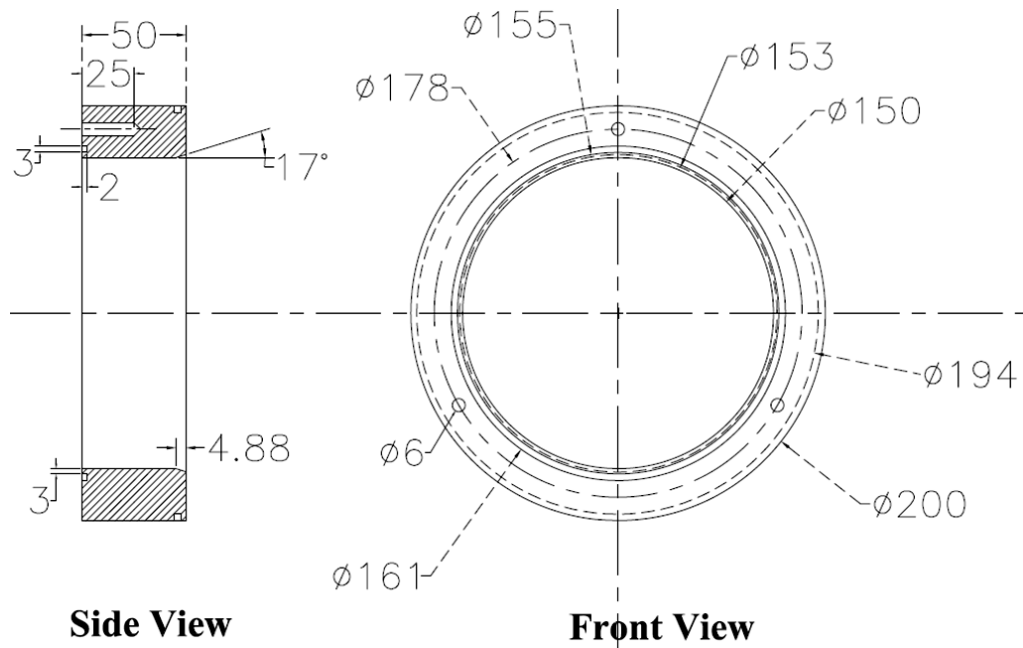


Figure 3-14 Chamfer seat with chamfer length of 4.88mm, all dimensions in mm

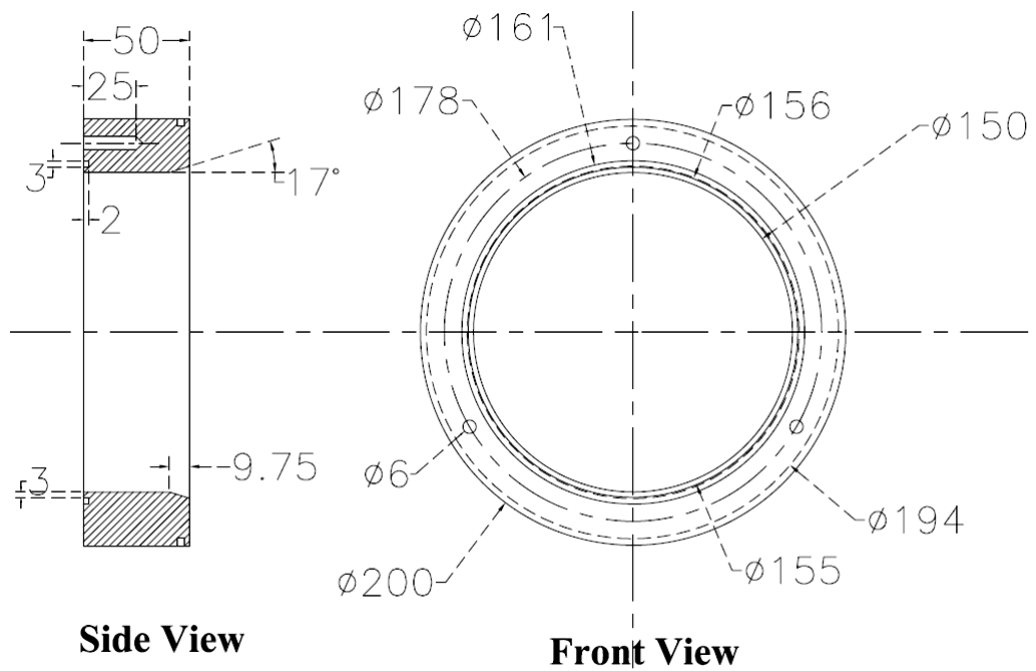


Figure 3-15 Chamfer seat with chamfer length of 9.75mm, all dimensions in mm

inside the 50 mm thickness altered aluminum seat shown in figure 3-17. The altered aluminum seat is of 200 mm outer diameter and 150 mm inner diameter. The altered aluminum seat fit inside two flanges of 25 mm thickness and is installed at the cavity upstream. The ring is fixed to the altered aluminum seat with counter sink bolts. The aluminum seat fit inside the 25 mm deep cavity flanges and bolted to the ends of the cavity inside walls similar to figure 3-4. O-rings are used to seal all the interfaces between the seat, ring, and all the adjustment points.

Figure 3-18 show the detailed geometry of the square toothed spoiler (2) ring. The design of leading edge spoiler is based on the chamfer geometry shown in figure 3-15. Spoiler (2) has the configuration of 30 teeth; 9.75 mm chamfer length; 7 mm tooth height and  $4^\circ$  tooth width, and  $8^\circ$  spacing between the teeth. The spoiler (2) has the same outer configuration as spoiler (1). The spoiler ring fit inside the 50 mm thickness altered aluminum seat shown in figure 3-17. The ring is fixed to the altered aluminum seat with counter sink bolts. The aluminum seat fit inside the 25 mm deep cavity flanges and bolted to the ends of the cavity inside walls similar to figure 3-4. O-rings are used to seal all the interfaces between the seat, ring, and all the adjustment points.

Figure 3-19 shows the detailed geometry of the square toothed spoiler (3) ring. The design of leading edge spoiler is based on the chamfer geometry shown in figure 3-15. Spoiler (3) has the configuration of 20 teeth; 9.75 mm chamfer length; 7 mm tooth height and  $6^\circ$  tooth width, and  $12^\circ$  spacing between the teeth. The spoiler (3) has the same outer configuration as spoiler (1) and (2). The spoiler ring fit inside two 12.5 mm deep altered flanges. These two flanges are of 12.5 mm (half inch) and 25 mm (one inch) thickness. The spoiler ring is fixed to the altered flanges with counter sink bolts.

Figure 3-20 shows the detailed geometry of the square toothed spoiler (4) ring. The design of leading edge spoiler is based on the chamfer geometry shown in figure 3-15. Spoiler (4) has the configuration of 20 teeth; 9.75 mm chamfer length, 9 mm tooth height,  $6^\circ$  tooth width, and  $12^\circ$  spacing between the teeth. The spoiler ring fit inside the 50 mm thickness altered aluminum seat shown in figure 3-17. The ring is fixed to the altered aluminum seat with counter sink bolts. The

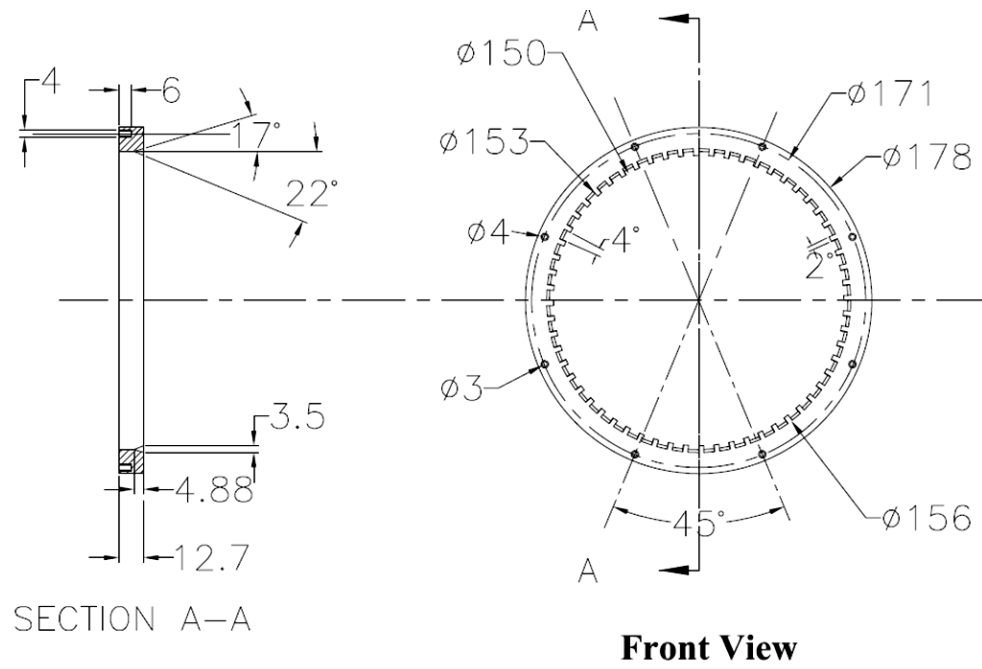


Figure 3-16 Detailed drawing of Spoiler (1), all dimensions in mm

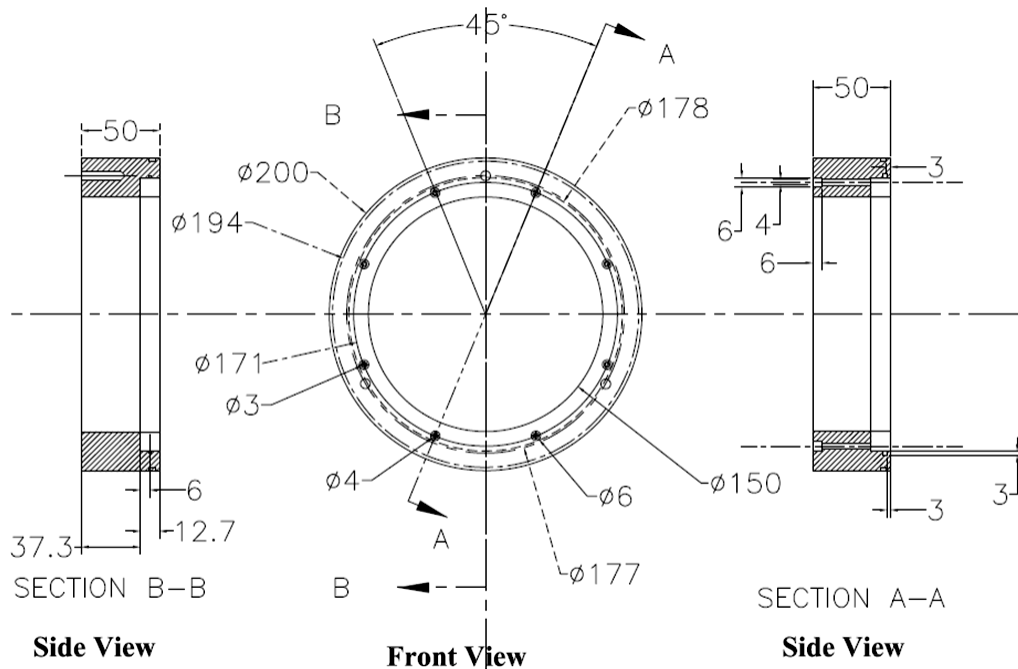


Figure 3-17 Altered aluminum seat to fit spoiler



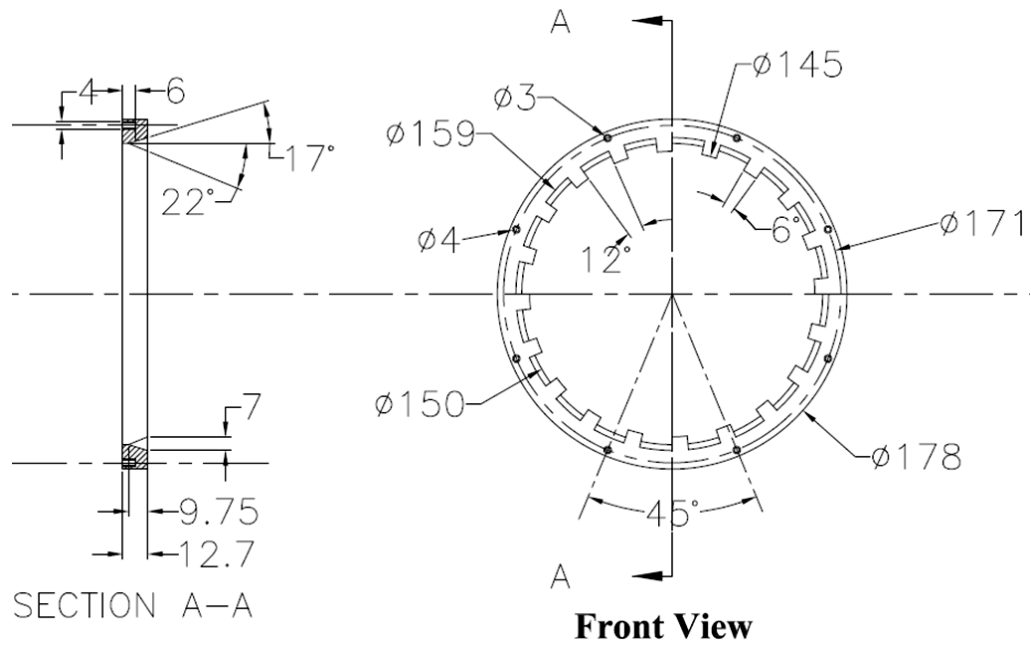


Figure 3-19 Detailed drawing of Spoiler (3), all dimensions in mm

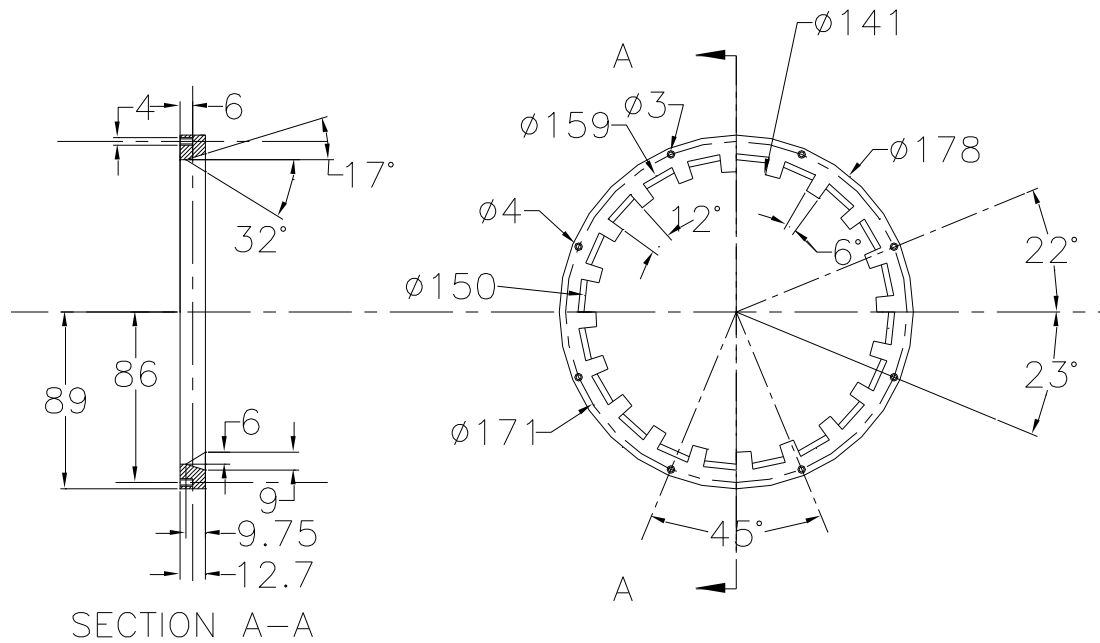


Figure 3-20 Detailed drawing of Spoiler (4), all dimensions in mm

seat, ring, and all the adjustment points. Photograph of curved spoiler is shown on figure 3-23(a).

Figure 3-22 shows the detailed geometry of the delta spoiler ring. Delta spoiler has the configuration of 18 mm thickness, 26 teeth, 6 mm tooth height, 2 mm and 4 mm tooth width at the tip and the base, respectively. The teeth have 30°- 32° angle of incident. Also, the delta spoiler has no chamfer. The spoiler ring fit inside the 50 mm thickness altered aluminum seat shown in figure 3-17. The aluminum seat is further altered to fit the new spoiler ring thickness. The ring is fixed to the altered aluminum seat with counter sink bolts. The aluminum seat fit inside the spacer ring shown in figure 3-5. The spacer ring helps positioning the altered aluminum seat and spoiler ring into 50 mm deep cavity flange. This arrangement is bolted to the ends of the cavity inside walls similar to figure 3-4. O-rings are used to seal all the interfaces between the seat, ring, and all the adjustment points. Photograph of delta spoiler is shown on figure 3-23(b). All data of suppression devices designed and tested for different cavity depths and lengths are tabulated in table 3-4.

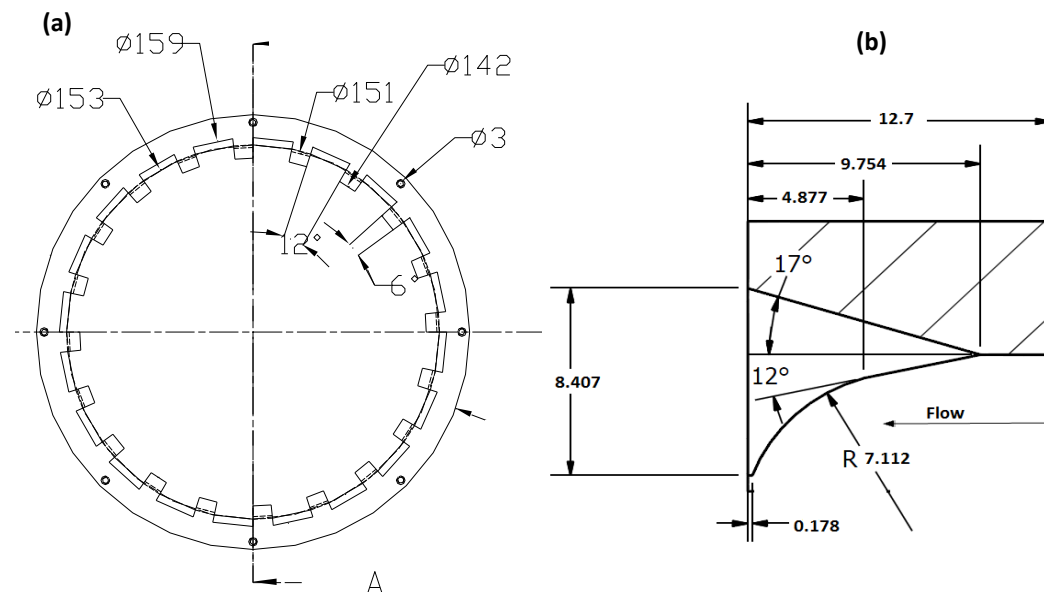


Figure 3-21 (a) Detailed drawing of Curved Spoiler, (b) Tooth details of spoiler, all dimensions in mm

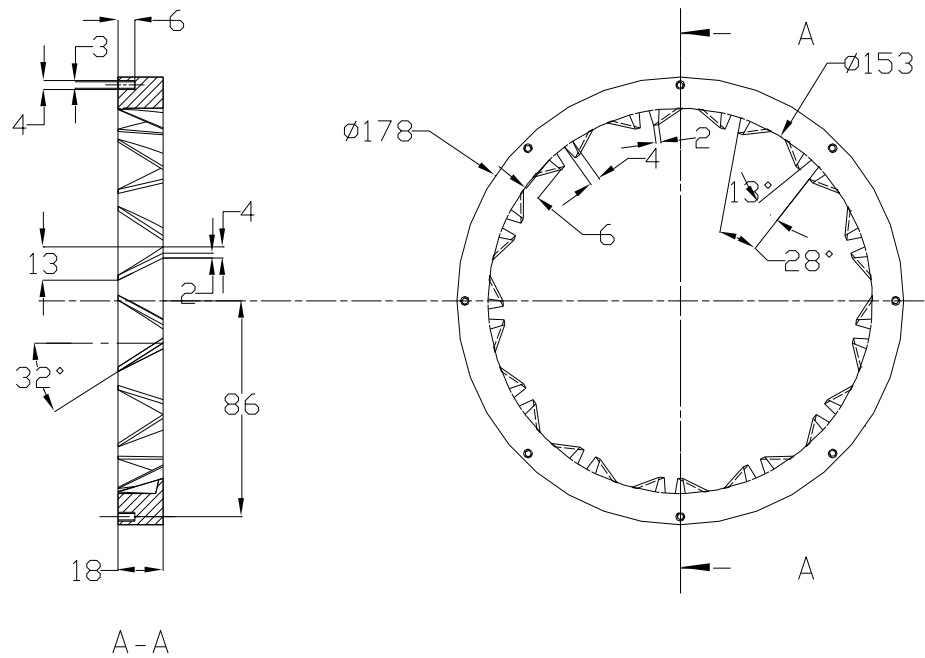


Figure 3-22 Detailed drawing of Delta Spoiler, all dimensions in mm

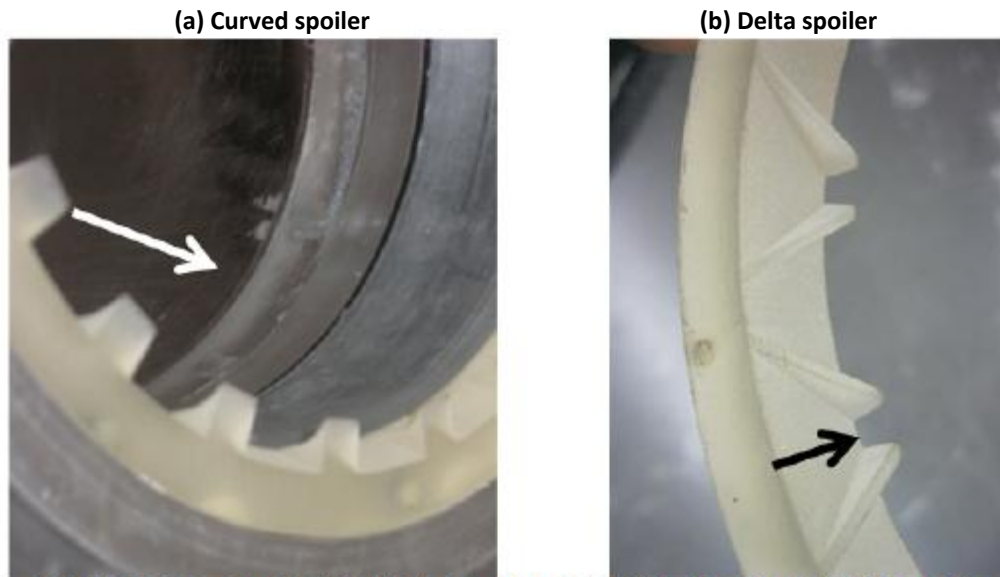


Figure 3-23 Photographs of (a) Curved spoiler and (b) Delta spoiler

Table 3-4 Suppression devices tested in different cavity dimensions

Suppression Method	Number of teeth (N)	Chamfer/down word ramp Length (ℓ)	Total Height of tooth from base (H)	Depth (d) = 1 inch		Depth (d) = 2 inch		Depth (d) = 12.5mm = ½ inch	
				L=25mm (L/d=1)	L=50mm (L/d=2)	L=25mm (L/d=0.5)	L=50mm (L/d=1)	L=25mm (L/d=2)	L=50mm (L/d=4)
Chamfer- 20% of 25mm (one inch)	----	ℓ=4.88mm=0.192inch	----	Y	Y	Y	Y	Y	N
Chamfer-20% of 50mm (two inch)	---	ℓ=9.75mm=0.384inch	----	Y	Y	N	N	N	Y
Spoiler (1)	60	ℓ=4.88mm=0.192inch	3.5mm=0.138inch	Y	Y	N	N	N	N
Spoiler (2)	30	ℓ=9.75mm=0.384inch	7.0mm=0.276inch	Y	Y	N	N	N	N
Spoiler (3)	20	ℓ=9.75mm=0.384inch	7.0mm=0.276inch	N	Y	N	N	Y	Y
Spoiler (4)	20	ℓ=9.75mm=0.384inch	9.0mm=0.354inch	N	Y	Y	Y	N	N
Curved Spoiler	20	ℓ=9.75mm=0.384inch	8.5mm=0.331inch	N	Y	Y	Y	N	N
Delta Spoiler	26	----	18.0mm=0.708inch	N	Y	Y	Y	N	N
Rounding-20% of 25mm (one inch)	---	r=5.1mm=0.2inch	----	Y	Y	N	N	N	N
Rounding-20% of 50mm (two inch)		r=10.2mm=0.4inch	----	N	Y	N	N	N	N

### 3.7 Instrumentation

The present testes include the measurements of the acoustic pressure amplitude and the mean flow velocity. A static pitot tube is used to measure the mean flow velocity. Four pressure transducers, for measuring the acoustic pressure, are used simultaneously. In the following subsections these instruments are approached.

#### (a) Pitot tube

The pitot tube is placed right after the bell mouth contraction. It is connected to a differential pressure transducer of Validyne diaphragm type. The transducer model no. is DP45-14. The pitot tube is used to measure the dynamic head at the centerline of the test section. After considerable amount of measurements over the cross section, it was established that the flow velocity is uniform within 0.5%. A pressure pump is used to calibrate the differential pressure transducer with help of electrical bridge. The standard of deviation resulted from this ancillary calibration is found to be 0.5% of the full scale.

#### (b) Pressure Transducer

Four pressure transducers are employed at 4 different angles at the circumference of the cavity floor. Figure 3-24 shows the relative positions of the pressure transducers within the cavity. These transducers are used simultaneously to measure the instantaneous acoustic pressure amplitudes. They are piezoelectric type sensors and are fitted on the level of the inner surface of the cavity floor. The vibration sensitivity is diminished by attaching an acceleration compensation sensing element to the pressure transducer. The transducer has a resonance frequency of 250 kHz and a sensitivity of 7.3mV/kPa.

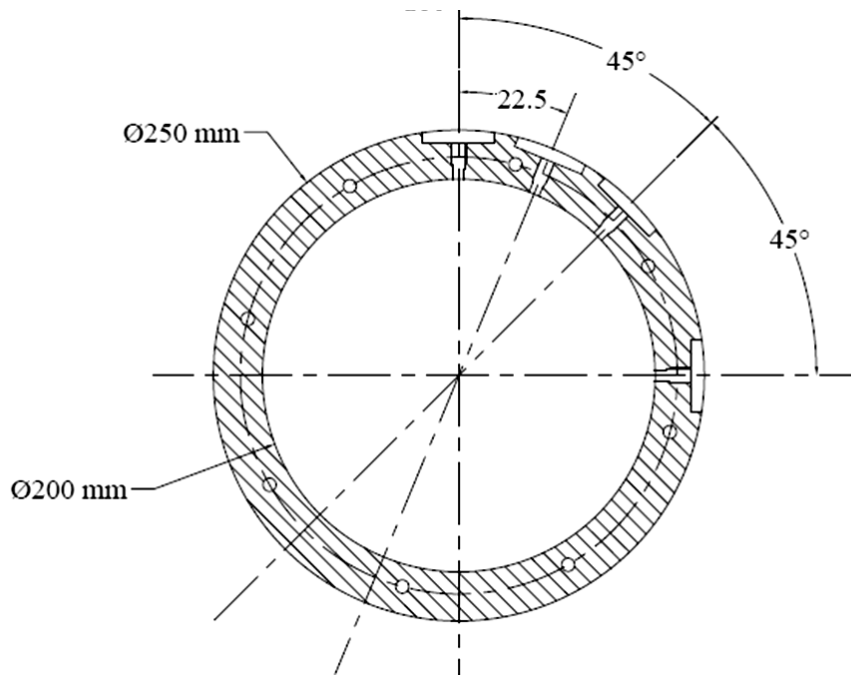


Figure 3-24 Location of pressure transducers, (Aly, 2008)

### 3.8 Experimental Procedures and Data Analysis

The approach for experiments is set to measure the acoustic pressure at the cavity floor. This is done for the different geometries of the cavity and over a range of mean flow velocity up to a Mach number of 0.4. The mean flow velocity is measured at the inlet of the test section by means of a pitot tube for the different blower rotational speed. Then the pitot tube is removed from the test section for the rest of the measurements. This is to ensure the uniformity of the flow entering the cavity. The blower rotational speed is then decreased constantly in steps. The step is selected to be 3.33% of the blower maximum speed. As a result, the flow velocity changes by approximately 3.33% of the maximum flow velocity. A complete error and uncertainty analysis is given in Appendix B. For each flow velocity, the amplitude spectrum of each pressure transducer signal is recorded. This is done at a sampling rate of 25000 point/sec i.e. sampling frequency is 25 kHz. Forty five averages of one second signal length are performed to obtain each spectrum. The data acquisition is performed using a 16-bit 4-channel National

Instrument card model PCI-4452. Analysis of recorded signals to produce the power spectra is done by Labview program. The labview program uses hanning windowing to produce a sine wave with no discontinues. The output of the labview program is a text file, which is then used as an input for FORTRAN program. This FORTRAN program was previously programmed by Aly (2008). What the FORTRAN program does is collecting the peaks of the pressure amplitudes from the four pressure transducers along the flow velocity, so saving the time to go and determine the peaks manually. Another input to the FORTRAN program is the calculated gradient from a plot drawn of the calculated flow velocity ( $V = \sqrt{2P/\rho}$ ) against blower frequency. The result of the FORTRAN program provides the pressure amplitudes of the four pressure transducers at the corresponding resonance frequencies. Also, the program picks the highest pressure amplitude of the four transducers and presents it. This result is plotted using excel file where the results of measurements as well as analysis are shown in the following chapter.

# CHAPTER 4

## Experimental Results

---

This chapter presents the experimental results obtained when adding passive suppression devices to cavity-duct system. This includes analysis and comparison to the corresponding reference/base cases for each cavity depth and length. The experimental measurements were performed for cavity-duct ratios of  $d/D=1/12$ ,  $2/12$ , and  $4/12$ . This corresponds to cavity depth ( $d$ ) of 12.5mm (half inch), 25mm (one inch), and 50mm (two inch), respectively. Different cavity depths are examined to explore the effect of the suppression methods in a more generalized prospective. The cavity length ( $L$ ) changes from 25mm (one inch) to 50mm (two inch). As a result, the cavity aspect ratio under study varies from  $L/d=0.5-4$ . The discussion here is based on the output of the experimental measurements performed on the test facility described previously. The discussion will begin with detailed analysis for one inch deep cavities with and without suppression seats. This is followed by, in the same manner, the half inch deep and the two inch deep cavities.

An overview of aeroacoustic response of the cavity-duct system is given in section 4.1. This is done by presenting the results of base cases for one inch deep cavities. In addition, the effect of suppression methods on the general aeroacoustic response, Strouhal number, reduced velocity, and acoustic pressure level is included. In sections 4.2 & 4.3 the effects of the suppression devices are extended to shallower (half inch deep) and deeper (two inch deep) cavities.

### **4.1 One Inch Cavity Depth ( $d=25\text{mm}$ )**

This section details the characteristics of the suppression of the diametral mode resonance using several leading edge inserts. For this purpose, the results of

base geometries with sharp leading and trailing edges will be first presented in detail. This is followed by the results of the suppression devices tested for these geometries. The base geometries throughout the study are given the symbol of B# (d, L). Two base geometries are studied in this section the first geometry is one inch deep and one inch long cavity and is denoted as B1 (1, 1). The second geometry is one inch deep and two inch long cavity, and is denoted as B2 (1, 2). Those base geometries will be used as reference to evaluate the effect of the suppression devices. The evaluation is based on the amplitude of acoustic pressure and frequency of the excited acoustic modes as function of flow velocity. In the rest of the chapter the acoustic modes and the free shear layer modes are denoted by (m) and (n), respectively.

#### **4.1.1 Acoustic response of base geometries B1 (1, 1) and B2 (1, 2)**

For each of the tested cavities, a number of acoustic pressure spectra were recorded for different flow velocities up to the highest capacity of the blower. Each spectrum is the average of 40 data samples, each of which is one second long yielding a spectrum with frequency resolution of one Hertz. The time signals were sampled at a frequency of 25 kHz. Figure 4-1 shows typical examples of pressure spectrum for a cavity with  $L/d=1$ ,  $d/D=2/12$  at three different flow velocities. For each of the three power spectrum, a single or multiple acoustic modes are excited. The excitation is demonstrated with a well-defined peak. It is noteworthy that the discussion, in this section, is based on the analysis of the power spectra of the pressure time traces, similar to the one shown in figure 4-1.

To gain overall perspective of the system behavior, the amplitude and frequency of the dominant peaks in the pressure spectra for base case B1 (1, 1) are presented in figures 4-2 and 4-3. Figure 4-2 shows the pressure amplitudes of the excited acoustic modes ( $m=1$  to 4) versus flow velocity. These acoustic modes are excited by shear layer modes ( $n=1$  & 2). The amplitude of the acoustic pressure ranges from approximately 6 Pa to 6400 Pa for the velocity range of 25 to 140 m/s which corresponds to Mach number of approximately 0.07 to 0.41. Figure 4-2

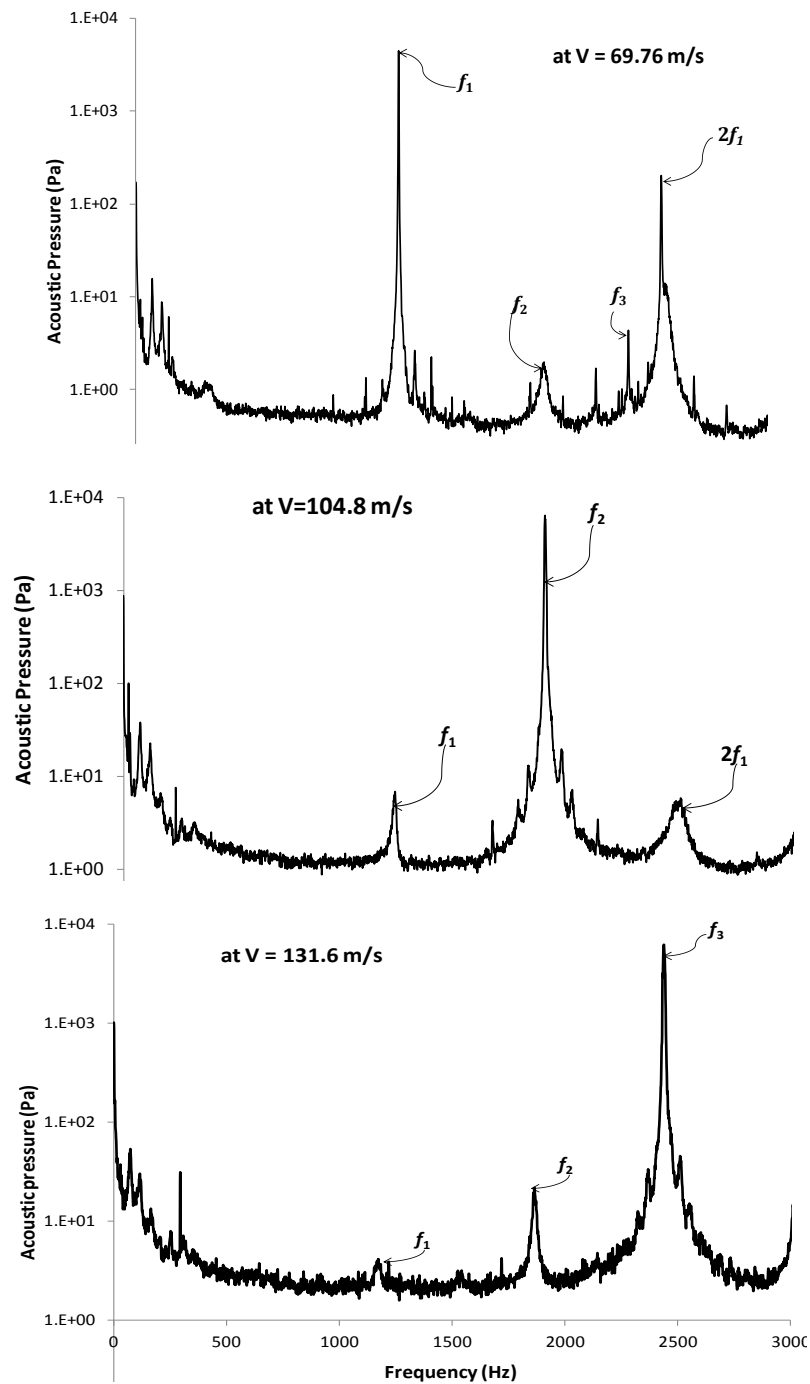


Figure 4-1 Acoustic pressure spectrum for cavity  $L/d = 1$ ,  $d/D = 2/12$  at different flow velocities,  $f_n$  is the frequency of mode  $m$ .

shows which mode is dominating according to the acoustic pressure amplitude as the flow velocity increases. As an example, the first acoustic mode ( $m=1$ ) is excited by the second shear layer mode ( $n=2$ ) from approximately 33 m/s until 45 m/s whereas the second acoustic mode ( $m=2$ ) is excited by the second shear layer mode ( $n=2$ ).

The resonance frequencies of the first four acoustic modes ( $m=1, 2, 3,$  and  $4$ ) excited by first, and second shear layer modes ( $n = 1,$  and  $2$ ) are shown in figure 4-3 against mean flow velocity for base case B1 (1, 1). Each data point in this plot is the frequency of the corresponding amplitude data point presented in the figure 4-2 at the same flow velocity. Clearly, the data points jump up and down from one dominant acoustic mode to another as the velocity increases. This behavior resembles the general trend of cavity excited acoustic resonance as reported by Schachenmann & Rockwell (1980). Also the plot shows that the resonance frequencies of the excited acoustic modes ( $m=1-4$ ) decrease slightly as the flow velocity increases. This trend is quite noticeable from the dotted lines indicated in the figure.

The shear layer modes excite the acoustic modes over specific ranges of Strouhal numbers. The Strouhal number is defined as ( $St=f L/V$ ); where  $f$  is the resonance frequency,  $L$  is cavity length, and  $V$  is the mean flow velocity. The Strouhal numbers are represented by the slope of the straight continuous lines shown in figure 4-3. These continuous lines represent the locus of the velocity and frequency at which each acoustic mode reaches peak pressure amplitude as shown in figure 4-2.

Presenting the base case B2 (1, 2) in the same manner, figures 4-4 and 4-5 show the amplitudes of the acoustic pressure and resonance frequencies for the excited acoustic modes as function of flow velocity. The behavior in this case is very similar to B1 (1, 1) discussed previously. In this case, the first three acoustic modes ( $m=1$  to  $3$ ) are excited. It should be pointed out that increasing the cavity length results in the change of the velocity range over which each acoustic mode is excited. Scrutinizing the results in figures 4-2 to 4-5 indicates clearly that the excitation by the first free shear layer mode ( $n=1$ ) is significantly stronger than the excitation by the second and third free shear layer modes ( $n=2$  &  $3$ ).

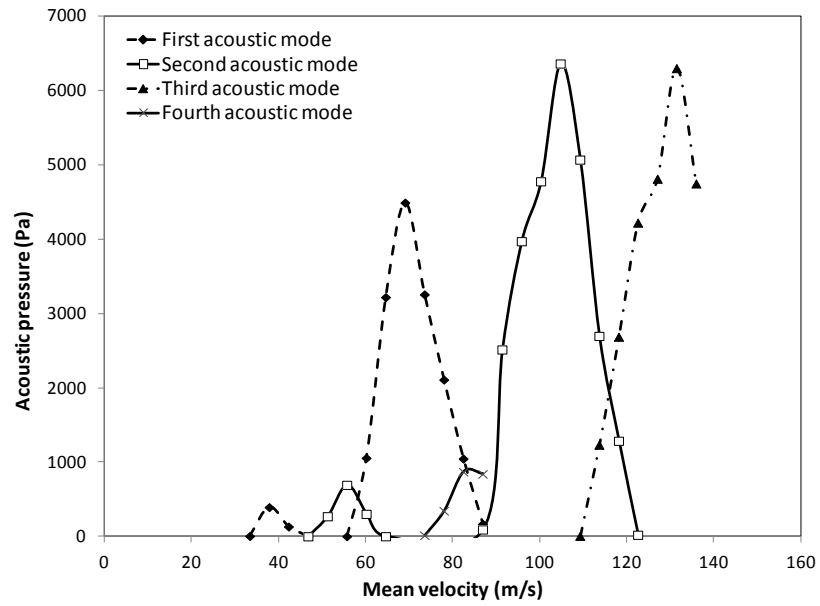


Figure 4-2 Pressure amplitudes of excited acoustic modes at different flow velocities for base case B1 (1, 1),  $d=25\text{mm}$ ,  $L/d=1$ ,  $d/D=2/12$

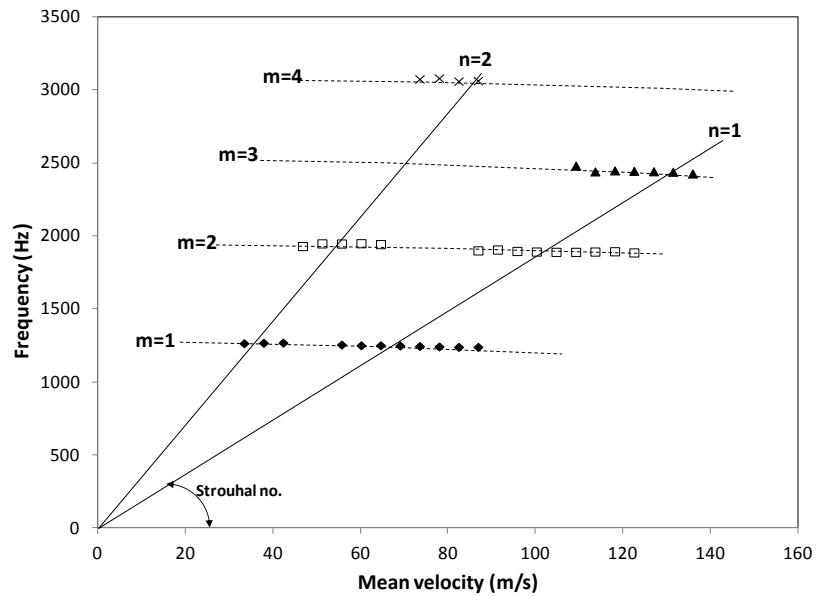


Figure 4-3 Frequency of excited acoustic modes at different flow velocities for base case B1 (1, 1),  $d=25\text{mm}$ ,  $L/d=1$ ,  $d/D=2/12$

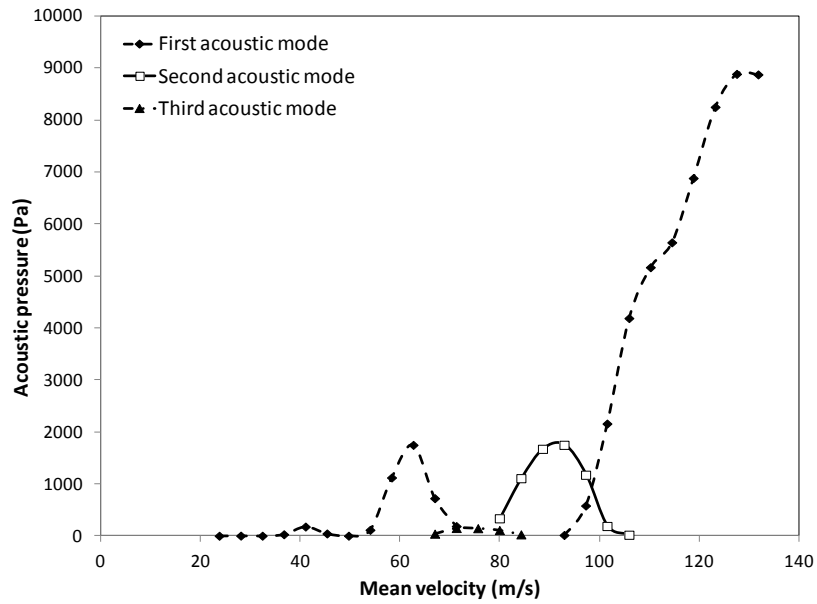


Figure 4-4 Pressure amplitudes of excited acoustic modes at different flow velocities for base case B2 (1, 2),  $d=25\text{mm}$ ,  $L/d=2$ ,  $d/D=2/12$

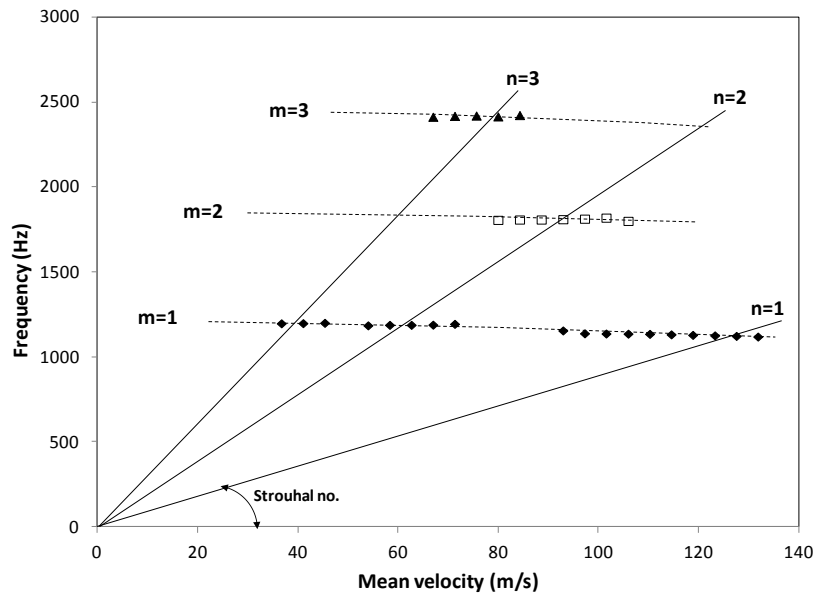


Figure 4-5 Frequency of excited acoustic modes at different flow velocities for base case B2 (1, 2),  $d=25\text{mm}$ ,  $L/d=2$ ,  $d/D=2/12$

The characteristics of the aerodynamic excitation of acoustic resonance are commonly being represented in terms of the Strouhal number and dimensionless pressure amplitude. Figure 4-6 is a plot of normalized acoustic pressure versus the Strouhal number for case B1 (1, 1). The acoustic pressure is normalized by dynamic head of mean flow ( $P/\frac{1}{2}\rho V^2$ ); where  $P$  is the acoustic pressure,  $\rho$  is the density of air and  $V$  is the mean flow velocity. The Strouhal number ( $St=f L/V$ ) is based on cavity length and the frequency of the excited acoustic mode. The first free shear layer mode excites the first three acoustic modes ( $m=1-3$ ). The Strouhal number of this mode ( $n=1$ ) ranged from 0.4 – 0.55. The maximum dimensionless pressure over this range is 1.6 and it corresponds to a Strouhal number of 0.5. The second shear layer mode ( $n=2$ ) has a Strouhal number range from 0.7 – 1.1. This mode ( $n=2$ ) excites the first, second, and fourth acoustic modes ( $m=1, 2, 4$ ). The maximum dimensionless amplitude excited by the second shear layer mode was 0.5 at a Strouhal number of 0.85.

Similar to figure 4-6, figure 4-7 shows the dimensionless pressure plotted against reduced velocity based on cavity length ( $V_r=V/fL$ ). The reduced velocity is the inverse of Strouhal number. Both the Strouhal number and the reduced velocity are dimensionless groups that represent the flow velocity. The main advantage of using the reduced velocity over the Strouhal number is that the reduced velocity is linearly proportional to the flow velocity. Whereas the Strouhal number is inversely proportional to the flow velocity. For this reason, figure 4-7 seems less confusing compared to figure 4-6. Therefore, the plot of dimensionless pressure against reduced velocity will be used throughout the study to avoid such confusion.

For the base case B2 (1, 2), figure 4-8 shows the dimensionless acoustic pressure ( $P/\frac{1}{2}\rho V^2$ ) as a function of the reduced velocity ( $V_r = V/fL$ ). As shown, excitation of acoustic modes ( $m=1$  & 3) by the third shear layer mode ( $n=3$ ) ranged from  $V_r = 0.55 - 0.7$  where the maximum dimensionless pressure of 0.2 occurs at a reduced velocity near 0.7. The second shear layer mode ( $n=2$ ) excites acoustic resonance over a reduced velocity range from 0.8 to 1.2. The maximum dimensionless pressure excited by the second shear layer is 0.7 and occurs at a reduced velocity of 1. The first shear layer mode ( $n=1$ ) excites the first acoustic

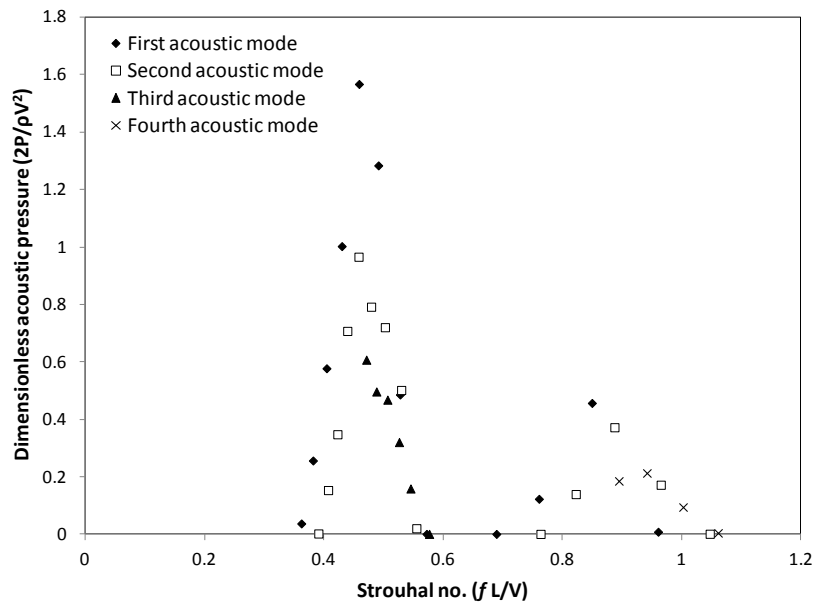


Figure 4-6 Dimensionless acoustic pressures ( $P/\frac{1}{2}\rho V^2$ ) versus Strouhal number ( $St=fL/V$ ) for base case B1 (1, 1),  $d=25\text{mm}$ ,  $L/d=1$ ,  $d/D=2/12$

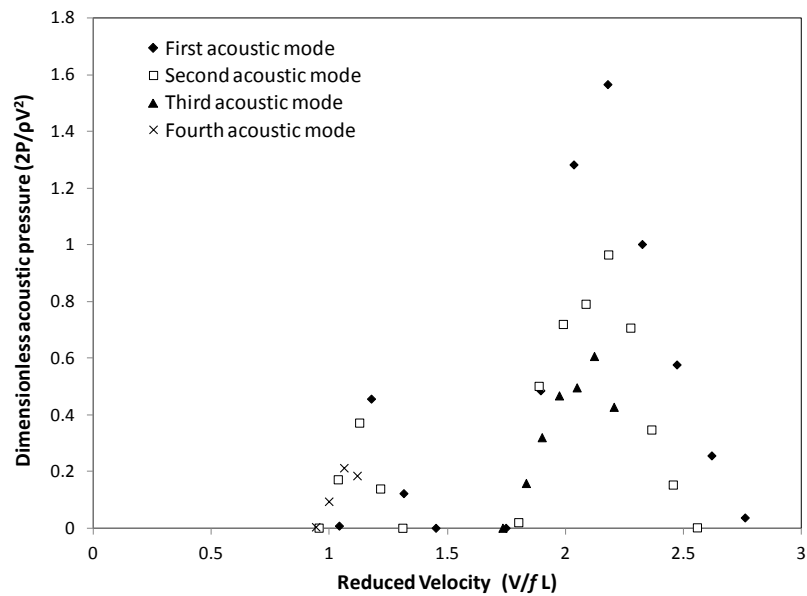


Figure 4-7 Dimensionless acoustic pressures ( $P/\frac{1}{2}\rho V^2$ ) versus reduced velocity ( $V_r=V/fL$ ) for base case B1 (1, 1),  $d=25\text{mm}$ ,  $L/d=1$ ,  $d/D=2/12$

mode ( $m=1$ ) for the range of reduced velocity starting from 1.6. The end of the resonance range by the first shear layer mode cannot be determined as it exceeds the velocity at the maximum capacity of the blower. However, the maximum dimensionless pressure of the first shear layer mode is 0.91 at a reduced velocity near 2.2.

The next sections present the results of different passive suppression devices tested for the one and two inch long cavities. All suppression devices (or seats) are tested at the upstream edge of the cavity except for rounding the edges which is tested at both upstream and downstream the edges simultaneously. The next sections show the effectiveness of each method in reducing the acoustic pressure and delaying the resonance.

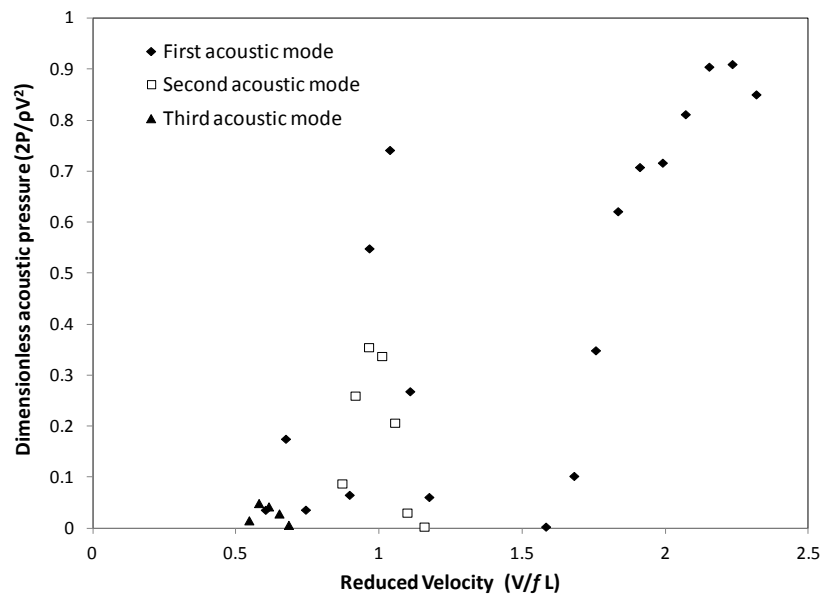


Figure 4-8 Dimensionless acoustic pressures ( $P/\frac{1}{2}\rho V^2$ ) versus reduced velocity ( $V_r=V/fL$ ) for base case B2 (1, 2),  $d=25\text{mm}$ ,  $L/d=2$ ,  $d/D=2/12$

### 4.1.2 Rounding the Cavity Edges

The effect of rounding the cavity edges on attenuating pressure amplitudes differ from one oscillation type to another. For instance, rounding off the trailing

edge of a rectangular cavity reduces the amplitude of the fluid dynamic oscillations in comparison with sharp edge (Ethembaoglu, 1973). On the other hand, for fluid resonant oscillations in deep cavities and closed side branches, it was found that rounding the cavity edges would increase pressure pulsation rather than reduce it (Brugguman et al. (1991), Tonon et al. (2011)). Similar features have been reported for corrugated pipes (Nakiboğlu et al. (2009), Nakiboğlu and Hirschberg (2010), Nakiboğlu et al. (2012)). In all this previous work, the ratio of the acoustic wavelength to the cavity length is relatively larger than the corresponding ratio of the configuration under study. The research objective of this section is to determine the impact of rounding the cavity edges on the pressure amplitude.

Based on the work reported in the open literature, the studied ratio of radius of curvature to cavity length ( $r/L$ ) ranges from 0.1 to 0.25 for either deep or shallow cavities. Accordingly, a rounding ratio of 0.2 is selected. First, the results of the cavity with one inch long ( $L/d=1$ ) are presented. Following the same sequence of presentation as the base case, figures 4-9 and 4-10 show the acoustic response after rounding the cavity edges in terms of acoustic pressure amplitudes and resonance frequencies versus mean flow velocity. Overall, the behavior in this case is very similar to B1 (1, 1) discussed previously. Figure 4-9 shows that only the first and second acoustic modes ( $m=1$  &  $2$ ) are excited over the flow velocity range from 42 m/s to 134 m/s. The pressure amplitudes of the excited diametral modes ranged from 272 Pa to 12560 Pa. The resonance frequencies of the excited acoustic modes ( $m=1$  &  $2$ ) by first and second shear layer modes ( $n=1$  &  $2$ ) are shown in figure 4-10 as function of the mean flow velocity. Again each data point in this plot is the frequency of the corresponding amplitude data point presented in figure 4-9 at the same flow velocity. As a result of rounding the cavity edges, the resonance frequencies show slight decrease by 0.9% from the base case B1 (1, 1).

Figure 4-11 shows the dimensionless pressure amplitude versus the reduced velocity for the rounded edges cavity of one inch long ( $L/d=1$ ). This figure shows that the diametral modes excited by the second shear layer mode ( $n=2$ ) have a reduced velocity ranged from 1.1 to 1.7 and a maximum dimensionless amplitude

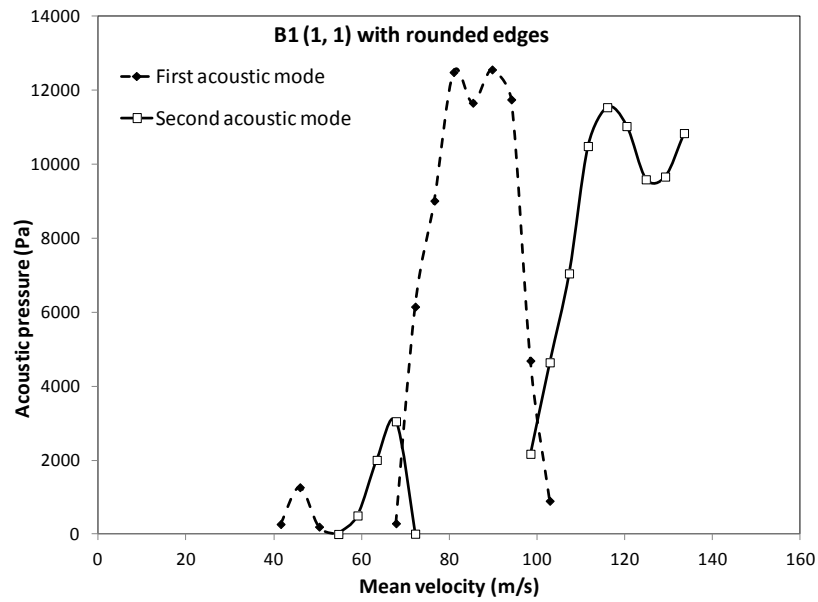


Figure 4-9 Pressure amplitudes of excited acoustic modes at different flow velocities,  $d=25\text{mm}$ ,  $L/d=1$ ,  $d/D=2/12$ ,  $r/L=0.2$

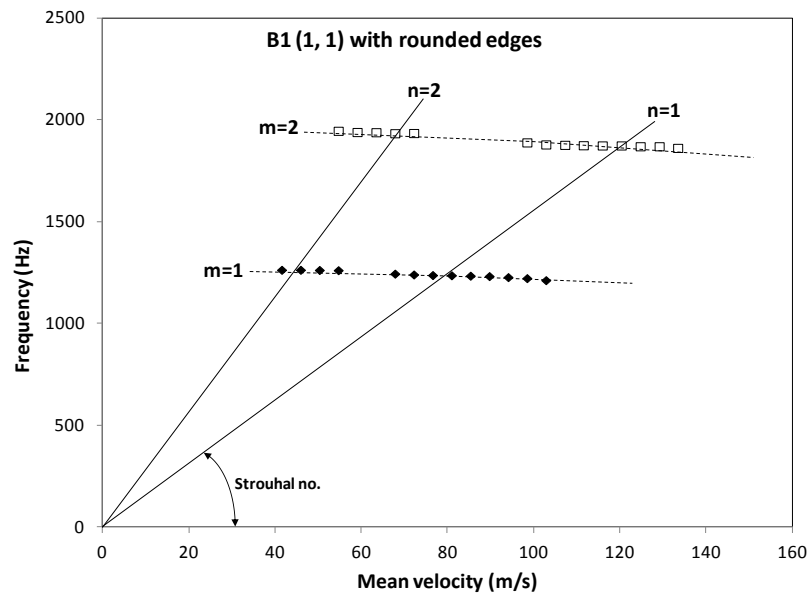


Figure 4-10 Frequency of excited acoustic modes at different flow velocities,  $d=25\text{mm}$ ,  $L/d=1$ ,  $d/D=2/12$ ,  $r/L=0.2$

of 1.1 at a reduced velocity of 1.4. While the first shear layer mode ( $n=1$ ) has a reduced velocity range from 2 to 3 and a maximum dimensionless amplitude of 3.2 at a reduced velocity of 2.6. It should be mentioned here that as a result of rounding the cavity edges, the values of the reduced velocity ranges corresponding to the shear layer modes are higher than those of the base case B1 (1, 1). This is because the radius of curvature ( $r$ ) was not taken into account when calculating the characteristic length in the reduced velocity formula, such effect is examined below.

Figure 4-12 compares the amplitude of the acoustic pressure for the rounded case and the base case B1 (1, 1) as a function of velocity. The figure shows that the main differences between the two cases is that the pressure amplitudes increased by more than a factor of two when rounded case is compared with the base case B1 (1, 1). This result is similar to that reported by Bruggeman et al. (1991) for rounding the upstream and the downstream edges of a deep side branch. Also, Nakiboğlu et al. (2012) reported similar results for longitudinal modes of a pipeline housing a shallow cavity. They explained that this increase in pressure amplitudes is due to the rounding of upstream cavity edge and can be qualitatively predicted by vortex sound theory. This comparison shows that the rounding of the cavity edges results in increasing the amplitudes of the fluid resonant oscillations. This is independent of the acoustic wavelength to the cavity length. Also, this effect is opposite to what is observed in fluid dynamic oscillations (Pereira & Sousa, 1994). In the case of fluid dynamic oscillations, rounded cavity edges reduce the level of oscillation.

Figure 4-13 shows the dimensionless acoustic pressure ( $P/\frac{1}{2}\rho V^2$ ) plotted against the reduced velocity based on cavity length ( $V_r = V/fL$ ). Continuous and dotted lines are drawn to form envelopes of the data points of shear layer modes for the base and rounded cavity cases respectively. The purpose of the envelopes is to visually illustrate the trend observed in the plotted data. The figure shows that the maximum value for the second shear layer mode has increased by more than a factor of 2 when the cavity edges were rounded. Similarly, for the first shear layer mode, the maximum value has increased by a factor of 2. Moreover these maximum values for either shear layer modes are shifted to higher reduced

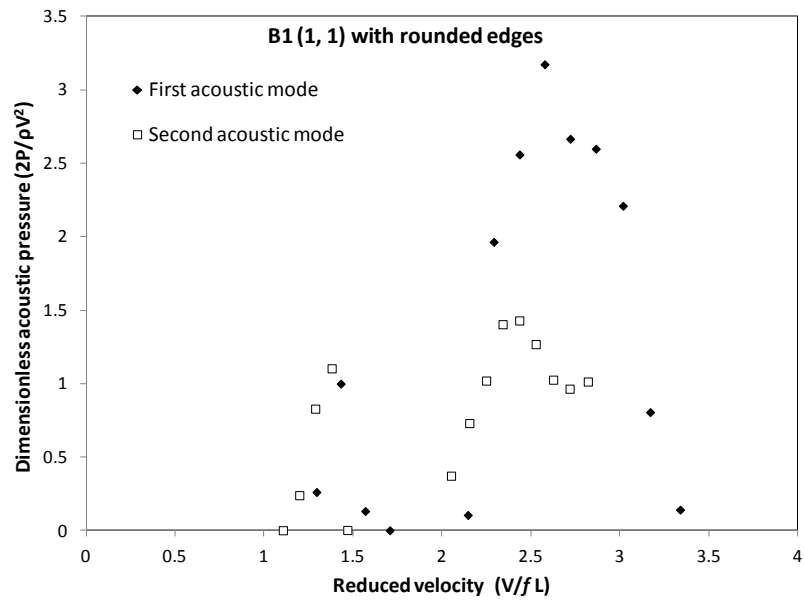


Figure 4-11 Dimensionless acoustic pressures ( $P/\frac{1}{2}\rho V^2$ ) versus reduced velocity ( $V_r = V/fL$ ),  $d=25\text{mm}$ ,  $L/d=1$ ,  $d/D=2/12$ ,  $r/L=0.2$

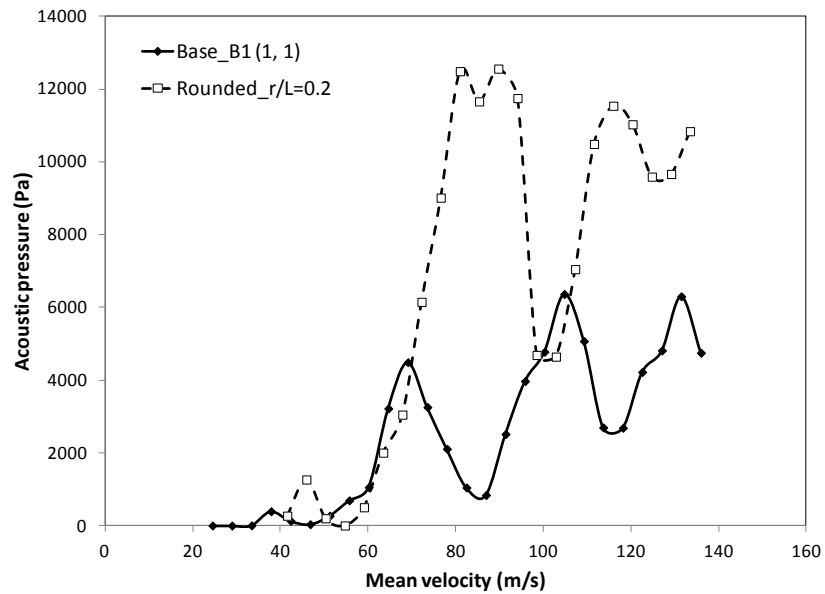


Figure 4-12 Influence of rounding cavity edges on pressure amplitudes of excited acoustic modes at different flow velocities,  $d=25\text{mm}$ ,  $L/d=1$ ,  $d/D=2/12$ ; \_\_\_ base, ---- rounding

velocities. For the second shear layer mode, the maximum value for the base case occurs at a reduced velocity of 1.2 while the rounded case at a reduced velocity of 1.4. The shift of data points as well as increase in dimensionless amplitude between the base and the rounded cases is similar to what Nakiboğlu et al. (2010) found when studying the effect of edge geometry on both corrugated pipes and multiple sidebranch system. Nakiboğlu et al. (2010) reported the dimensionless pressure fluctuation amplitude for the acoustic mode as a function of Strouhal number for a round upstream–sharp downstream case and sharp upstream–round downstream case with  $r/L = 0.1$ . Bruggeman et al. (1991) concluded that the characteristic length used in the Strouhal number definition should be the sum of the cavity width and the upstream edge radius,  $L+r_{up}$ . This is because the traveled distance by the vorticity perturbation is increased by rounding off the upstream edge. The use of the modified gap length ( $L_e = L + r_{up}$ ) as the characteristic length for the reduced velocity decreases the discrepancy in the values of reduced velocity observed in figure 4-13.

Figure 4-14 shows the dimensionless amplitude as a function of the reduced velocity based on the modified gap length ( $L_e$ ). The figure shows that the tips of the continuous and dashed envelopes of the base and rounding cases coincide with each other. This provides a better understanding of the effect of rounding the edges. Figure 4-14 present a difficulty when comparing the data of different cases because there are lots of data points that do not show which acoustic mode is excited first, and which mode is dominating at what velocity. To avoid such confusion during analysis and comparison of the other suppression devices, the acoustic pressure amplitudes against flow velocity will be used throughout the study. The dimensionless plot of acoustic pressure and reduced velocity will be addressed when required.

For the two inch cavity length, two rounding radii are tested. The ratios ( $r/L$ ) for the two cases are 0.1 and 0.2. The ratio  $r/L=0.2$  ( $r = 0.4\text{in} = 10\text{mm}$ ) showed a similar behavior as discussed for the one inch long cavity. For the ratio  $r/L = 0.1$  ( $r = 0.2\text{in} = 5\text{mm}$ ), the acoustic pressure amplitudes were increased by factor of 2.25. The results showing this case can be found in figures A-1 to A-10

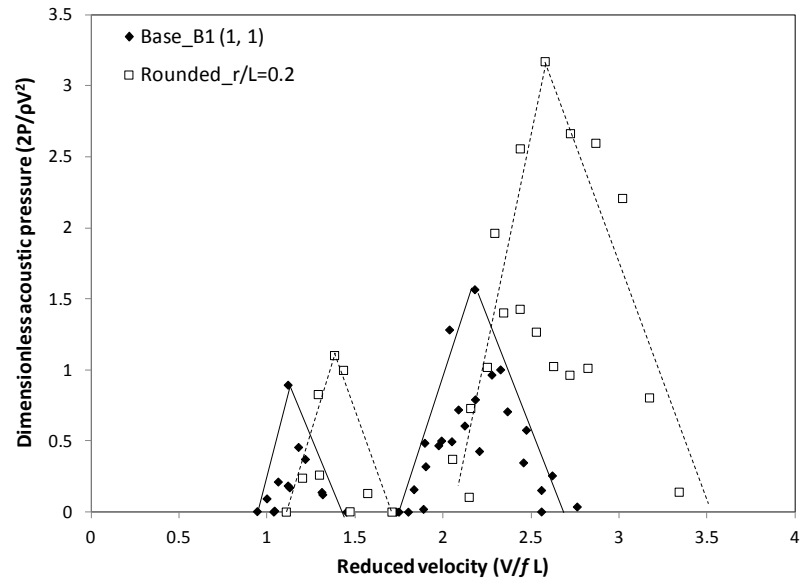


Figure 4-13 Influence of rounding cavity edges on dimensionless pressure ( $P/\frac{1}{2}\rho V^2$ ) amplitudes of excited acoustic modes against reduced velocity ( $V_r = V/fL$ ),  $d=25\text{mm}$ ,  $L/d=1$ ,  $d/D=2/12$ ; \_\_\_ base, ---- rounding

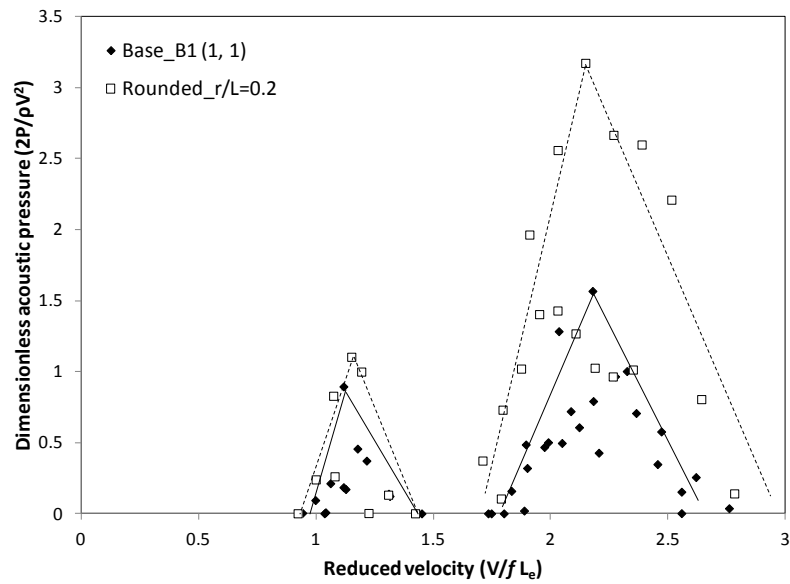


Figure 4-14 Influence of rounding cavity edges on dimensionless pressure ( $P/\frac{1}{2}\rho V^2$ ) amplitudes of excited acoustic modes against reduced velocity ( $V_r = V/fL_e$ ),  $L_e = L + r$ ,  $d=25\text{mm}$ ,  $L/d=1$ ,  $d/D=2/12$ , \_\_\_ base, ---- rounding

of the Appendix A. These results indicate that even small rounding of  $r/L = 0.1$  results in significant increase of the pressure amplitude.

To summarize this section, rounding off the up- and downstream cavity edges has augmented the acoustic modes excitation. This agrees with the findings in the literature. For the one and two inch cavity lengths, rounding off the cavity edges ( $r/L = 0.2$ ) has increased the amplitudes of acoustic pressure by a factor of 2. Even when the radius of curvature is made smaller for the two inch cavity length ( $r/L = 0.1$ ), this results in even higher pressure amplitudes. In addition, using  $L_e$  ( $L_e = L+r_{up}$ ) as the characteristic length eliminated the apparent delay in reduced velocity ranges. Concluding from these results, rounding the edges delayed the onset of acoustic resonances due to the increase in the effective cavity length. It also increased the maximum amplitude of pulsation during the Lock-in resonance range. In the next section, chamfering the cavity upstream corner is tested.

### **4.1.3 Chamfering Upstream Cavity edge**

This section discusses the effect of chamfering the cavity leading edge on the fluid resonant oscillations. Chamfers (also known as ramp or bevel) at the upstream and the downstream cavity edges were used to suppress the acoustic resonance with some degree of success by Smith & Loluff (2000) in gate valves. Franke & Carr (1975) as well as Heller & Bliss (1975) used the chamfer to suppress self sustained oscillations for different cavity aspect ratios. The idea of using a chamfer with same ratio of chamfer length to cavity length ( $l/L$ ) as that used by Smith & Loluff (2000) was repeated by Janzen et al., (2007). However, Janzen et al., (2007) used the chamfer only at the upstream edge of the cavity of gate valve. Their results showed some success as a noise-reduction method. Knotts & Selamet (2003) also conducted experiments studying the effect of different sizes of chamfer upstream of a deep side branch as well as at its up and downstream edges. They found that using the upstream chamfer only showed similar results to those of the combined upstream and downstream chamfer, and suggested that the upstream-only chamfer is capable of suppressing high acoustic

pressure amplitudes. Therefore, the effectiveness of upstream chamfers for the present configuration is investigated in this section.

Based on the literature, a chamfer seat is inserted upstream the cavity. For the one inch cavity length, the ratio of chamfer length to cavity length ( $\ell/L$ ) of 0.2 is used where  $\ell = 0.192\text{in} = 4.88\text{mm}$ . The chamfer angle of  $17^\circ$  is used. The amplitudes of acoustic pressure as a function of the flow velocity is plotted in figure 4-15. Figure 4-15 also shows the same data for the base case B1 (1, 1). The purpose of the comparison is to illustrate in part the effect of chamfer on the acoustic resonance. The figure shows that the chamfer was capable of delaying the resonance up to 73 m/s. Yet, it did not reduce the overall acoustic pressure effectively. Only 17.5% reduction is achieved in comparison with base case B1 (1, 1). Moreover, the cavity with chamfer seat follows the same trend as the base case over the same range of flow velocity with shift in the flow velocity as a result of increasing cavity length.

Similar experiments were conducted for the two inch long cavity with the same chamfer length to cavity length ratio ( $\ell/L$ ). The chamfer tested in this case has a length of  $\ell = 0.384\text{in} = 9.75\text{mm}$  and an angle of  $17^\circ$ . Figure 4-16 presents a comparison of the amplitudes of acoustic pressure for the chamfer seat to the base case B2 (1, 2). The comparison shows that this chamfer is capable of delaying the resonance up to a flow velocity of 117 m/s. In addition, the maximum value of acoustic pressure in case of the chamfer seat reached half the maximum value of base case B2 (1, 2) and this is considered a success of this chamfer in suppressing and delaying resonance.

The long chamfer ( $\ell = 0.384\text{in} = 9.75\text{mm}$ ) is tested with one inch cavity length. For this arrangement the chamfer length to cavity length ratio ( $\ell/L$ ) is 0.4. The test results of this arrangement are plotted in figure 4-17(a). The results show that the long chamfer performed better than the short chamfer ( $\ell = 0.192\text{in} = 4.88\text{mm}$ ) in suppressing as well as delaying resonance of the one inch cavity. The long chamfer delayed the resonance up to a flow velocity of 93 m/s which is higher than the delay reached by the short chamfers. In addition, the maximum acoustic pressure reached in case of long chamfer seat was reduced by 66%

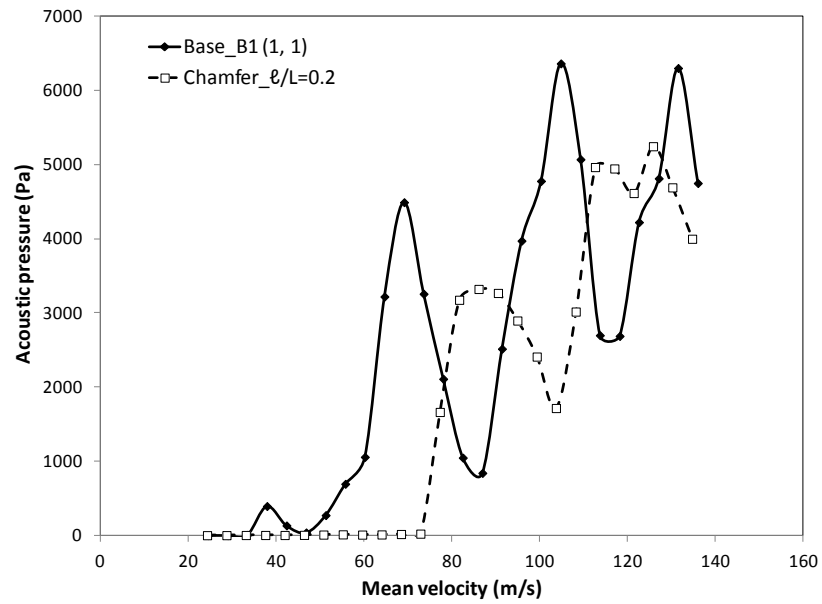


Figure 4-15 Influence of upstream chamfer on pressure amplitudes of excited acoustic modes at different flow velocities,  $d=25\text{mm}$ ,  $L/d=1$ ,  $d/D=2/12$ , \_\_\_ base, - - - chamfer

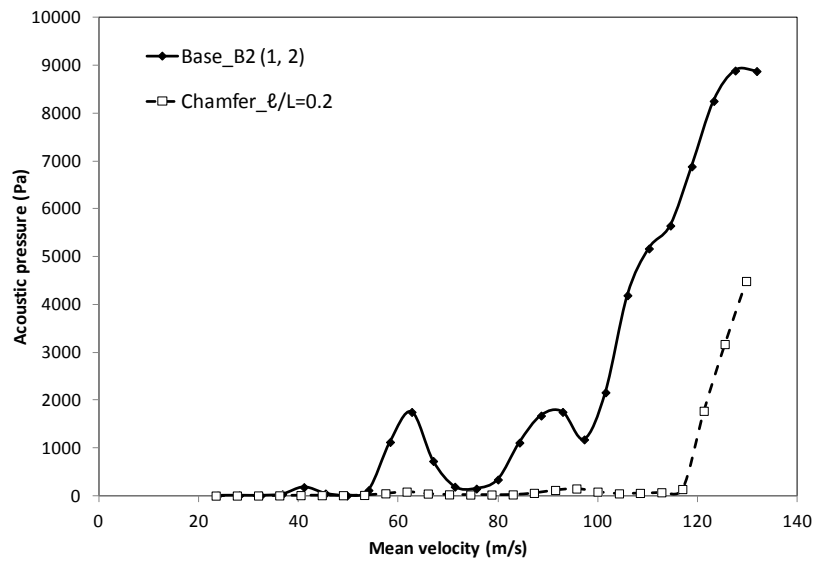


Figure 4-16 Influence of upstream chamfer on pressure amplitudes of excited acoustic modes at different flow velocities,  $d=25\text{mm}$ ,  $L/d=2$ ,  $d/D=2/12$ , \_\_\_ base, - - - chamfer

compared to the base case B1 (1, 1), which is again higher suppression than the short chamfer.

Figure 4-17(b) shows the difference in the suppression level of the two chamfer arrangements by comparing the dimensionless acoustic pressure amplitudes as a function of the reduced velocity of the two arrangements to the base case B1 (1, 1). The reduced velocity is calculated based on the effective cavity gap length. For the chamfer, the effective cavity gap length is the summation of cavity length and chamfer length ( $L_e=L+\ell$ ). The figure shows that the maximum dimensionless pressure for the first shear layer mode ( $n=1$ ) reached by the short chamfer is 0.79. This is a reduction of 50% in comparison to the base case that has a maximum of 1.6. For the long chamfer, the first shear layer mode is shifted to a reduced velocity of 1.6. In addition, the maximum dimensionless amplitude of the first shear layer mode ( $n=1$ ) reached by the long chamfer is 0.32. This represents a reduction of 80% from the base case values. Both the short and the long chamfers are successful in suppressing acoustic modes excited by the second shear layer mode.

Testing the short chamfer for two inch cavity length was not that intriguing, yet it is required to confirm the observed trends. Figure 4-18(a) shows the effect of short chamfer ( $\ell/L=0.1$ ) for the two inch cavity on acoustic pressure amplitudes versus flow velocity. The expectations regarding the delay of resonance or the reduction in acoustic pressure for the short chamfer in two inch cavity were correct. Compared with the base case B2 (1, 2), the short chamfer delayed the resonance slightly; up to a flow velocity of 63 m/s and produced almost no reduction in amplitudes of acoustic pressure.

Figure 4-18(b) shows detailed comparison of the dimensionless acoustic pressure amplitudes and the reduced velocity based on effective cavity length for two inch cavity length, between the long and short chamfer with the base case B2 (1, 2). The figure shows that the maximum dimensionless pressure for the first shear layer mode ( $n=1$ ) reached by the short chamfer is 0.85 at a reduced velocity of 2.0. For the long chamfer, the maximum dimensionless pressure is 0.2 at a

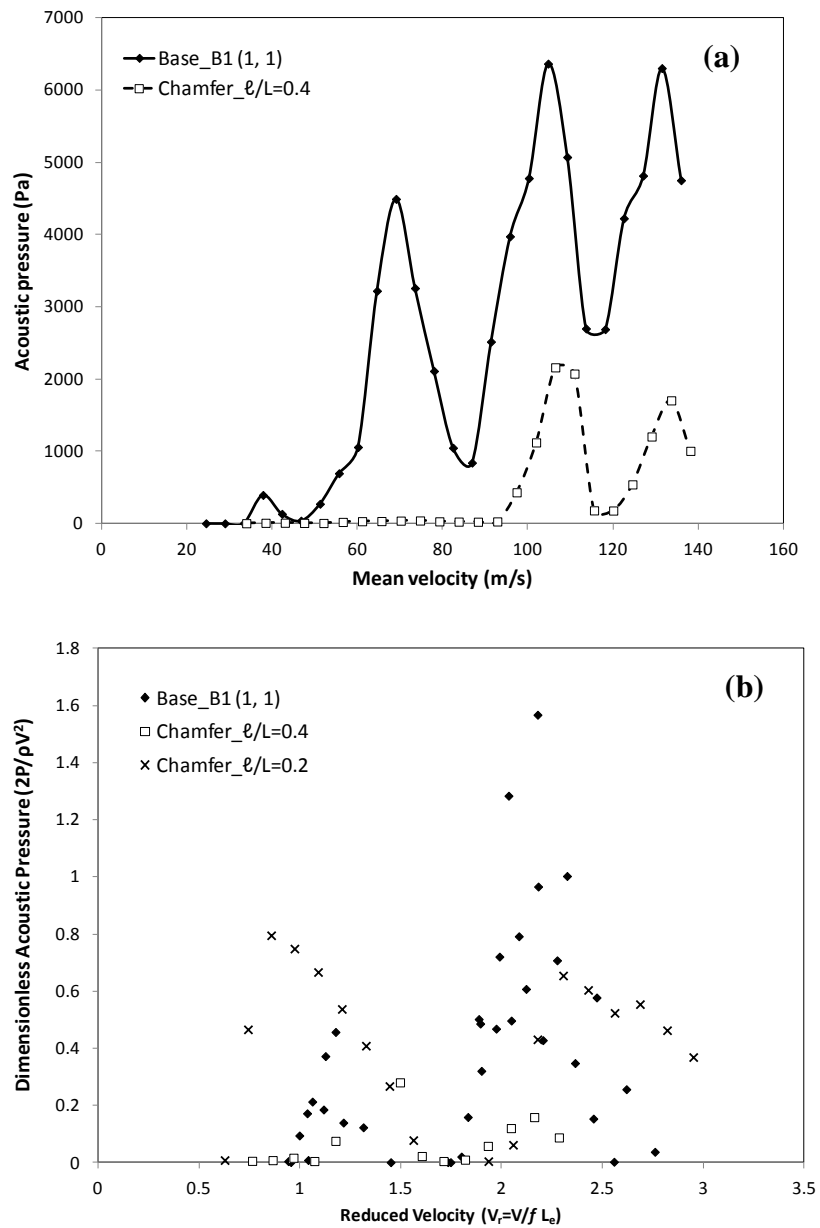


Figure 4-17(a) Influence of long chamfer on pressure amplitudes of excited acoustic modes at different flow velocities,  $d=25\text{mm}$ ,  $L/d=1$ ,  $d/D=2/12$ , \_\_\_base, - - - chamfer (b) Influence of long and short chamfer on dimensionless pressure ( $P/\frac{1}{2}\rho V^2$ ) amplitudes of excited acoustic modes against reduced velocity ( $V_r=V/fL_0$ ),  $L_e=L+r$ ,  $d=25\text{mm}$ ,  $L/d=1$ ,  $d/D=2/12$ , ■ Base case, X short chamfer, □ Long chamfer

reduced velocity of 1.8. This is in comparison to the base case that has a maximum of 1.6 at a reduced velocity of 2.2. For the long chamfer it is important to note that due to the limited capacity of the blower, it is not possible to test the whole range of reduced velocity of the first shear layer mode as shown in figure 4-18(b). As a result, the reported maximum value of the pressure amplitude is only the achievable value and a higher value is possible at higher reduced velocity. In addition, the maximum dimensionless amplitude of the second shear layer mode ( $n=2$ ) reached by the short chamfer is 0.4. This is 46% of the base case maximum value of 0.74. On the other hand, the long chamfer is successful in suppressing acoustic modes excited by the second shear layer mode. Moreover, both chamfers were capable of completely suppressing the third shear layer mode ( $n=3$ ).

This section presented the effect of introducing a chamfer upstream the cavity as a method of cavity noise reduction. The section also discussed the impact of changing the chamfer length on the level of reduction. The analyses showed that chamfering the leading edge can result in reducing and delaying the onset of fluid-resonant oscillations. The level of reduction is strongly dependent on the ratio of the chamfer length to cavity length ( $\ell/L$ ). This reduction in fluid resonant oscillations is the result of the change in hydrodynamic characteristics of the upcoming boundary layer. This change affects the instability characteristics of the cavity free shear layer as well as the interaction between the shear layer and the acoustic particle velocity. For one inch cavity length, the chamfer with ( $\ell/L=0.2$ ) did affect the acoustic resonance amplitude. However, the chamfer with ( $\ell/L=0.4$ ) was effective in producing weaker resonance. While for two inch cavity length, the chamfer with ( $\ell/L=0.2$ ) provided sufficient disturbance to the coupling of the shear layer mode and the acoustic field over the tested velocity range. These results agree with what is reported in the literature which is that coherent vortex shedding instabilities over a cavity can be significantly reduced by altering the flow at the upstream edge of the cavity. The chamfer with ( $\ell/L=0.4$ ) achieved a reduction in the pressure amplitude of 75%. On the other hand, the chamfer with ( $\ell/L=0.1$ ) did not reduce the acoustic amplitude.

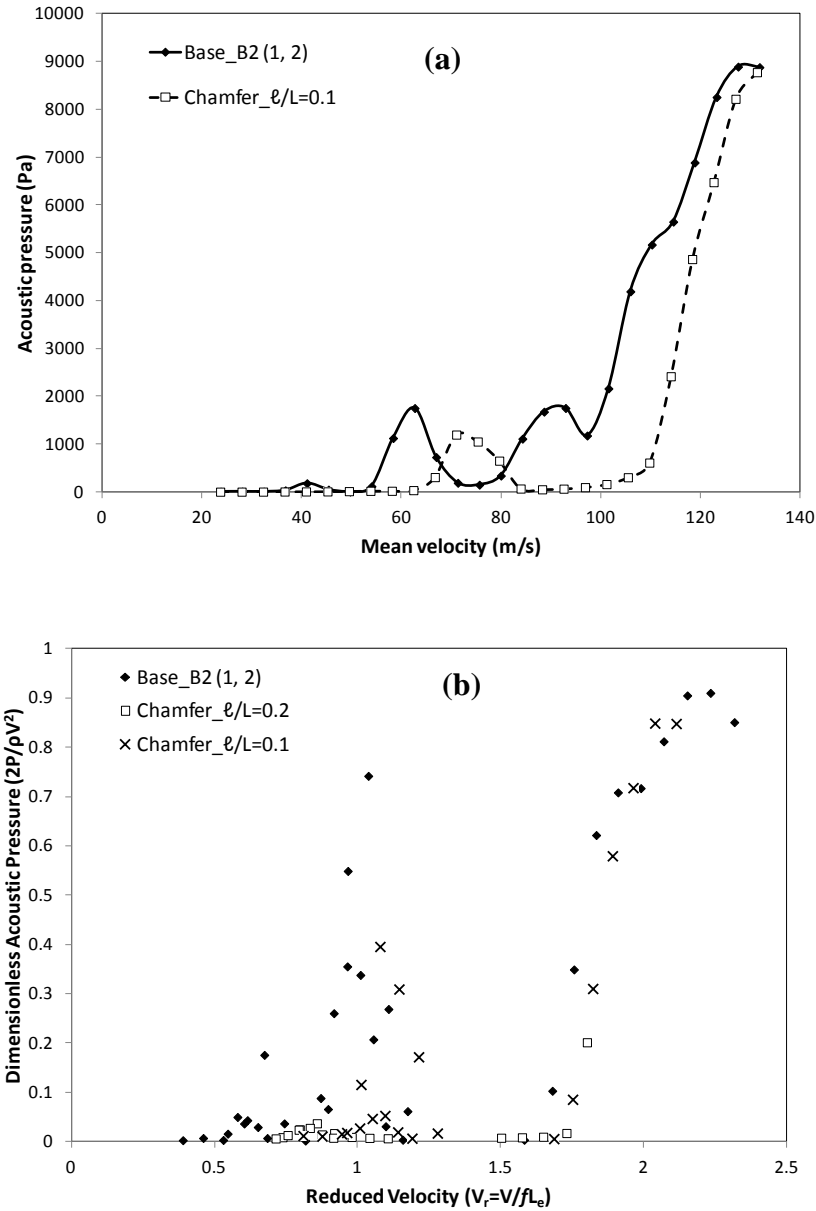


Figure 4-18(a) Influence of short chamfer on pressure amplitudes of excited acoustic modes at different flow velocities,  $d=25\text{mm}$ ,  $L/d=2$ ,  $d/D=2/12$ , \_\_\_base, - - - chamfer, (b) Influence of long and short chamfer on dimensionless pressure ( $P/\frac{1}{2}\rho V^2$ ) amplitudes of excited acoustic modes against reduced velocity ( $V_r=V/fL_e$ ),  $L_e=L+r$ ,  $d=25\text{mm}$ ,  $L/d=2$ ,  $d/D=2/12$ , ■ Base case, X short chamfer, □ long chamfer

The next section discusses two different spoiler geometries installed at the cavity leading edge.

#### **4.1.4 Leading Edge Spoilers**

Another tested passive control method is introducing leading edge spoiler. Spoilers were among the first types of flow control in fluid dynamic oscillation to be studied in conjunction with cavities. Rossiter (1964) tested various leading edge spoilers and found that almost any type of leading edge spoiler can reduce the intensity of the pressure fluctuations inside a cavity at subsonic speeds. Spoilers were also examined and tested numerous in weapon bay cavities (Shaw (1979), Shaw et al., (1988), Dix & Bauer (2000), Schmit & Raman (2006 ) and others). However, in fluid resonant cavities there are fewer studies that used spoilers. Fluid resonance in deep side branches have been the examined configuration in the literature (Bruggeman et al. (1991), Knotts & Selmat (2003)). Spoilers are less popular in fluid resonant cavities because of the pressure drop they cause. So designing a spoiler is challenging to meet the desired attenuation with minimum pressure drop.

The first spoiler; spoiler (1) has the configuration of 60 teeth; 4.88mm chamfer length, 3.5 mm tooth height from the base, 2° tooth width, and 4° spacing between the teeth. Spoiler (1) is tested upstream of the one inch and the two inch long cavities. The acoustic pressure amplitudes for those two cases are plotted in figures 4-19 and 4-20, respectively.

Scrutinizing figure 4-19, it shows three resonance zones were excited in case of spoiler (1). Two of which are strong where their maximum peaks occur at 97 m/s and 128 m/s. But the third resonance zone is the weakest of the three zones and the maximum value occurs at 71 m/s. In the base case B1 (1, 1), four resonance zones exist along the velocity range. Three of which are strong and of maximum pressure amplitudes at 69 m/s, 104m/s, and 127 m/s. And the fourth occurs at the beginning of velocity range and is the weakest zone excited. The figure also shows that spoiler (1) was able to delay resonance up to almost 90 m/s flow velocity. Also the comparison with the base case shows that the spoiler

decreased the excited acoustic zones. Moreover, spoiler (1) suppressed the maximum pressure amplitude by 21%. In addition, spoiler (1) increases the loss coefficient of the system. This is manifested in decreasing the maximum flow velocity that is achieved in comparison to the base case B1 (1, 1). This result agrees with the literature that leading edge spoilers attempt to reduce cavity noise and fluctuating pressure levels by lifting the shear layer and reducing its interaction with the cavity trailing edge. A comparison is needed in order to differentiate the effect of spoiler teeth alone away from the effect of chamfer. This is done by comparing figure 4-15 and figure 4-19. The comparison shows that spoiler (1) delayed resonance up to 90 m/s while the chamfer delayed resonance up to 73m/s. In addition, the data points in case of spoiler (1) show similar trend to the base case unlike the chamfer alone.

The effect of spoiler (1) on the acoustic pressure amplitude for the two inch cavity length is shown in figure 4-20. The figure shows that the spoiler succeeded in completely suppressing resonance up to 100 m/s. The resonance excitation occurs at the end of the velocity range with 6% higher peak in comparison with the base case. However, the spoiler increased the loss coefficient of the system. As previously mentioned, this is clearly manifested in the decrease in the maximum flow velocity that is achieved in comparison to the base case B2 (1, 2). The difference between the effectiveness of the chamfer and the spoiler is concluded by comparing 4-18(a) and figure 4-20. The comparison shows that the spoiler delayed resonance to higher velocity than the chamfer alone. However, the spoiler enhanced the resonance at the higher flow velocities. In addition, the spoiler increased the loss coefficient of the system than the chamfer alone.

The second spoiler; spoiler (2), has the configuration of 30 teeth; 9.75mm chamfer length, 7 mm tooth height from the base, 4° tooth width, and 8° spacing between the teeth. Spoiler (2) is tested upstream of the one inch and the two inch long cavities and the results are plotted in figures 4-21 and 4-22, respectively.

Figure 4-21 presents the effect of spoiler (2) on the one inch cavity length. The figure shows only one resonance zone exists in the case of spoiler (2). This is in contrast with the base case that excites four resonance zones. The spoiler suppressed the acoustic resonance by 94%. The maximum pressure peak occurs at

112 m/s. The difference between the effectiveness of the chamfer and the spoiler is concluded by comparing figure 4-21 and figure 4-17(a). The comparison shows that a higher delay of lock-in is achieved with spoiler than that achieved with the chamfer. Also, the spoiler exceeded the long chamfer in eliminating and suppressing acoustic modes and their peaks. On the other hand, the spoiler increased the loss coefficient of the system. This is clearly shown by the decrease in the maximum flow velocity that is achieved when the spoiler is installed in comparison to the base case and the chamfer.

The results of testing spoiler (2) for the two inch cavity length is shown in figure 4-22. The figure shows only one resonance zone is exist in case of spoiler (2). This excited acoustic resonance exists at the end of the velocity range. And the base case excites four resonance zones. The spoiler suppressed of acoustic resonance by 75% and the maximum peak occurs at 123 m/s. A comparison is needed in order to differentiate the effectiveness of spoiler and the chamfer. This is done by comparing 4-22 and figure 4-16. The comparison shows that a similar delay of lock-in is achieved in both cases. But the spoiler exceeded the chamfer in reaching lower pressure peak of the acoustic modes. On the other hand, the spoiler increased the loss coefficient of the system. This is clearly shown by the decrease in the maximum flow velocity that is achieved in comparison to the base case and the chamfer.

This section presented the introducing of a spoiler as a suppression device upstream the cavity. Leading edge spoiler provides 3-D disturbances to shear layer perturbation at the separation edge. The shear layer instabilities increases and break up into 3D turbulence. As a result of the break the coupling of the shear layer perturbations and the acoustic particle velocity at the leading edge is disturbed. Therefore weaker resonance is produced. These results agree with the observations of Lawson & Barakos (2011). They compared the experimental and computational results of different leading and trailing edge control devices. Lawson & Barakos (2011) have shown that leading edge devices, including sawtoothed spoilers, altered the feedback mechanism. The alteration is achieved by deflecting the shear layer and shifting the flow at the cavity leading edge.

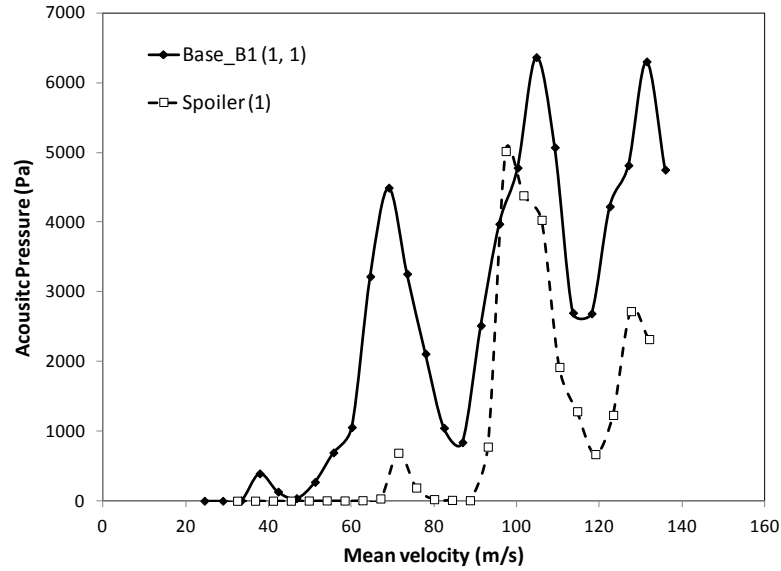


Figure 4-19 Influence of spoiler (1) on pressure amplitudes of excited acoustic modes at different flow velocities,  $d=25\text{mm}$ ,  $L/d=1$ ,  $d/D=2/12$ , \_\_\_ base, - - - spoiler

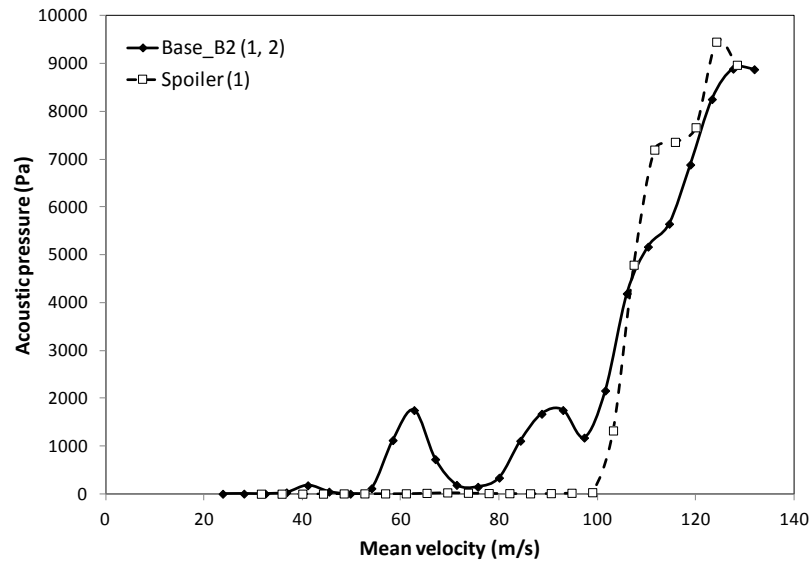


Figure 4-20 Influence of spoiler (1) on pressure amplitudes of excited acoustic modes at different flow velocities,  $d=25\text{mm}$ ,  $L/d=2$ ,  $d/D=2/12$ , \_\_\_ base, - - - spoiler

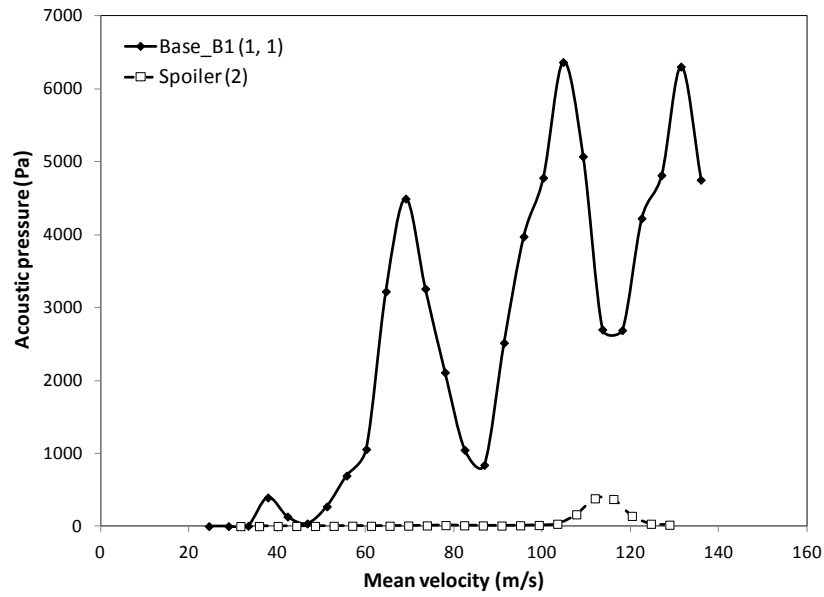


Figure 4-21 Influence of spoiler (2) on pressure amplitudes of excited acoustic modes at different flow velocities,  $d=25\text{mm}$ ,  $L/d=1$ ,  $d/D=2/12$ , \_\_\_ base, - - - spoiler

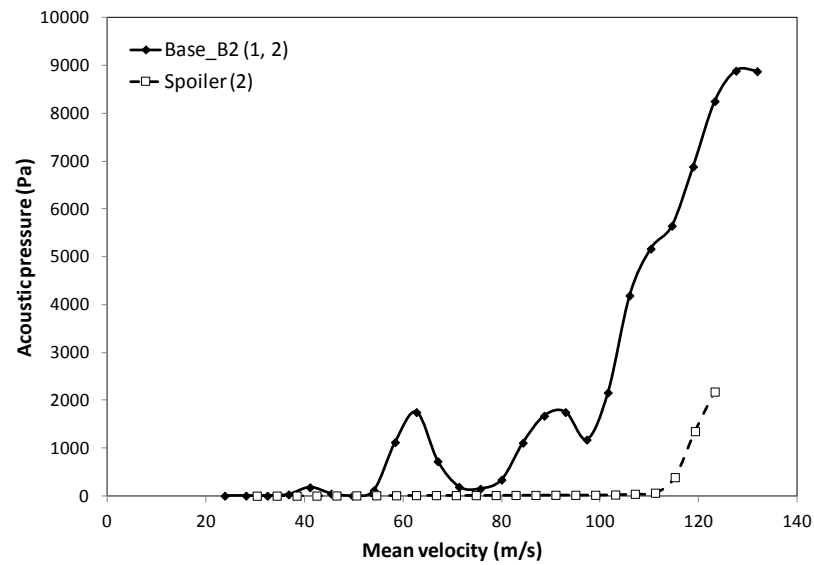


Figure 4-22 Influence of spoiler (2) on pressure amplitudes of excited acoustic modes at different flow velocities,  $d=25\text{mm}$ ,  $L/d=2$ ,  $d/D=2/12$ , \_\_\_ base, - - - spoiler

### **4.1.5 Summary of one inch Cavity depth ( $d=25\text{mm}$ )**

- This section examined the base cases for one inch and two inch cavity lengths in details, showing the acoustic response, pressure amplitudes and the frequency of excited acoustic modes.
- Rounding upstream and downstream edges were designed and tested for two different radii. These rounded seats failed to suppress any mode.
- Two chamfers were tested upstream of the cavity for one inch and two inch cavity lengths. The short chamfer failed in suppressing or delaying the acoustic resonances to a higher flow velocity. The long chamfer succeeded in delaying the resonances to considerably higher flow velocity. In addition, the long chamfer reduced pressure amplitude by a factor of 0.3 and 0.5 for one inch and two inch cavity lengths, respectively.
- Finally, two spoiler designs were tested upstream the cavity for the one inch and the two inch cavity lengths. The proper combination of chamfer length and spoiler teeth size can achieve a delay of lock-in to higher flow velocities, or the combination can lead to almost complete suppression of acoustic modes. In either case, this can be done at the cost of increasing loss coefficient of the system.

It was previously mentioned that the acoustic pressure decays faster as the cavity gets deeper; recall figure 3-9. So the effect of different passive suppression devices for larger cavities will be explored. These larger cavities generate more robust acoustic resonance. The next sections will present the results of changing the size of the cavity into shallow cavity (half inch deep) and deep cavity (two inch deep).

## **4.2 Results of Half inch cavity depth ( $d=12.5\text{mm}$ )**

This section presents the results of the tests performed on the half inch deep cavity. Two cavity lengths are considered the one inch long ( $L/d=2$ ) and the two inch long ( $L/d=4$ ). This section follows the same presentation approached used in the previous section. First section 4.2.1 discusses the results of the base cases B3 (1/2, 1) and B4 (1/2, 2) for one inch and two inch cavity lengths, respectively.

This is followed in section 4.2.2 by the discussion of the results of suppression seats. The discussion illustrates the characteristics of the excitation of different acoustic modes by various cavity shear layer modes. The amplitude of acoustic pressure and frequency of these modes with mean flow velocity is also presented.

#### 4.2.1 Base Cases B3 (1/2, 1) and B4 (1/2, 2)

This section illustrates in detail the main characteristics of the excitation mechanism of the diametral modes for the base cases B3 (1/2, 1) and B4 (1/2, 2). Those two cases are the one inch and the two inch cavity lengths, respectively.

The amplitude and frequency of the dominant peaks in the pressure spectra for base case B3 (1/2, 1) are presented in figures 4-23 and 4-24, respectively. Figure 4-23 shows the pressure amplitudes of the excited acoustic modes ( $m=1-4$ ) by shear layer modes ( $n=1$  &  $2$ ) versus flow velocity. The pressure amplitude ranged from approximately 0.32 Pa to 1743 Pa for the velocity ranges of 28 to 138 m/s. This velocity range corresponds to Mach number of approximately 0.082 to 0.4. The resonance frequencies of the excited acoustic modes ( $m=1-4$ ) by first and second shear layer modes ( $n=1$  &  $2$ ) as a function of mean flow velocity for base case B3 (1/2, 1) are shown in figure 4-24. Each data point in this plot is the frequency of the corresponding amplitude data point presented in the previous plot at the same flow velocity. The plot shows that the resonance frequencies of the excited acoustic modes ( $m=1-4$ ) decrease slightly along the flow velocity. This is quite noticeable by the dotted lines drawn. The shear layer modes exciting the acoustic modes have specific range of Strouhal number ( $St=f L/V$ ). The Strouhal number is represented by the slope of the straight and continuous lines indicated in the figure. These continuous lines pass around the peak pressure amplitudes of the excited acoustic resonance. At the beginning of the velocity range, the first diametral mode ( $m=1$ ) is excited by first shear layer mode ( $n=1$ ) over the velocity range of 28-76 m/s. The maximum pressure amplitude over this velocity range is 190 Pa. As the velocity increases, the third diametral mode ( $m=3$ ) is excited over the velocity range of 75-90 m/s. This is followed by the excitation of the fourth acoustic mode ( $m=4$ ) over the velocity range of 90-102

m/s. The excited third and fourth acoustic modes reached maximum acoustic pressure of 284 and 343 Pa, respectively. Those two acoustic modes are excited by the second shear layer mode ( $n=2$ ) as shown in figure 4-24. At higher velocities, the first shear layer mode ( $n=1$ ) excites both the second and third acoustic modes. The second diametral mode ( $m=2$ ) is excited over the velocity range of 98-134 m/s. Finally the third diametral mode is excited a flow velocity of 123 m/s. The second and third diametral modes reached maximum amplitude of 1743 Pa and 1358 Pa, respectively.

Figures 4-25 and 4-26 show the results of the base case B4 (1/2, 2). They present the amplitudes of the acoustic pressure and resonance frequencies, respectively, for the excited acoustic modes as function of flow velocity. Again the behavior in this case is very similar to B3 (1/2, 1) discussed previously. It should be pointed out that increasing the cavity length resulted in higher pressure amplitudes compared to B3 (1/2, 1). Also, the diametral frequencies dropped by 2% compared to B3 (1/2, 1). Yet, in both cases, the resonance frequencies decrease as the flow velocity increases. Moreover, the shear layer modes frequency decreases with the increase of cavity length. This results in only exciting acoustic modes ( $m=1-3$ ) for the base case B4 (1/2, 2) compared to acoustic modes ( $m=1-4$ ) for the case B3 (1/2, 1).

The changes in dimensionless acoustic pressure with reduced velocity are shown in figures 4-27 and 4-28 for the base cases B3 (1/2, 1) and B4 (1/2, 2), respectively. Figure 4-27 shows the dimensionless pressure ( $P/\frac{1}{2}\rho V^2$ ) plotted against the reduced velocity based on cavity length ( $V_r = V/fL$ ). The first shear layer mode ( $n=1$ ) has a reduced velocity ranged from 1.8-2.6 with maximum dimensionless pressure of 0.2. The maximum dimensionless pressure occurs at a reduced velocity of 2.3. The second shear layer mode ( $n=2$ ) reaches a maximum dimensionless pressure of 0.067 at a reduced velocity of 1.17. This corresponds to the excitation of the third and fourth acoustic modes over a reduced velocity ranged from 1-1.3. Figure 4-28 shows that for the case B4 (1/2, 2) the maximum dimensionless pressure reached by the third shear layer mode is 0.035 at a reduced velocity of 0.65. The third shear layer mode has a reduced velocity ranged from 0.6-0.7. The second shear layer mode reached maximum

dimensionless pressure of 0.25 at a reduced velocity of 1.07. The second shear layer mode has a reduced velocity ranged from 0.9-1.2. Finally the maximum dimensionless pressure reached by the first shear layer mode is 0.3 at a reduced velocity of 2.2. The first shear layer mode has a reduced velocity ranged from 1.8-2.2.

Generally the effect of decreasing the cavity depth on pressure amplitude in either dimensional or dimensionless form can be pointed out as follows: the maximum dimensionless pressure as well as maximum pressure amplitudes reached for the half inch deep cavities ( $d/D=1/12$ ) are lower than that reached by one inch deep cavities ( $d/D=2/12$ ). For example, the maximum dimensionless acoustic pressure reached by first diametral mode for the base case B3 (1/2, 1) (recall fig.4-27) is lower than that reached for the base case B1 (1, 1) (recall fig.4-7) by a factor of 4. Same observation stands for the base case B4 (1/2, 2) (recall fig.4-28) the first diametral mode excited by second shear layer mode reaches a maximum dimensionless pressure of 0.26 which is lower by a factor of 35 times than the base case B2 (1, 2) (recall fig.4-8).

Regarding the resonance frequencies, the half inch deep cavities are higher than those of one inch deep cavities. For example at flow velocity of 33 m/s, the resonance frequency for the base case B3 (1/2, 1) is 1314 HZ while the base case B1 (1, 1) is 1265 HZ. Also, the resonance frequency of the excited diametral modes decrease with increasing flow velocity for both half inch deep ( $d/D=1/12$ ) and one inch deep ( $d/D=2/12$ ) cavities. On the other hand, changing cavity depth did not affect the reduced velocity ranges of different shear layer modes. The reduction of velocity ranges are the same for both of half inch deep ( $d/D=1/12$ ) and one inch deep ( $d/D=2/12$ ) cavities.

The next section examines the results and analyses of introducing two different suppression devices upstream the cavity.

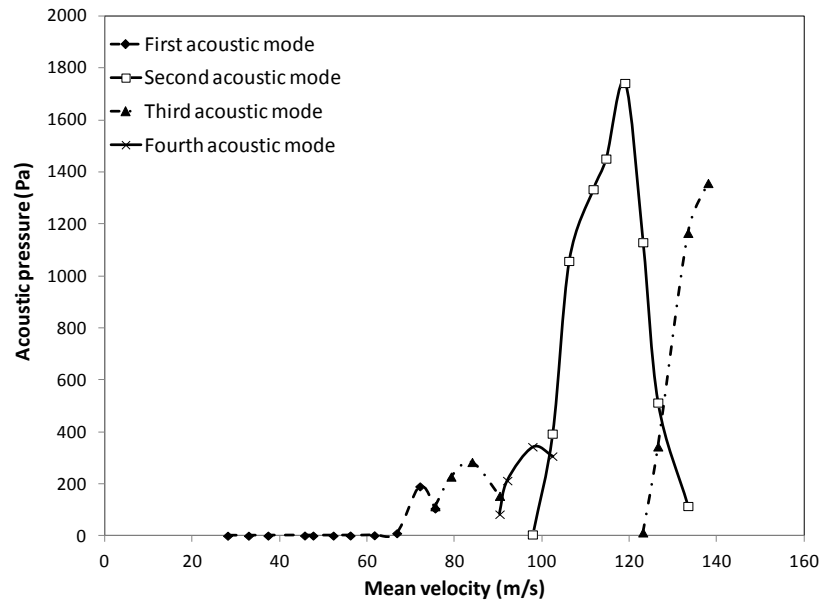


Figure 4-23 Pressure amplitudes of excited acoustic modes at different flow velocities for base case B3 (1/2, 1), d=12.5mm, L/d=2, d/D=1/12

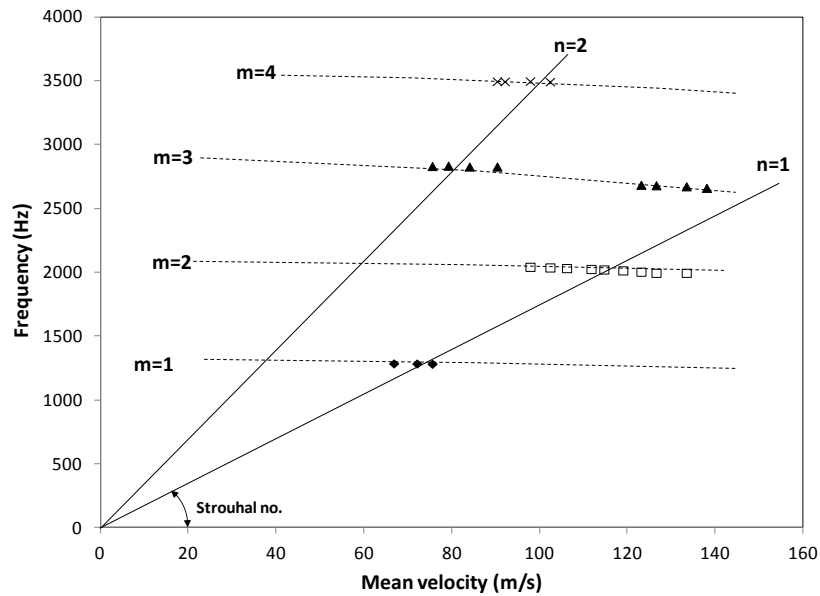


Figure 4-24 Frequency of excited acoustic modes at different flow velocities for base case B3 (1/2, 1), d=12.5mm, L/d=2, d/D=1/12

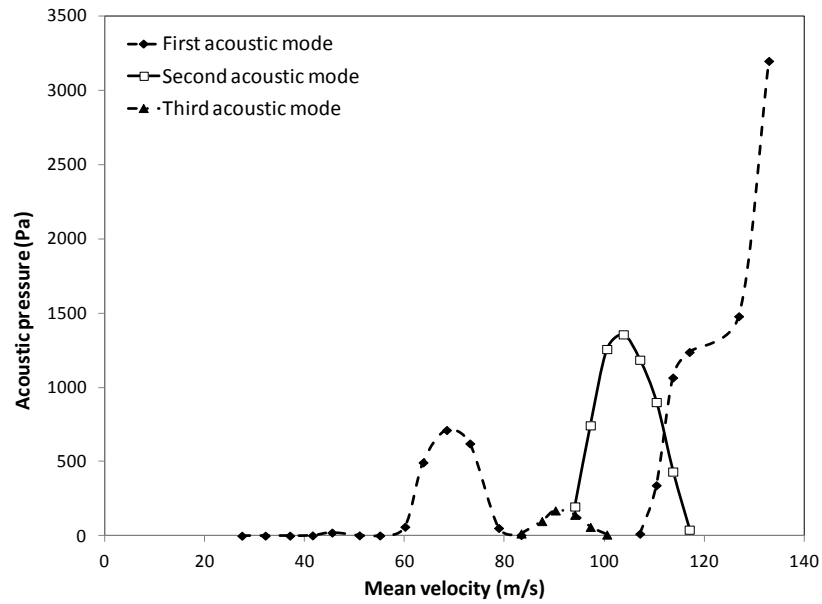


Figure 4-25 Pressure amplitudes of excited acoustic modes at different flow velocities for base case B4 (1/2, 2),  $d=12.5\text{mm}$ ,  $L/d=4$ ,  $d/D=1/12$

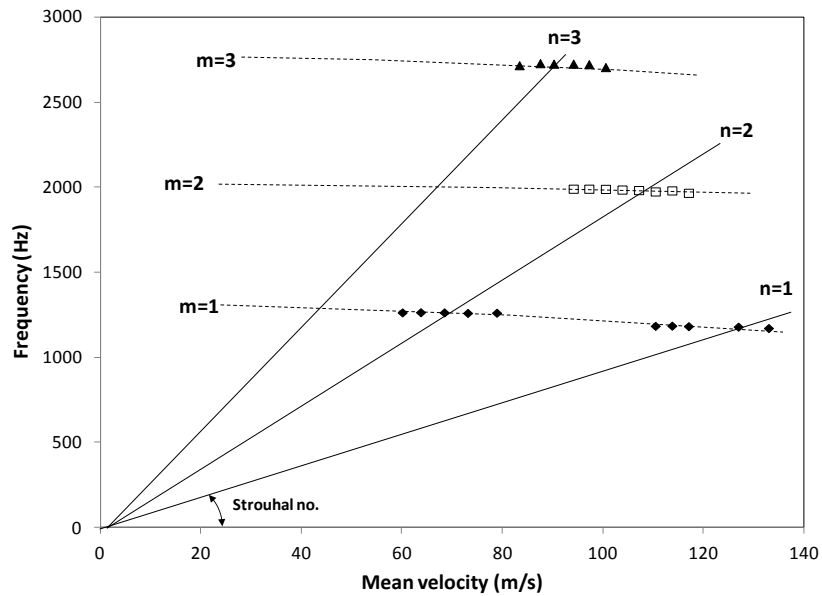


Figure 4-26 Frequency of excited acoustic modes at different flow velocities for base case B4 (1/2, 2),  $d=12.5\text{mm}$ ,  $L/d=4$ ,  $d/D=1/12$

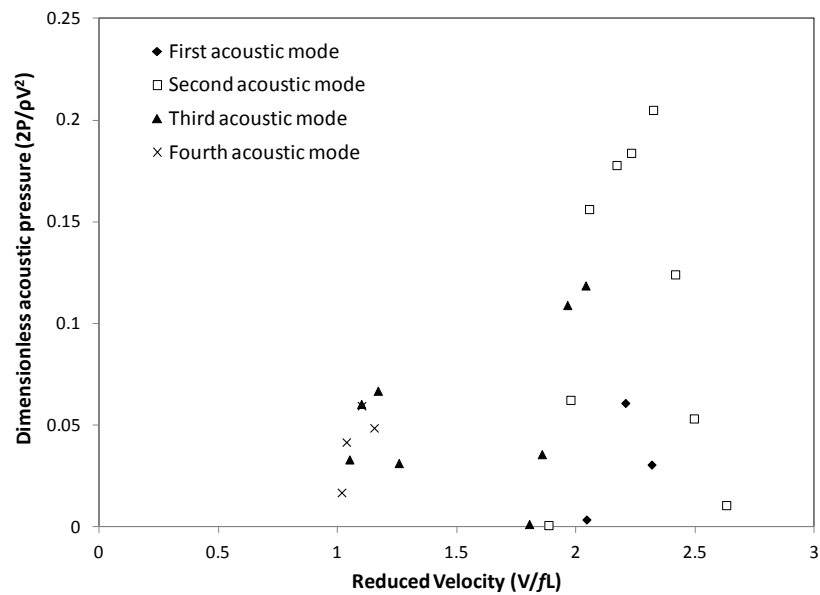


Figure 4-27 Dimensionless acoustic pressures ( $P/\frac{1}{2}\rho V^2$ ) versus reduced velocity ( $V_r = V/fL$ ) for base case B3 (1/2, 1),  $d=12.5\text{mm}$ ,  $L/d=2$ ,  $d/D=1/12$

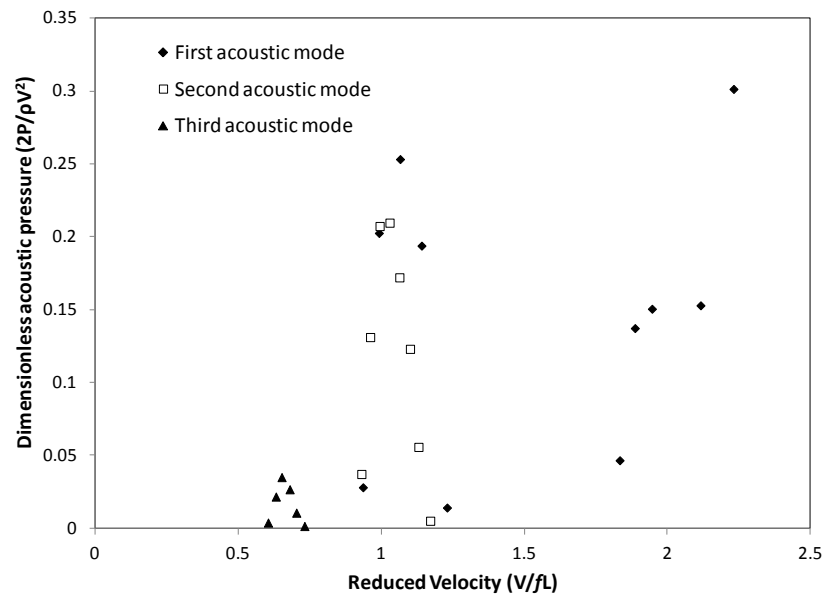


Figure 4-28 Dimensionless acoustic pressures ( $P/\frac{1}{2}\rho V^2$ ) versus reduced velocity ( $V_r = V/fL$ ) for base case B4 (1/2, 2),  $d=12.5\text{mm}$ ,  $L/d=4$ ,  $d/D=1/12$

## 4.2.2 Suppression devices

The previous section shows that the acoustic pressure amplitudes are much lower for the half inch cavity depth compared to that of the one inch cavity depth. Therefore, it is expected that the introduction of suppression devices would be more effective in reducing and/or delaying the acoustic resonance. Two suppression devices are tested for the half inch deep cavities. First, the chamfer insert is tested at the cavity leading edge, and the second insert tested is the spoiler upstream the cavity.

An upstream chamfer with  $l/L = 0.2$  is tested in the half inch deep cavities. The chamfer had similar overall effect as in the case of one inch deep cavities. Figure 4-29 shows the effect of the chamfer on pressure amplitudes in the two inch cavity length. The figure shows one resonance zone is excited at the end of the velocity range. This is in contrast to the base case B4 (1/2, 2), for which three resonance zones are excited. The chamfer succeeded in delaying the lock-in to 120 m/s. In addition, the maximum pressure peak reached is 45% lower than that reached in the base case.

Generally, the effect of the chamfer in the one inch cavity length is similar to the two inch cavity length. In other words, the chamfer was capable of delaying resonance to 115 m/s. Also, the suppression of the acoustic pressure amplitudes reached 28% in comparison to the base case B3 (1/2, 1). Figure A-11 showing the result of the chamfer in the one inch cavity length is found in the Appendix A.

Tests with spoiler (3) follows the same procedures as before in testing spoilers for the one inch deep cavities. Spoiler (3) has a configuration of 20 teeth; 9.75mm chamfer length, 7.0 mm tooth height, 6° tooth width and 12° spacing between the teeth. The spoiler is tested upstream the cavity for one inch and two inch cavity lengths.

Figure 4-30 shows the effect of spoiler (3) for the two inch cavity length. The figure shows complete suppression of the acoustic modes in case of the spoiler in comparison to the base case. The suppression is accomplished throughout the

velocity range. The difference between the effectiveness of the chamfer and the spoiler is concluded by comparing figure 4-29 and figure 4-30. The comparison shows the spoiler exceeded the chamfer in completely suppressing acoustic modes and their peaks. On the other hand, the spoiler increased the loss coefficient of the system. This is clearly shown by the decrease in the maximum flow velocity that is achieved when the spoiler is installed in comparison to the base and the chamfer cases.

The effect of spoiler (3) in the one inch long cavity is similar to the two inch cavity length. Figure A-12 showing these results is found in the Appendix A. The two plots point out that spoiler (3) is capable of providing 3-D disturbances to the shear layer perturbation at the cavity leading edge. This disturbances result in disturbing the coupling of the shear layer perturbations and the acoustic particle velocity at the leading edge. As a result, a weaker resonance is produced until reaching the maximum capacity of the blower.

### 4.2.3 Summary of half inch cavity depth

- This section examined the half inch base cases in details. It showed the differences and the similarities between half inch deep cavities and one inch deep cavities in form of acoustic response, pressure amplitudes and the frequency of excited acoustic modes.
- Upstream chamfer of  $\ell/L = 0.2$  was tested upstream the cavity for one inch and two inch cavity lengths. The chamfer succeeded in delaying modes to higher flow velocities in comparison to the base cases. Also, the maximum recorded acoustic pressure was only 28% and 40% of one inch and two inch cavity lengths, respectively.
- Finally, spoiler (3) was tested upstream the cavity for one inch and two inch cavity lengths. The spoiler completely suppressed the acoustic modes throughout the velocity range. This is achieved at the cost of increasing the loss coefficient of the system.

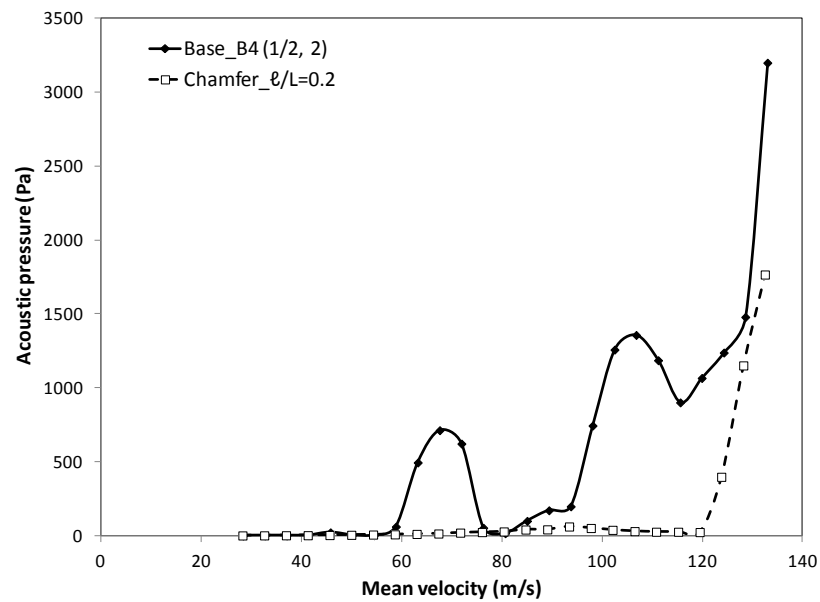


Figure 4-29 Influence of chamfer on pressure amplitudes of excited acoustic modes at different flow velocities,  $d=12.5\text{mm}$ ,  $L/d=4$ ,  $d/D=1/12$ , \_\_\_base, --- chamfer

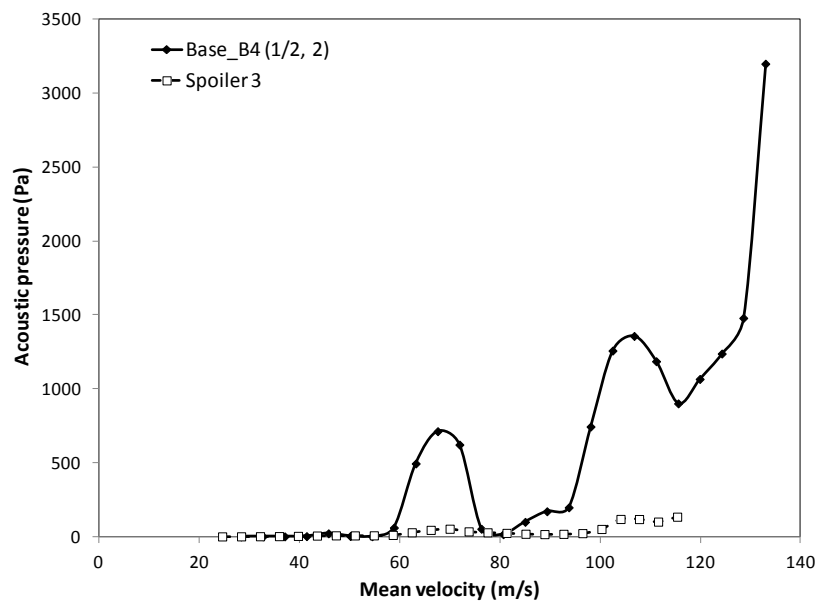


Figure 4-30 Influence of spoiler (3) on pressure amplitudes of excited acoustic modes at different flow velocities,  $d=12.5\text{mm}$ ,  $L/d=4$ ,  $d/D=1/12$ , \_\_\_base, --- spoiler

In the previous section covering smaller cavity sizes, the suppressive device needed was simple in design. The next section will examine the response of deeper cavities and the effect of different suppression devices on the excited diametral modes.

### **4.3 Results of Two Inch cavity depth ( $d = 50\text{mm}$ )**

This section presents the results of two inch deep cavities. The one inch long ( $L/d=0.5$ ) and the two inch long ( $L/d=1$ ) cavities are tested. The results of the base cases B5 (2, 1) for the one inch long cavity and B6 (2, 2) for the two inch long cavity are discussed in section 4.3.1. This is followed by the discussion of the results of the suppression seats tested for the one inch and the two inch cavities in section 4.3.2. The results will show different acoustic modes excited by the different shear layer modes. The amplitude of acoustic pressure and frequency of these modes as a function of mean flow velocity will also be presented.

#### **4.3.1 Base Cases B5 (2, 1) and B6 (2, 2)**

This section illustrates in detail the main characteristics of the excitation mechanism of the diametral modes for the base cases B5 (2, 1) and B6 (2, 2). Those two cases are for the one inch and the two inch cavity lengths, respectively.

The amplitude and frequency of the dominant peaks in the pressure spectra for base case B5 (2, 1) are presented in figures 4-31 & 4-32, respectively. Figure 4-31 shows the pressure amplitudes of the excited acoustic modes ( $m=1-3$ ) by shear layer modes ( $n=1$  &  $2$ ) versus flow velocity. The pressure amplitudes ranged from 0.5 Pa to 20710 Pa for the velocity range of 23-131 m/s. This velocity range corresponds to Mach number of 0.067- 0.38. The resonance frequencies of the excited acoustic modes by first and second shear layer modes as a function of flow velocity for the base case B5 (2, 1) are shown in figure 4-32. Each data point of resonance in this plot is the frequency of the corresponding amplitude data point presented in the previous plot at the same flow velocity. The plot shows that the resonance frequencies of the excited acoustic modes ( $m=1-3$ ) decrease slightly along the flow velocity. This is quite noticeable by the dotted lines drawn. The

shear layer modes exciting the acoustic modes have specific ranges of Strouhal number ( $St=f L/V$ ). The Strouhal number is represented by the slope of the straight and continuous lines indicated in the figure. These continuous lines pass around the peak pressure amplitudes of the excited acoustic resonance. At the beginning of the velocity range, the second acoustic mode ( $m=1$ ) is excited by the second shear layer ( $n=2$ ) over the velocity range of 23-56 m/s. The maximum pressure amplitude over this velocity range is 563 Pa. As the velocity increases, the first acoustic mode ( $m=1$ ) is excited over the velocity range of 56-94 m/s. This is followed by the second acoustic mode over the velocity range of 94-127 m/s. The excited first and the second acoustic modes reached maximum acoustic pressures of 16090 Pa and 20710 Pa, respectively. Finally, the third acoustic mode ( $m=3$ ) is excited over the velocity range of 118-131 m/s. The maximum pressure amplitude over this velocity range is 8386 Pa. The acoustic modes ( $m=1-3$ ) are excited by the first shear layer mode ( $n=1$ ) as shown in figure 4-32.

The results of the base case B6 (2, 2) are shown in figures 4-33 & 4-34. The two figures show the pressure amplitude and resonance frequencies, respectively for the excited acoustic modes as a function of flow velocity. Again the behavior in this case is similar to B5 (2, 1) discussed previously. It should be pointed out that increasing the cavity length resulted in higher pressure amplitudes compared to B5 (2, 1). Moreover, the diametral frequencies did not change compared to B5 (2, 1). In addition, the shear layer mode frequencies decrease with the increase of the cavity length.

Figures 4-35 and 4-36 show the dimensionless amplitude of the acoustic pressure as a function of reduced velocity for the base cases B5 (2, 1) and B6 (2, 2), respectively. Figure 4-35 shows the dimensionless pressure ( $P/\frac{1}{2}\rho V^2$ ) plotted against the reduced velocity based on the cavity length ( $V_r = V/f L$ ). The second shear layer mode ( $n=2$ ) has a reduced velocity range from 1.12-1.5. The Maximum dimensionless amplitude is 0.45 and it occurs at a reduced velocity of 1.2. The first shear layer mode ( $n=1$ ) has a reduced velocity ranged from 2.2-3.2. The Maximum dimensionless amplitude is 4.2 and it occurs at a reduced velocity of 2.8. Figure 4-36 shows the third shear layer mode ( $n=3$ ) for B6 (2, 2) has a reduced velocity ranged from 0.57-0.65. The maximum dimensionless amplitude

is 0.63 and it occurs at a reduced velocity of 0.65. The second shear layer mode ( $n=2$ ) has a reduced velocity ranged from 0.74-1.1. The maximum dimensionless amplitude is 2.2 and it occurs at a reduced velocity of 1.0. The first shear layer mode ( $n=1$ ) has a reduced velocity ranged from 1.6-2.4. The maximum dimensionless amplitude is 3.1 and it occurs at a reduced velocity of 2.4.

Generally the effect of increasing the cavity *depth* on pressure amplitude in either dimensional or dimensionless form can be pointed out as follows: the maximum dimensionless pressure as well as maximum pressure amplitudes reached for the two inch deep cavities ( $d/D=4/12$ ) are higher than that reached by one inch deep cavities ( $d/D=2/12$ ). For example, the maximum dimensionless acoustic pressure reached by first diametral mode for the base case B5 (2, 1) (recall fig.4-35) is higher than that reached for the base case B1 (1, 1) (recall fig.4-7) by factor of 2.7. Same observation stands for the base case B6 (2, 2) (recall fig.4-36), the first diametral mode reaches a maximum dimensionless pressure higher than the base case B2 (1, 2) (recall fig.4-8) by factor of 3.5.

Regarding the resonance frequencies, the frequencies of the two inch deep cavities are lower than those of one inch deep cavities. For example at flow velocity of 55 m/s, the resonance frequency for the base case B5 (2, 1) is 1014 HZ while the base case B1 (1, 1) is 1265 HZ. This is a result of the increase in the average diameter of the system. The frequencies of the diametral modes do not seem to experience a substantial reduction with the increase of the mean flow velocity for the two inch deep cavities. On the other hand, a reduction was observed for previously studied cavities. Considering all the previous observations, it is evident that the frequencies of the diametral acoustic resonance modes decrease with the mean flow velocity when the cavity size is small.

The next section examines the results and the analyses of introducing different suppression seats for deep cavities.

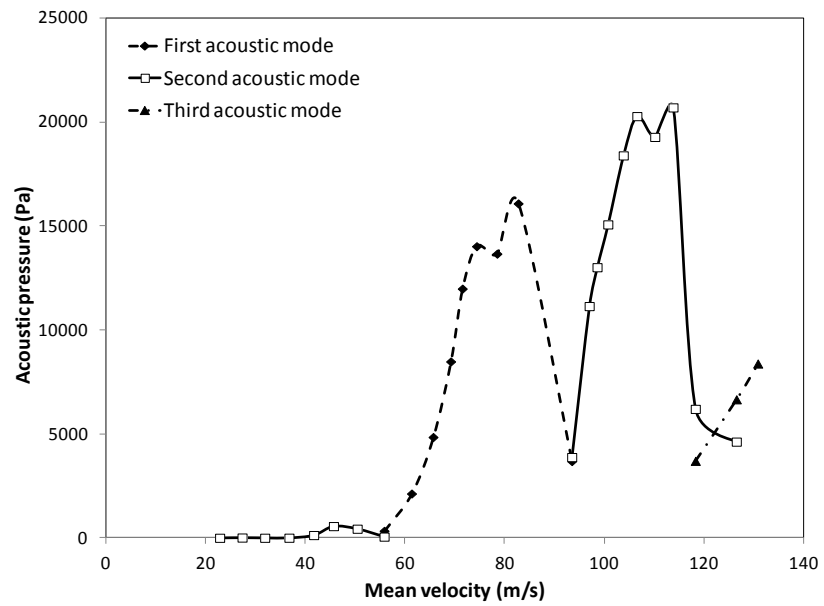


Figure 4-31 Pressure amplitudes of excited acoustic modes at different flow velocities for base case B5 (2, 1),  $d=50\text{mm}$ ,  $L/d=0.5$ ,  $d/D=4/12$

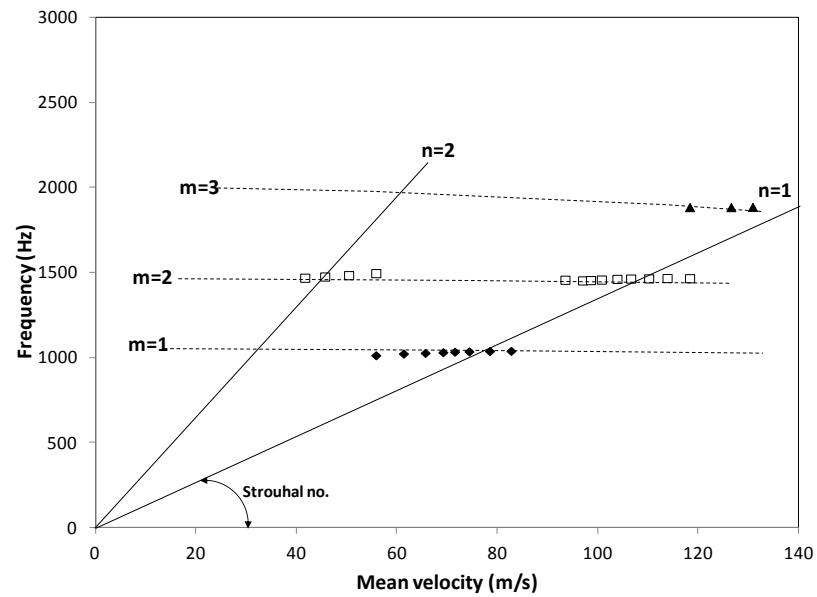


Figure 4-32 Frequency of excited acoustic modes at different flow velocities for base case B5 (2, 1),  $d=50\text{mm}$ ,  $L/d=0.5$ ,  $d/D=4/12$

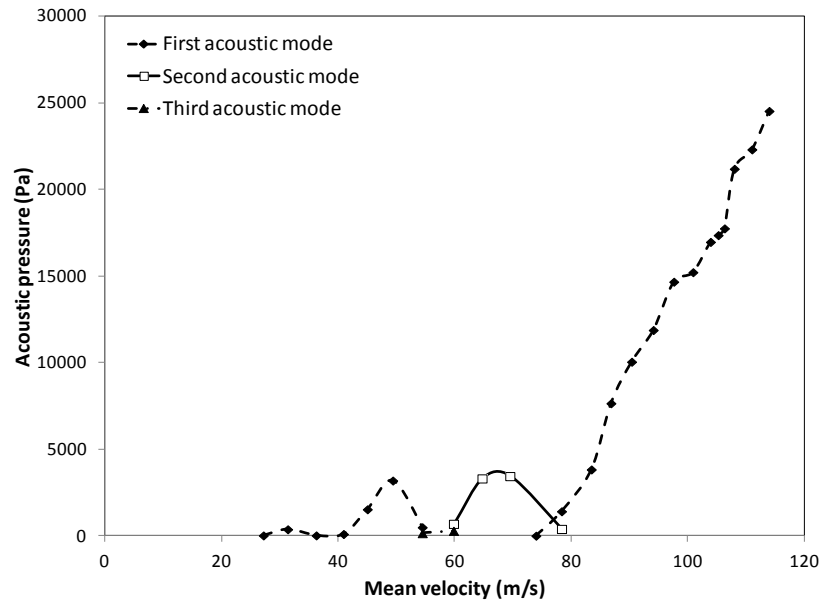


Figure 4-33 Pressure amplitudes of excited acoustic modes at different flow velocities for base case B6 (2, 2),  $d=50\text{mm}$ ,  $L/d=1$ ,  $d/D=4/12$

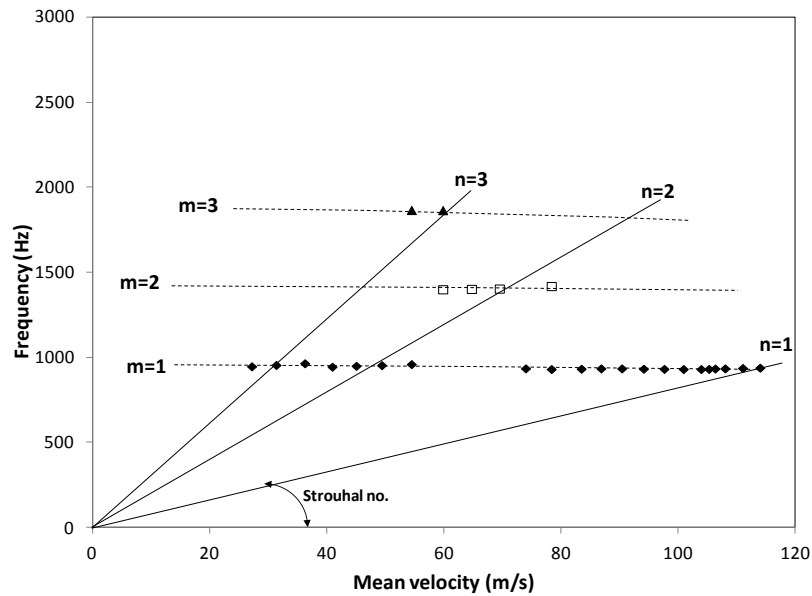


Figure 4-34 Frequency of excited acoustic modes at different flow velocities for base case B6 (2, 2),  $d=50\text{mm}$ ,  $L/d=1$ ,  $d/D=4/12$

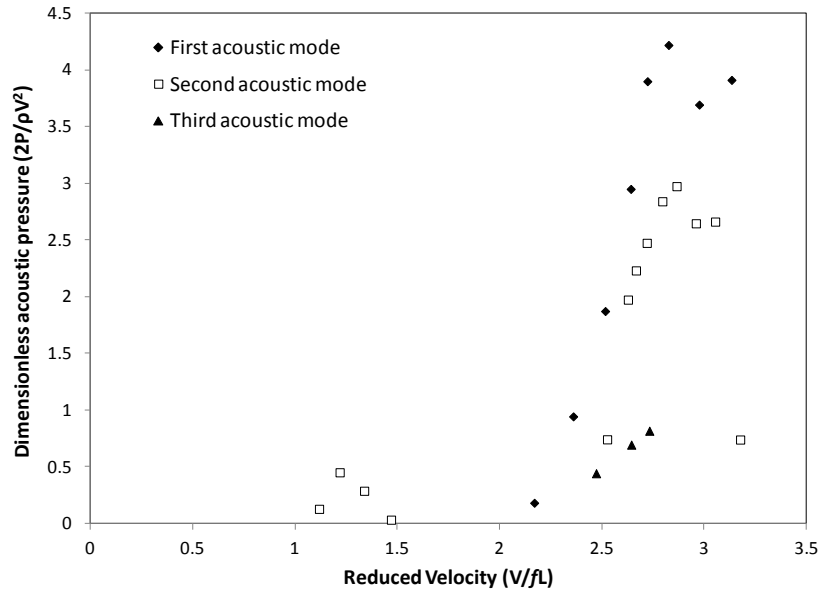


Figure 4-35 Dimensionless acoustic pressures ( $P/\frac{1}{2}\rho V^2$ ) versus reduced velocity ( $V_r = V/fL$ ) for base case B5 (2, 1),  $d=50\text{mm}$ ,  $L/d=0.5$ ,  $d/D=4/12$

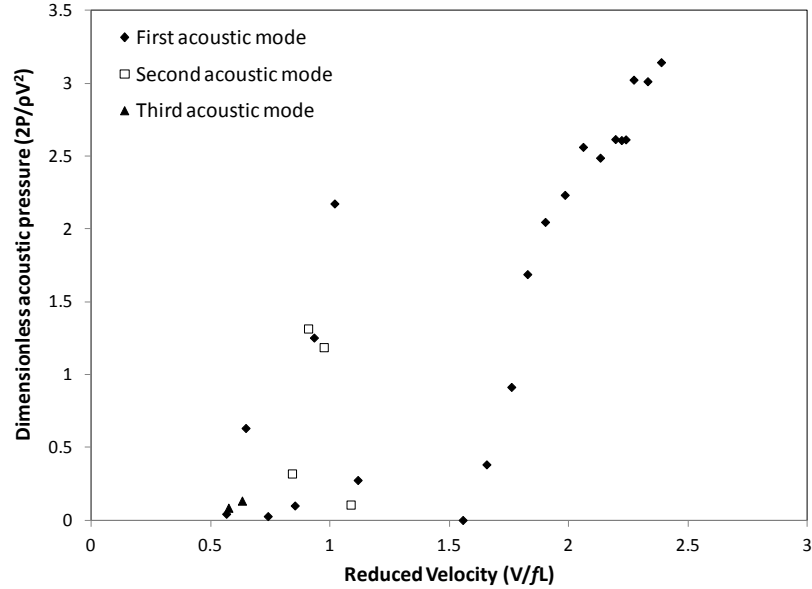


Figure 4-36 Dimensionless acoustic pressures ( $P/\frac{1}{2}\rho V^2$ ) versus reduced velocity ( $V_r = V/fL$ ) for base case B6 (2, 2),  $d=50\text{mm}$ ,  $L/d=1$ ,  $d/D=4/12$

### 4.3.2 Suppression results

The previous sections showed that the two inch deep cavities strongly excite diametral modes with higher pressure amplitudes compared to half inch deep and one inch deep cavities. Therefore, it is expected that a bigger suppression devices to suppress and/or delay resonance is required. Two types of suppression devices are tested for two inch deep cavities. First, an upstream chamfer insert is introduced. Second, spoiler inserts of three different configurations are tested.

The long chamfer ( $l = 9.75$  mm) is tested in the one inch and the two inch cavity lengths. Generally, the effect of the chamfer is not as effective as previously tested in one inch deep and half inch deep cavities. Figure 4-37 shows the effect of the long chamfer on the acoustic pressure amplitudes along the flow velocity for two inch cavity length. The figure shows that the chamfer excites three resonance zones as in the base case B6 (2, 2). In addition, the maximum pressure amplitude reached by the chamfer is approximately similar to the base case. Also, the delay of resonance achieved is in the range of 5 m/s when compared to the base case B6 (2, 2). As a result of increasing the cavity length by the addition of the chamfer, the shift of data points is more obvious. This is clearly shown by the maximum amplitude in case of chamfer occurs at 119 m/s whilst the base case occurs at 114 m/s. For the one inch long cavity, the chamfer increased maximum pressure amplitudes by factor of 1.16. The delay of resonance was less than 10 m/s in comparison to the base case B5 (2, 1). Figure A-13 shows result of this case in the Appendix A.

The second suppression device tested in two inch deep cavities is the spoiler. Spoiler (4) is similar in shape to spoiler (1) to (3). Spoiler (4) has the configuration of 20 teeth; 9.75mm chamfer length, 9 mm tooth height, 6° tooth width, and 12° spacing between teeth. The spoiler is tested upstream the one and the two inch cavity lengths.

The effect of spoiler (4) in the two inch long cavity is shown in figure 4-38. The figure shows that the spoiler excites three resonance zones similar to the base case B6 (2, 2). Spoiler (4) reduced the maximum acoustic pressure amplitude by a

factor of 3.2 compared to the base case. Moreover, the spoiler did not delay resonance to a higher flow velocity. Yet, it succeeded in partially suppressing the weak resonances appearing below 85 m/s. One more thing the plot reveals is that the maximum flow velocity reached in case of the spoiler is higher than that reached in the base case. The reason behind this might be the higher pressure amplitudes in the base case increased the resistance of the system. Thus the maximum blower speed reached a maximum flow velocity of 114 m/s for the base case. This hypothesis needs to be tested by measuring the pressure loss over the cavity. However, the amplitudes are much lower in case of the spoiler compared to the base case. As a result, the maximum flow velocity reached with spoiler installed is higher; 122 m/s. For the one inch long cavity, spoiler (4) suppressed high acoustic pressure amplitudes by factor of 4.4 compared to the base case B5 (2, 1). Also, the spoiler completely suppressed weak resonances below 59 m/s. On the other hand, the spoiler increased the loss coefficient of the system. This is clearly manifested by the decrease in the maximum flow velocity that is achieved when the spoiler is installed in comparison to the base case. The result of spoiler (4) in the one inch cavity length is shown in the figure A-14 of the Appendix A.

The suppression of acoustic pressure amplitudes achieved by spoiler (4) is a progress to the aim of the current study. This is to completely suppress or delay resonance throughout the velocity range for different cavity dimensions. The curved spoiler is designed with same parameters as spoiler (4) but with few alterations. The curved spoiler has the configuration of 20 teeth; 9.75mm chamfer length, 8.5 mm tooth height, 6° tooth width, 12° spacing between teeth, and a curved connection of radius 7 mm between the tip of tooth and half way the chamfer length (recall fig. 3-21(b)). The curved spoiler differs from spoilers (1) to (4) (or square-toothed spoilers). The square-toothed spoilers are designed to have a gradual increase with the help of upward ramp reaching the tip of the tooth, such that a gradual change in the area is introduced to the flow. Thus, minimizing the pressure drop associated with sudden change in area. On the other side, the curved spoiler is designed to alter the route of the vortices as well as the flow right into the middle of the cavity. This is done by the curvature joining the tip of the tooth

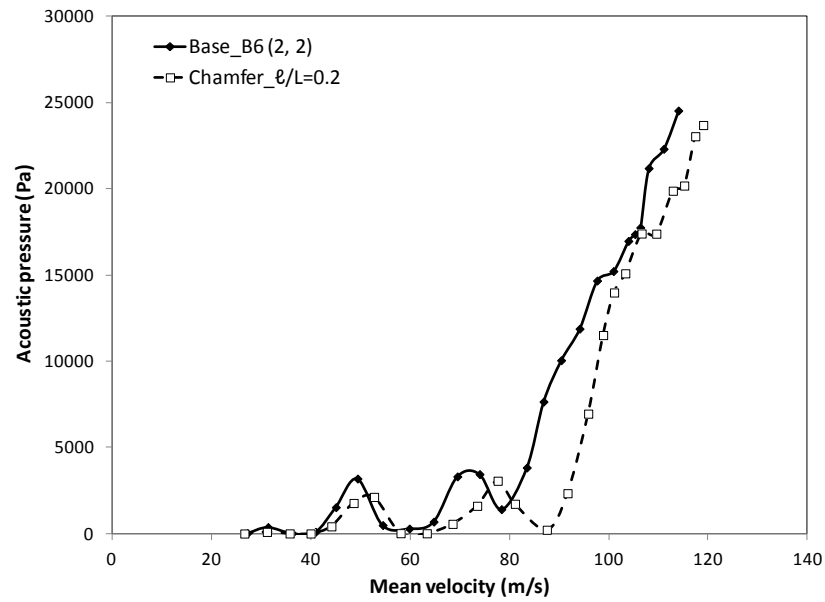


Figure 4-37 Influence of chamfer on pressure amplitudes of excited acoustic modes at different flow velocities,  $d=50\text{mm}$ ,  $L/d=1$ ,  $d/D=4/12$ , \_\_\_base, - - - chamfer

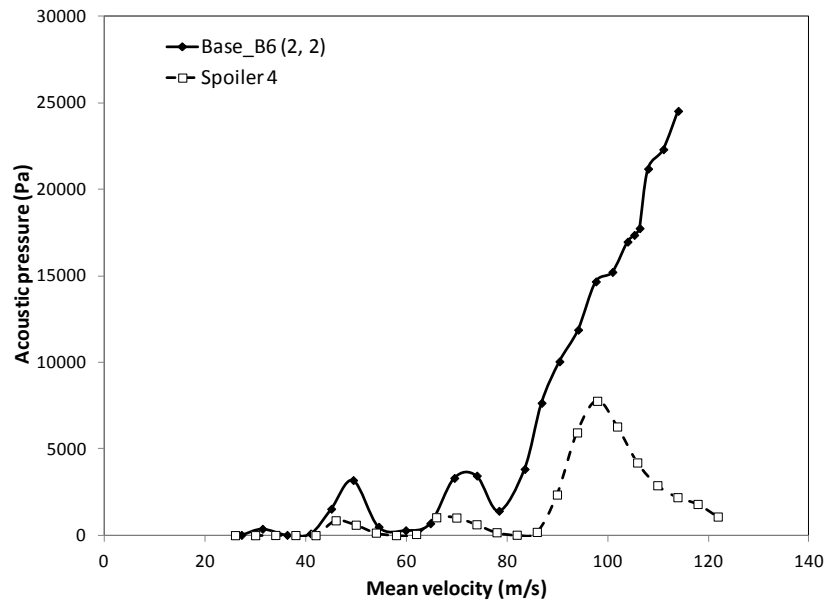


Figure 4-38 Influence of spoiler (4) on pressure amplitudes of excited acoustic modes at different flow velocities,  $d=50\text{mm}$ ,  $L/d=1$ ,  $d/D=4/12$ , \_\_\_base, - - - spoiler

and half way the chamfer length. The influence of the leading edge curved spoiler is tested in two inch deep cavities.

The influence of the curved spoiler on the resonance of the one inch cavity length is shown in figure 4-39. The figure shows two resonance zones are excited in case of the curved spoiler. Also, the base case B5 (2, 1) excites two strong and two weak resonance zones. In addition, the curved spoiler reduced the maximum acoustic pressure amplitudes by a factor of 6.5 compared to the base case B5 (2, 1). The curved spoiler completely suppressed weak resonances appearing below 52 m/s. On the other hand, the spoiler increased the loss coefficient of the system. This is clearly shown by the decrease in the maximum flow velocity that is achieved when the curved spoiler is installed compared to the base case. A comparison between the effect of the curved spoiler and spoiler (4) for one inch long cavity is needed. The comparison improves the insight on the progress towards the aim of current study. The curved spoiler suppressed the acoustic pressure amplitudes by a higher factor than that achieved by spoiler (4). The maximum flow velocity reached in case of spoiler (4) is higher than that reached in curved spoiler. This points out that the curved spoiler increases the system loss coefficient more than spoiler (4).

Figure 4-40 shows the effect of the curved spoiler on the acoustic pressure amplitudes along flow velocity for two inch cavity length. The figure shows that both the curved spoiler and the base case excited three resonance zones. The curved spoiler reduced the maximum acoustic pressure amplitude by a factor of 7.6 compared to the base case B6 (2, 2). The maximum flow velocity reached by the curved spoiler is higher than that reached by the base case. The reason behind this might be the higher pressure amplitudes in the base case increased the resistance of the system. Thus the maximum flow velocity in case of the curved spoiler is 118 m/s. The difference between the effectiveness of the curved spoiler and the square-toothed spoiler (4) is concluded by comparing figures 4-40 and 4-38. The comparison shows that below 86 m/s flow velocity both spoilers partially suppressed weak resonances. The suppressed pressure amplitudes by the curved spoiler are of lower values compared to spoiler (4). In addition, the maximum

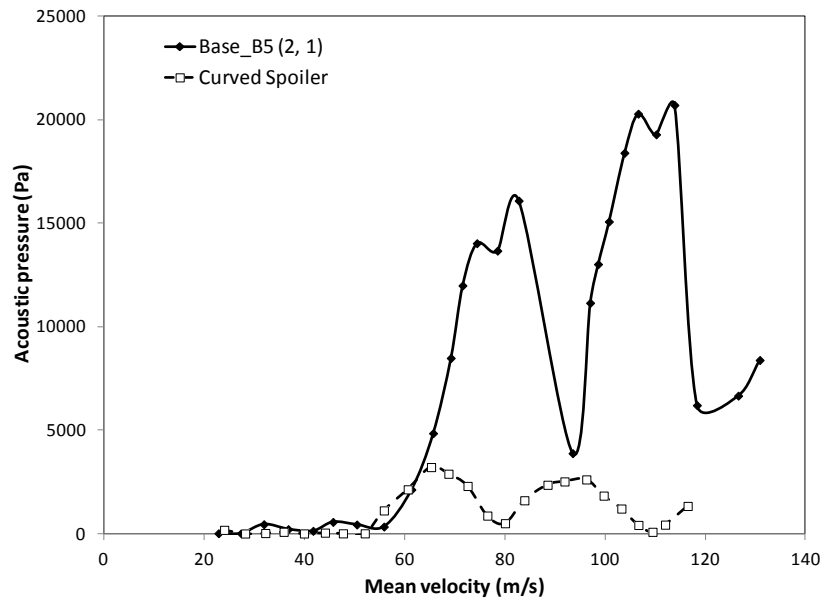


Figure 4-39 Influence of curved spoiler on pressure amplitudes of excited acoustic modes at different flow velocities,  $d=50\text{mm}$ ,  $L/d=0.5$ ,  $d/D=4/12$ , \_\_\_base, - - - spoiler

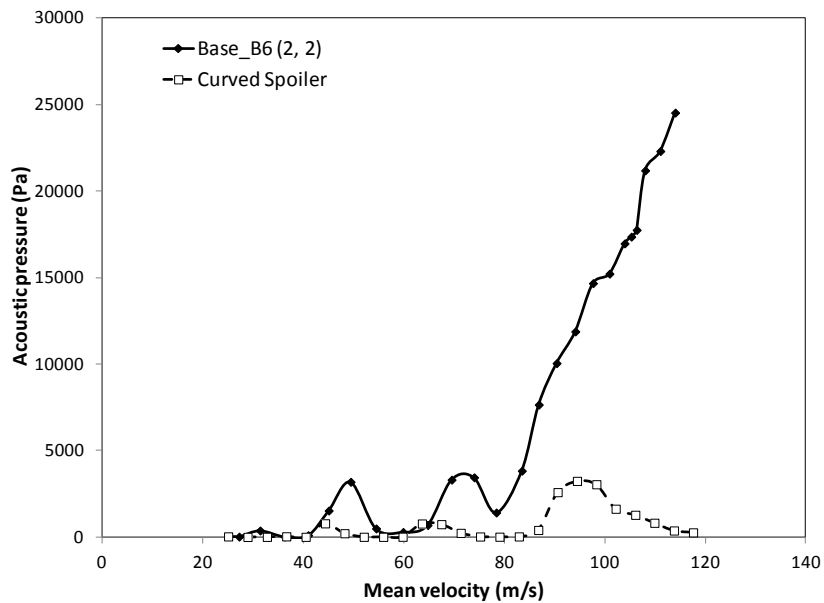


Figure 4-40 Influence of curved spoiler on pressure amplitudes of excited acoustic modes at different flow velocities,  $d=50\text{mm}$ ,  $L/d=1$ ,  $d/D=4/12$ , \_\_\_base, - - - spoiler

flow velocity reached by the curved spoiler is lower than that reached by the square-toothed spoiler.

One last spoiler of totally different configuration than previous ones tested in the current study is the delta spoiler. The delta spoiler has the configuration of 18 mm thickness, 26 teeth, 6 mm tooth height, 2 mm and 4 mm tooth thickness at the tip and the base of the tooth, respectively. The teeth have 30°- 32° angle of incidence. Also, the delta spoiler has no chamfer. The principle of the delta spoiler involves the production of streamwise vortices at an angle that allows collision with the mean flow. Thus cancelling off some the primary vortices formed by shear layer perturbation. The delta spoiler is tested upstream the one inch and the two inch cavity lengths.

The influence of the delta spoiler on pressure amplitudes along the flow velocity in the one inch long cavity is shown in figure 4-41. The figure shows the delta spoiler excited three resonance zones of nearly the same maximum pressure amplitudes. This is in contrast to the base case B5 (2, 1) where two strong and two weak resonances are excited. The maximum pressure amplitude in case of spoiler is reduced by a factor of 6.8 compared to the base case. In addition, partial suppression of weak resonances appearing below 52 m/s flow velocity is accomplished upon the introduction of the delta spoiler. The overall acoustic response while using the delta spoiler is similar to the response while using the curved spoiler. Yet, the delta spoiler was capable of reaching a higher maximum flow velocity than curved spoiler. This result agrees in a way with what Karadogan & Rockwell (1983) found when tested two different configurations of vortex generators. They found that vortex generators having either the same or an alternating angle, of incidence with respect to the mean flow were equally effective in attenuation. For the two inch long cavity, the results of the delta spoiler are shown in figure 4-42. The figure shows complete suppression of acoustic pressure amplitudes throughout the flow velocity range is achieved in case of delta spoiler compared to the base case B6 (2, 2). The difference between the effectiveness of the delta, curved and the square-toothed spoilers is concluded by comparing 4-42, 4-40, and 4-38, respectively. The comparison shows that the

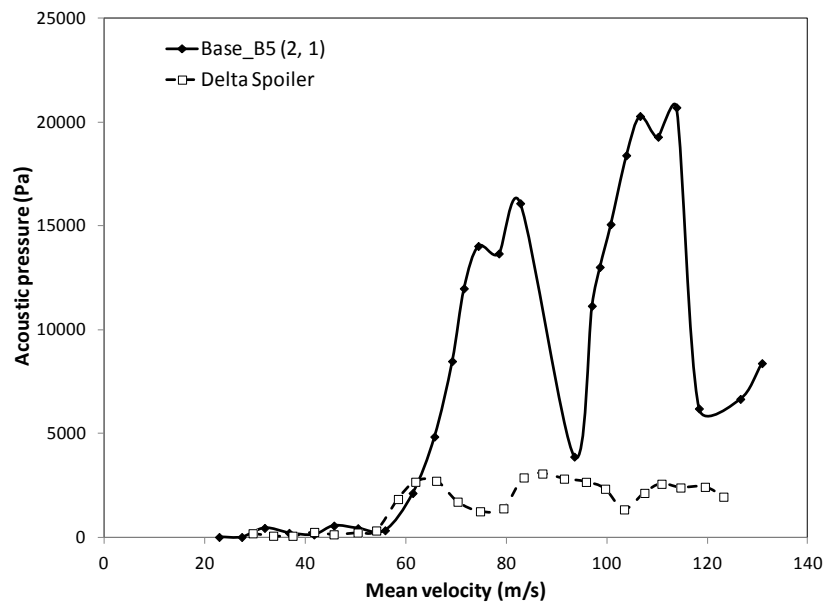


Figure 4-41 Influence of delta spoiler on pressure amplitudes of excited acoustic modes at different flow velocities,  $d=50\text{mm}$ ,  $L/d=0.5$ ,  $d/D=4/12$ , \_\_\_base, - - - spoiler

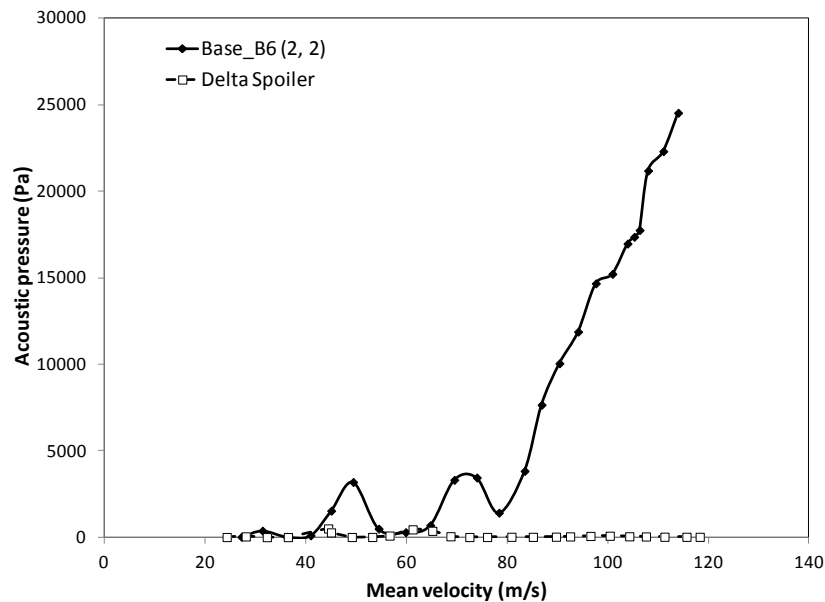


Figure 4-42 Influence of delta spoiler on pressure amplitudes of excited acoustic modes at different flow velocities,  $d=50\text{mm}$ ,  $L/d=1$ ,  $d/D=4/12$ , \_\_\_base, - - - spoiler

suppression of acoustic pressure amplitudes achieved with the delta spoiler is higher than the curved spoiler and spoiler (4).

### **4.3.3 Summary of two inch Cavity depth (d=50mm)**

- This section examined the two inch deep base cases in details, showing the differences and the similarities between two inch deep cavities and one inch deep cavities in form of acoustic response, pressure amplitudes and the frequency of excited acoustic modes.
- The long chamfer was tested upstream of the cavity for one inch and two inch cavity lengths. The chamfer showed totally different response than previously tested cavities. The acoustic pressure amplitudes were slightly increased in the one inch long cavity and reduced in the two inch long cavity. Also, the delay of resonance in either cavity was minimal.
- Three different spoiler configurations are tested upstream one inch and two inch long cavities. The spoilers are square toothed spoiler (4), curved spoiler and delta spoiler. The three spoilers delayed resonance to higher flow velocity. Also, a considerable suppression of pressure amplitudes throughout the flow velocity range has been achieved.

# CHAPTER 5

## Summary and Conclusions

---

### 5.1 Summary and Conclusions

Different passive suppression techniques of different configurations were tested for an internal axisymmetric cavity. The flow over the tested cavity excites the acoustic diametral modes classified as trapped modes. The associated acoustic pressure level decays exponentially with axial distance away from the cavity. An experimental setup of a cavity-duct system has been altered to facilitate the study of the suppression and/or delay of resonance. This is done over the range of Mach number of 0.07-0.4. Three different cavity depths have been investigated with cavity depth ( $d$ ) to pipe diameter ( $D$ ) ratios of 1/12, 2/12 & 4/12. These ratios correspond to cavity depth of 12.7 mm (half inch), 25.4mm (one inch), and 50.8 mm (two inches) deep. For each depth, the cavity length ( $L$ ) was changed from 25.4mm (one inch) to 50.8mm (two inch) which corresponds to  $L/d=0.5$  to 4. The characteristics of the upstream boundary layer have been previously determined by Aly (2008) using a hotwire anemometer. The acoustic response has been measured by a series of pressure transducers fixed at the level of the inner surface of cavity floor.

Rounding the cavity edges was investigated for the one inch deep cavities. The study of two rounding radii upstream and downstream the cavity was considered. It was found that rounding off cavity edges for both radii have increased the acoustic pressure level at resonance. However, it delayed the onset of resonance as a result of the increase of the cavity characteristic length. Based on these findings, rounding off the upstream and the downstream cavity edges was not further investigated for the other two cavity depths. Moreover, using

effective cavity length ( $L_e$ ) as the characteristic length eliminated the apparent delay in reduced velocity resonance range. Based on the findings of this research, the effective cavity length is the length of the cavity ( $L$ ) and upstream radius of curvature ( $r$ ). These results for trapped mode resonances agree with those in literature dealing with longitudinal acoustic resonances.

The second passive suppressive method tested for the three cavity depths was chamfering the upstream edge of the cavity. The study also includes the investigation of the effect of changing the length of chamfer for the one and two inch cavity lengths. The chamfer of the upstream edge is found to increase cavity characteristic length which delays the coupling of the shear layer perturbations and the acoustic field. Chamfering the upstream edge also changes the characteristics of the free shear layer. This change affects the coupling between the free shear layer and the acoustic particle velocity. The test data shows that these changes results in producing somewhat weaker resonance.

The chamfer of  $\ell/L=0.2$  was effective in delaying the lock-in of resonance in half inch deep and one inch deep cavities to higher flow velocities. In addition, the maximum pressure amplitudes reached upon adding the  $\ell/L=0.2$  chamfer were much lower than the corresponding base cases. As the cavity size increases the effect of the chamfer declines greatly. In two inch deep cavities, the  $\ell/L=0.2$  chamfer caused insignificant delay of resonance to higher flow velocity. In addition, the values of pressure amplitudes reached in these cases were very much similar to the corresponding base cases.

The effect of changing the chamfer length to cavity length ratio ( $\ell/L$ ) is also studied in one inch deep cavities. Increasing the chamfer length; chamfer of  $\ell/L=0.4$ , delayed the resonance to higher flow velocity than that by the chamfer of  $\ell/L=0.2$ . In addition, the maximum acoustic pressure reached in case of  $\ell/L=0.4$  chamfer was lower than that achieved in the  $\ell/L=0.2$  chamfer. On the other hand, decreasing the chamfer length in the two inch long cavity, the  $\ell/L=0.1$  chamfer, reduced the resonance delay than the  $\ell/L=0.2$  chamfer. Also, there was almost no reduction in amplitudes of acoustic pressure by the  $\ell/L=0.1$  chamfer. Unlike the

$l/L=0.2$  chamfer, the maximum pressure amplitude reached half the corresponding value in the base case.

The third and final suppressive seat investigated here is the leading edge spoilers with mainly three different configurations; square-toothed, curved, and delta spoilers. Leading edge spoilers were tested in the three cavity depths. The effect of square toothed spoiler is providing 3-D disturbances to shear layer perturbation at the separation edge. As the shear layer instabilities increase, the coupling of the shear layer oscillations with acoustic field becomes three dimensional and incoherent. As a result, lower acoustic power is generated; weaker resonance. And therefore weaker upstream effect which dampens the acoustic resonance. The square toothed spoilers were designed to have a gradual increase till reaching the tip of the tooth. Thus, the change in area is introduced gradually to the flow. This minimizes the pressure drop associated with sudden change in area. The test results showed that the strength of the excited resonance increases as the cavity size increases. This means that larger sized spoilers would be needed in order to successfully delay and suppress the acoustic resonances. Four different designs of square toothed spoilers were investigated in the three cavity depths. The designs would differ in number of teeth, tooth height, tooth width, spacing between teeth and chamfer length. The four square toothed spoilers succeeded; to a varying degrees, in delaying and suppressing the acoustic resonance in the three cavity depths.

The second configuration of leading edge spoiler is the curved spoiler. The curved spoiler was designed with similar parameters as square toothed spoilers with few alterations. It was designed to alter the route of the vorticity as well as the flow right into the middle of the cavity. This is done by the curvature joining the tip of the tooth and half way the chamfer length. Finally, the delta spoiler investigated had totally different configuration from the previously tested spoilers. The principle of the delta spoiler involves the production of streamwise vorticity at an angle that allows collision with the mean flow. Thus, dissipating some of the primary vorticity formed by the shear layer. The overall suppression of the acoustic resonance achieved while using the delta spoiler was much better than that while using the curved and the square toothed spoilers.

## 5.2 Suggestions for future work

This study has showed the influence of three different passive suppression techniques in axisymmetric cavity. It is recommended for future work to:

- Study in depth the effect of different parameters of chamfers and leading edge spoilers on acoustic response. These parameters might include shapes, angle of inclination, and sizes,
- Study more thoroughly the pressure drop caused by the leading edge spoilers. The effect of tooth height and how to minimize the pressure drop.
- Perform numerical simulations for different suppression methods and compare it with the experimental study. In order to further extent the knowledge of the shear layer mode behavior and acoustic particle velocity.

# References

- Aly, K., 2008. *Aerodynamic excitation of the diametral modes of an internal axisymmetric cavity*. Hamilton, Ontario, Canada: McMaster University.
- Aly, K. & Ziada, S., 2006. Flow excitation of diametral acoustic modes of axisymmetric Cavities. In *Proceedings of PVP*. Vancouver, BC, Canada, 2006. ASME.
- Bruggeman, J.C., Hirschberg, A., Van Dongen, M.E.H. & Gorter, J., 1991. Self-sustained aero-acoustic pulsations in gas transport systems: Experimental study of the Influence of closed side branches. *Journal of Sound and Vibration*, 150(3), pp.371-93.
- Cattafesta, L.N.III., Song, Q. & Williams, D., 2008. Active control of flow-induced cavity oscillations. *progress in Aerospace Sciences*, 44, p.479–502.
- Cattafesta, L., Williams, D., Rowley, C. & Alvi, F., 2003. Review of active control of flow-induced cavity resonance. In *AIAA Pap. 2003-3567.*, 2003.
- Chokani, N. & Kim, I., 1991. Suppression of pressure oscillations in an open cavity by passive pneumatic control., 1991. AIAA paper.
- Dequand, S., Hulshoff, S.J. & Hirschberg, A., 2003. Self-sustained oscillations in a closed side branch system. *Journal of Sound and Vibration*, 265, p.359–386.
- DiStefano, I.J., Stubberud, A. & Williams, I., 1990. Feedback and control systems. In *Schaum's outlines. 2nd ed.* New York, 1990. McGraw-Hill.
- Dix, R.E. & Bauer, R.C., 2000. *Experimental and theoretical study of cavity acoustics*. Tennessee: Arnold Air Force, Air Force Martial Command, United States Air Force Arnold Engineering Development centre.
- Ethembaoglu, S., 1973. *On the Fluctuating Flow Characteristics in the Vicinity of Gate Slots*. Divison of Hydraulic Engineering, University of Trondheim, Norwegian Institute of Technology.

Franke, M.E. & Carr, D.L., 1975. Effect of geometry on open cavity flow-induced pressure oscillations. *American Institute of Aeronautics and Astronautics*, pp.75-492.

Freymuth, P., 1966. On transition in a separated laminar boundary layer. *J. Fluid Mech. journal of fluid mechanics*, 25, pp.683-704.

Heller, H.H. & Bliss, D.B., 1975. Flow-induced pressure fluctuations in cavities and concepts for their suppression. *American Institute of Aeronautics and Astronautics*, pp.75-491.

Ho, C.M. & Hunang, L.S., 1982. Subharmonics and vortex merging in mixing layers. *journal of fluid mechanics*, 119, pp.443-73.

Howe, M.S., 1975. Contributions to the theory of aerodynamic sound, with application to excess jet noise and the theory of the flute. *Journal of Fluid Mechanics*, 71, pp.625-673.

Howe, M.S., 1980. The dissipation of sound at an edge. *Journal of Sound and Vibration*, 70, p.407–411.

Janzen, V.P. et al., 2007. Acoustic noise reduction in large diameter steam-line gate valve. In *Pressure Vessels and Piping Division*. Texas, 2007. Atomic Energy of Canada Limited.

Karadogan, H. & Rockwell, D., 1983. Toward attenuation of self-sustained oscillations of a turbulent jet through a cavity. *Journal of Fluids Engineering*, 105, pp.335-40.

Knotts, B.D. & Selamet, A., 2003. Suppression of flow–acoustic coupling in sidebranch ducts by interface modification. *Journal of Sound and Vibration*, 265 , p.1025–1045.

Krishnamurty, K.s., 1955. *Acoustic radiation from two-dimensional rectangular cutouts in aerodynamic surface*. NACA TN 3487.

Lawson, S.J. & Barakos, G.N., 2011. Review of numerical simulations for high-speed, turbulent cavity flows. *Progress in Aerospace Sciences*, 47(3), p.186–216.

- Miksad, R.W., 1972. Experiments on the nonlinear stages of free shear layer transition. *journal of fluid mechanics*, pp. 695-719.
- Nakiboglu, G. et al., 2009. A parametric study on the whistling of multiple side branch system as a model for corrugated pipes. In *Pressure Vessels and Piping*., 2009. Proceedings of the ASME.
- Nakiboglu, G., Belfroid, S.P.C., Willems, J.F.H. & Hirschberg, A., 2010. Whistling behavior of periodic systems: Corrugated pipes and multiple side branch system. *International Journal of Mechanical Sciences*, 52, p.1458–1470.
- Nakiboğlu, G. & Hirschberg, A., 2010. A numerical study of the aeroacoustic interaction of a cavity with a confined flow: Effect of edge geometry in corrugated pipes. Montreal, Canada, 2010.
- Nakiboğlu, G., Manders, H.B.M. & Hirschberg, A., 2012. Aeroacoustic power generated by a compact axisymmetric cavity: prediction of self-sustained oscillation and influence of the depth. *Journal of Fluid Mechanics*, 703, p.163\_191.
- Nelson, P.A., Halliwell, N.A. & Doak, P.E., 1981. Fluid dynamics of a flow excited resonance. Part I: experiment. *Journal of Sound and Vibration*, 78, p.15–38.
- Nelson, P.A., Halliwell, N.A. & Doak, P.E., 1983. Fluid dynamics of a flow excited resonance. Part II: flow acoustic interaction. *Journal of Sound and Vibration*, 91, p.375–402.
- Pereira, J.C.F. & Sousa, J.M., 1994. Influence of impingement edge geometry on cavity flow oscillation. *AIAA Journal*, 32, pp.1737-40.
- Rayleigh, L., 1880. On the stability or instability of certain fluid motions. *Proc. Lond. Maths. Soc*, 11, pp.57-70.
- Rockwell, D., 1983. Oscillations of impinging shear layers. *AIAA journal*, 21, pp.645-64.
- Rockwell, D. & Naudascher, E., 1978. Review: Self-sustaining oscillations of flow past cavities. *Journal of Fluids Engineering*, 100, pp.152-65.

- Rossiter, J., 1964. *Wind tunnel experiments on the flow over rectangular cavities at Subsonic and Transonic Speeds*. Technical Report 64037. Royal Aircraft Establishment.
- Rossiter, J. & Kurn, A., 1963. *Wind tunnel measurements of the unsteady pressures in and behind a bomb bay (T.S.R.2)*. Technical Report AERO.2677. Royal Aircraft Establishment.
- Sarohia, V. & Massier, P.F., 1997. Control of cavity Noise. *Journal of Aircraft*, 14, pp.833-77.
- Schachenmann, A. & Rockwell, D., 1980. Self-sustained oscillations of turbulent pipe flow terminated by an axisymmetric cavity. *Journal of sound and vibration.*, 73, pp. 61-72.
- Schmit, R.F. & Raman, G., 2006. High and low frequency actuation comparison for a weapons bay cavity. *International Journal of Aeroacoustics*, 5(4), p.395 – 414.
- Shaw, L.L., 1979. Suppression of aerodynamically induced cavity pressure oscillations. *Journal of the Acoustical Society of America*, 66(3), pp.880-84.
- Shaw, L., Clark, R. & Talmadge, D., 1988. F-111 generic weapons bay acoustic environment. *Journal of Aircraft*, 25(2), p.147–53.
- Smith, B.A.W. & Loluff, B.V., 2000. The effect of seat geometry on gate valve noise. *Pressure Vessel Technology*, 122, pp.401-07.
- Tam, C., 1974. Discrete tones of isolated airfoil. *Journal of the acoustical society of America*, 55, pp.1173-77.
- Tam, C.R.W. & Block, P.T.W., 1978. On the tones and pressure oscillations induced by flow over rectangular cavities. *Journal of fluid mechanics*, 89, pp.373-99.
- Tonon, D., Willems, J.F.H. & Hirschberg, A., 2011. Self-sustained oscillations in pipe systems with multiple deep side branches: Prediction and reduction by detuning. *Journal of Sound and Vibration* , 330, p. 5894–5912.

Valili, A. & Gauthier, C., 1994. Control of cavity flow by upstream mass injection. *Journal of Aircraft*, 31(1), pp.169-74.

Wilcox, J. & Floyd, J., 1988. Passive venting system for modifying cavity flow fields at supersonic speeds. *AIAA Journal*, 26(3), pp.374-76.

Ziada, S., 1994. A Flow visualization study of flow- acoustic coupling at the mouth of a resonant side-branch. *Journal of fluids and structures*, 8, pp.391-416.

Ziada, S. & Rockwell, D., 1982. Oscillation of an unstable mixing layer impinging upon an edge. *Journal of fluid mechanics*, 124, pp.307-34.

# Appendix A-Additional Results

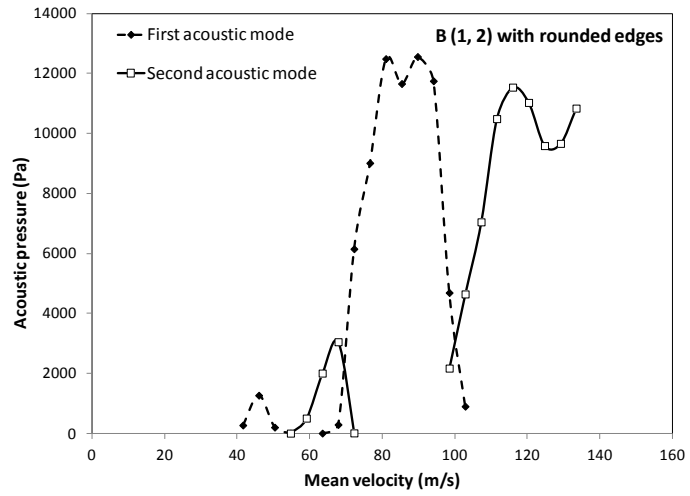


Figure A-1 Pressure amplitudes of excited acoustic modes at different flow velocities,  $d=25\text{mm}$ ,  $L/d=2$ ,  $d/D=2/12$ ,  $r/L=0.2$

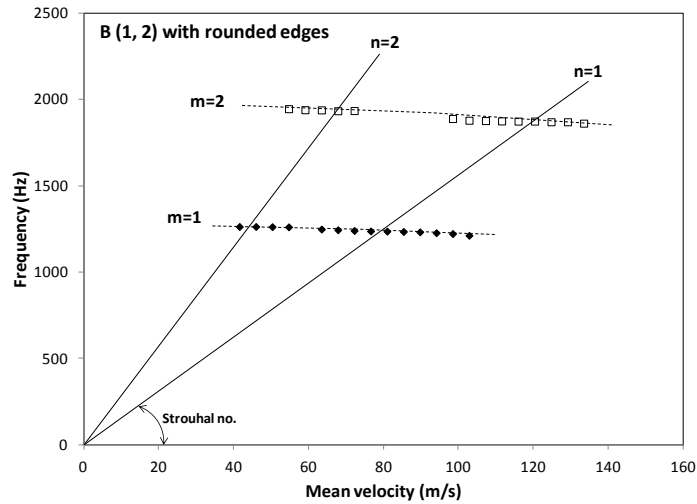


Figure A-2 Frequency of excited acoustic modes at different flow velocities,  $d=25\text{mm}$ ,  $L/d=2$ ,  $d/D=2/12$ ,  $r/L=0.2$

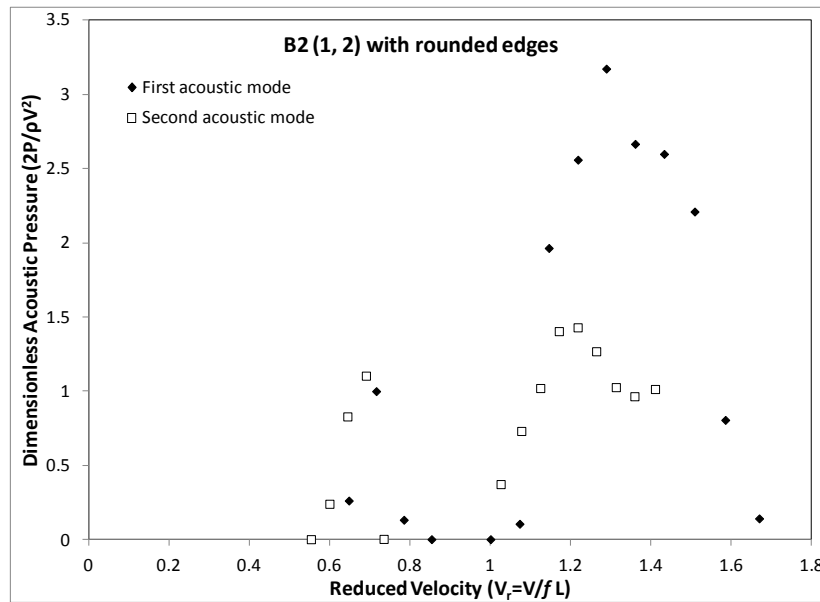


Figure A-3 Dimensionless acoustic pressures ( $P/\frac{1}{2}\rho V^2$ ) versus reduced velocity ( $V_r = V/fL$ ),  $d=25\text{mm}$ ,  $L/d=2$ ,  $d/D=2/12$ ,  $r/L=0.2$

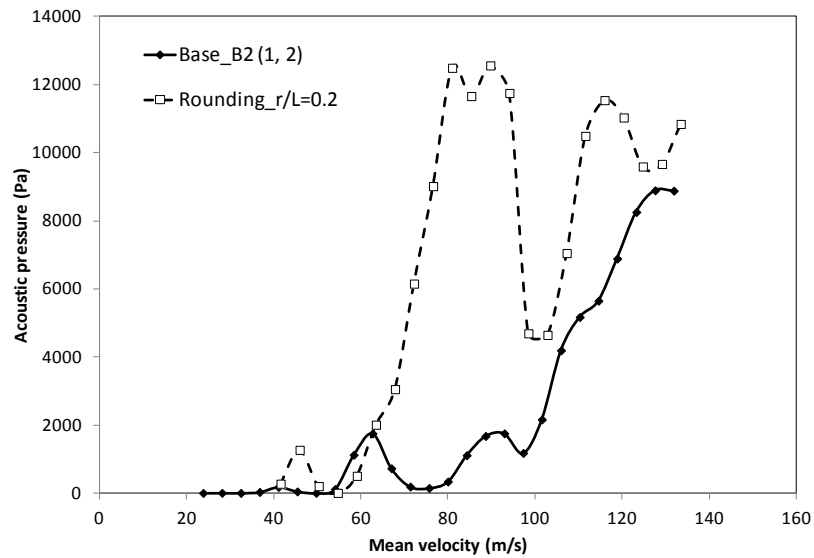


Figure A-4 Influence of rounding cavity edges on pressure amplitudes of excited acoustic modes at different flow velocities,  $d=25\text{mm}$ ,  $L/d=2$ ,  $d/D=2/12$ ; \_\_\_ base, ---- rounding

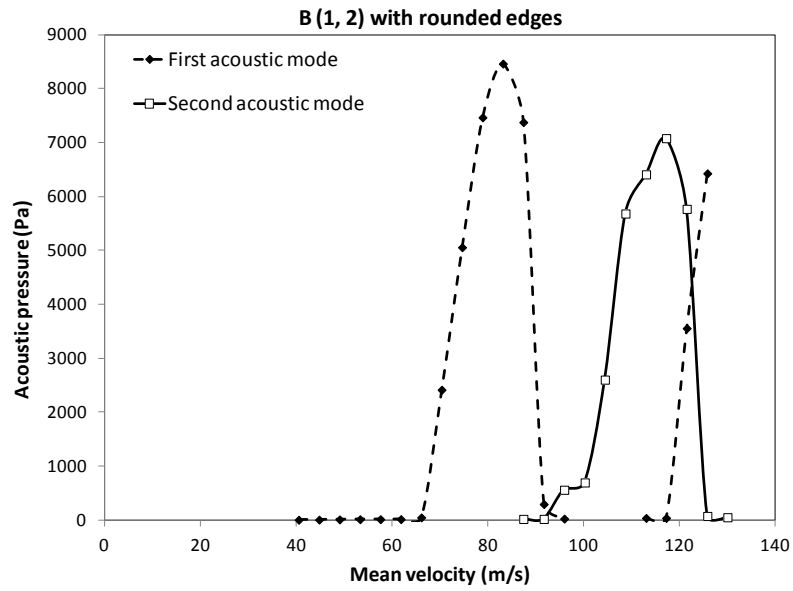


Figure A-5 Pressure amplitudes of excited acoustic modes at different flow velocities,  $d=25\text{mm}$ ,  $L/d=2$ ,  $d/D=2/12$ ,  $r/L=0.1$

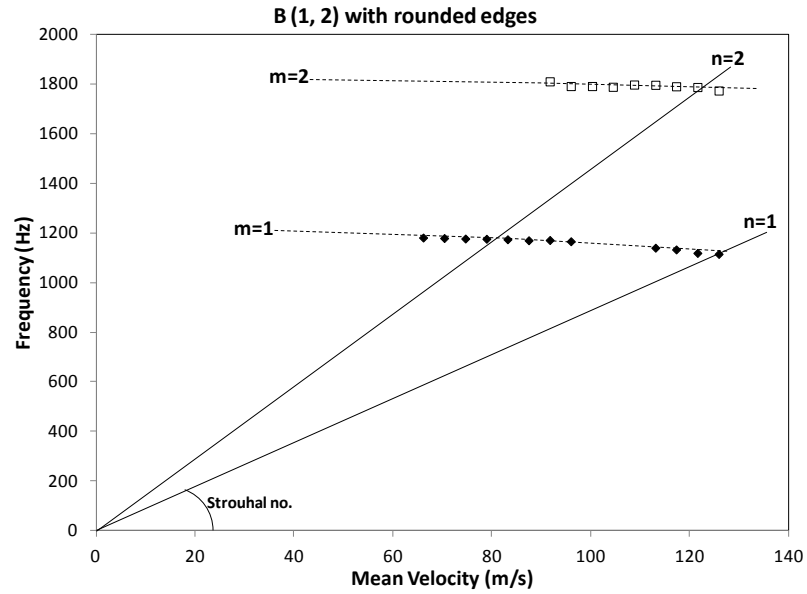


Figure A-6 Frequency of excited acoustic modes at different flow velocities,  $d=25\text{mm}$ ,  $L/d=2$ ,  $d/D=2/12$ ,  $r/L=0.1$

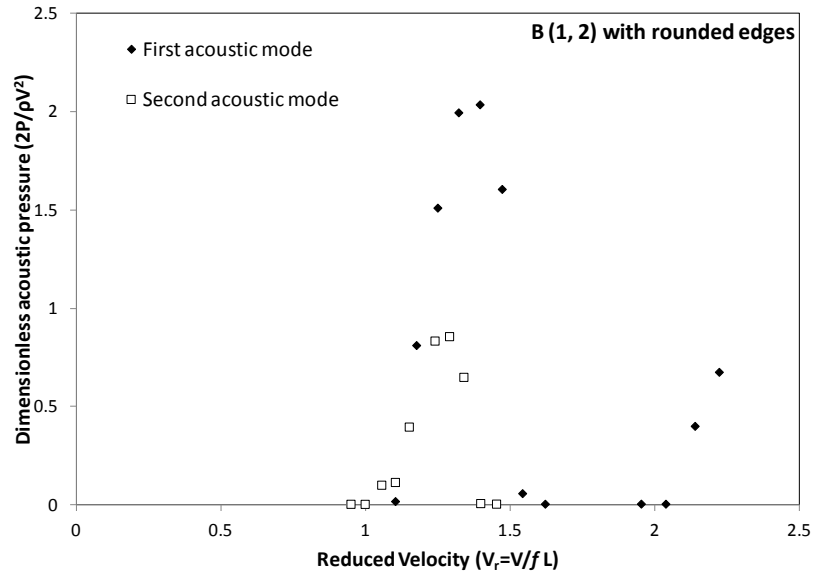


Figure A-7 Dimensionless acoustic pressures ( $P/\frac{1}{2}\rho V^2$ ) versus reduced velocity ( $V_r = V/fL$ ),  $d=25\text{mm}$ ,  $L/d=2$ ,  $d/D=2/12$ ,  $r/L=0.1$

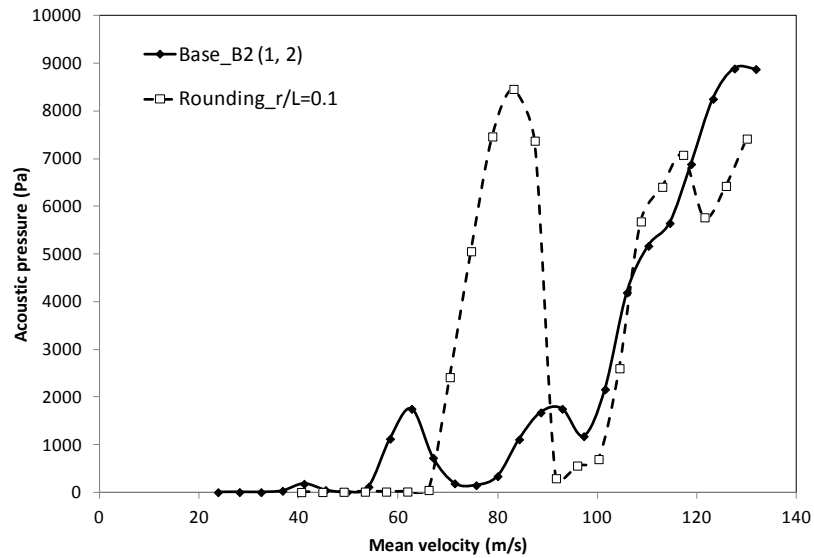


Figure A-8 Influence of rounding cavity edges on pressure amplitudes of excited acoustic modes at different flow velocities,  $d=25\text{mm}$ ,  $L/d=2$ ,  $d/D=2/12$ ; \_\_\_ base, ---- rounding

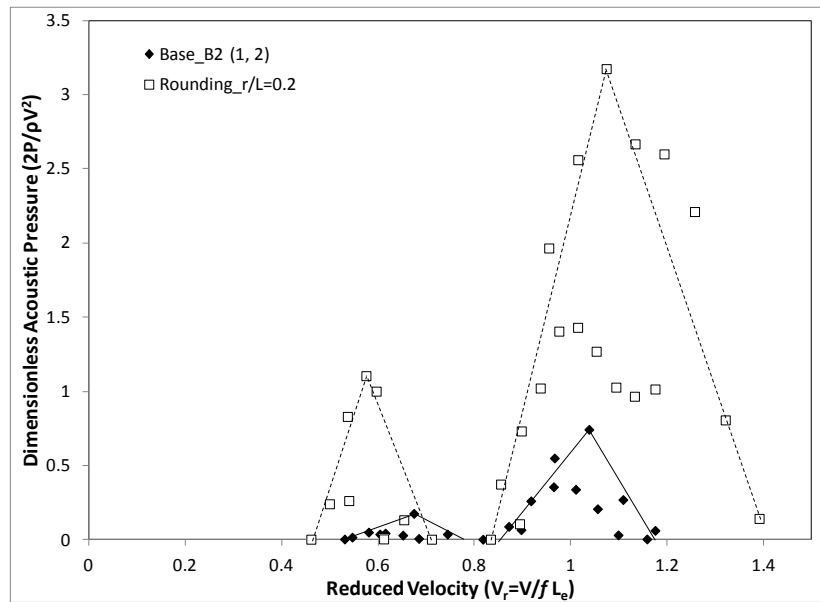


Figure A-9 Influence of rounding cavity edges on dimensionless pressure ( $P/\frac{1}{2}\rho V^2$ ) amplitudes of excited acoustic modes against reduced velocity ( $V_r = V/f L_e$ ),  $L_e = L + r$ ,  $d=25\text{mm}$ ,  $L/d=2$ ,  $d/D=2/12$ , \_\_\_ base, ----- rounding

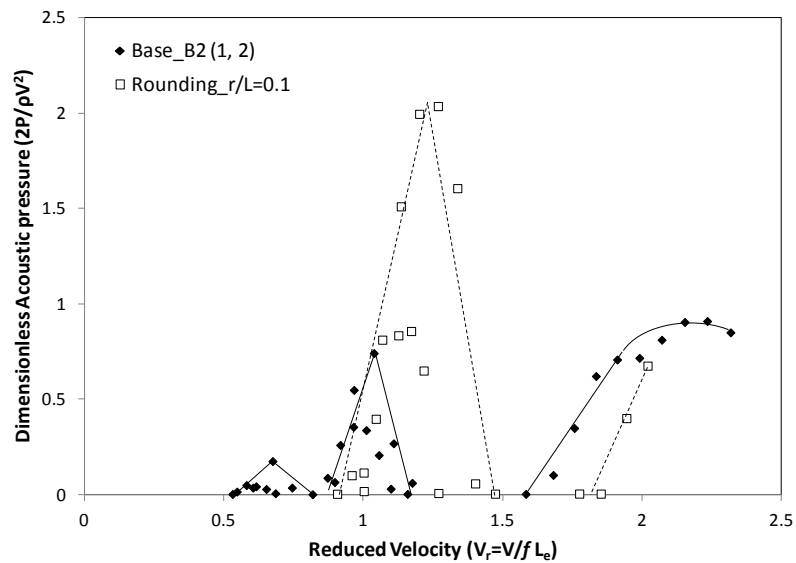


Figure A-10 Influence of rounding cavity edges on dimensionless pressure ( $P/\frac{1}{2}\rho V^2$ ) amplitudes of excited acoustic modes against reduced velocity ( $V_r = V/f L_e$ ),  $L_e = L + r$ ,  $d=25\text{mm}$ ,  $L/d=2$ ,  $d/D=2/12$ , \_\_\_ base, ----- rounding

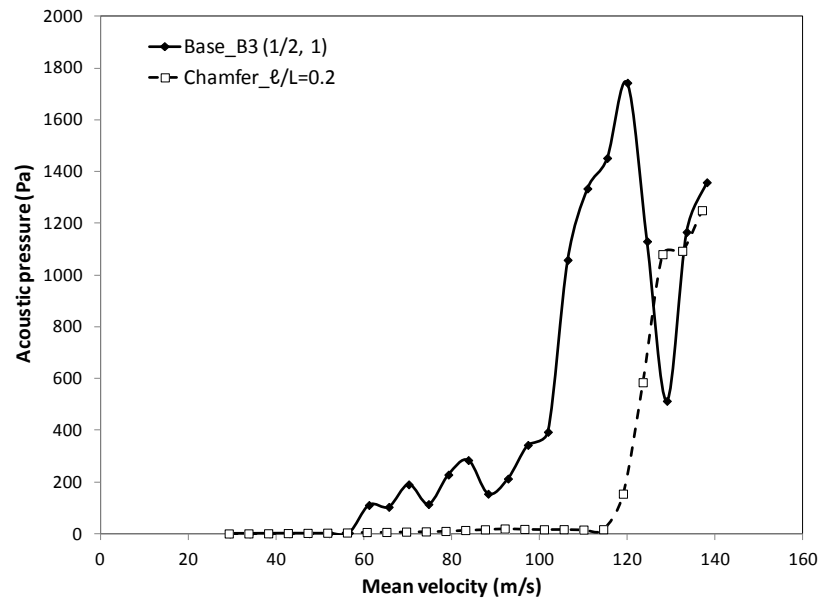


Figure A-11 Influence of chamfer on pressure amplitudes of excited acoustic modes at different flow velocities,  $d=12.5\text{mm}$ ,  $L/d=2$ ,  $d/D=1/12$ , \_\_\_base, - - - chamfer

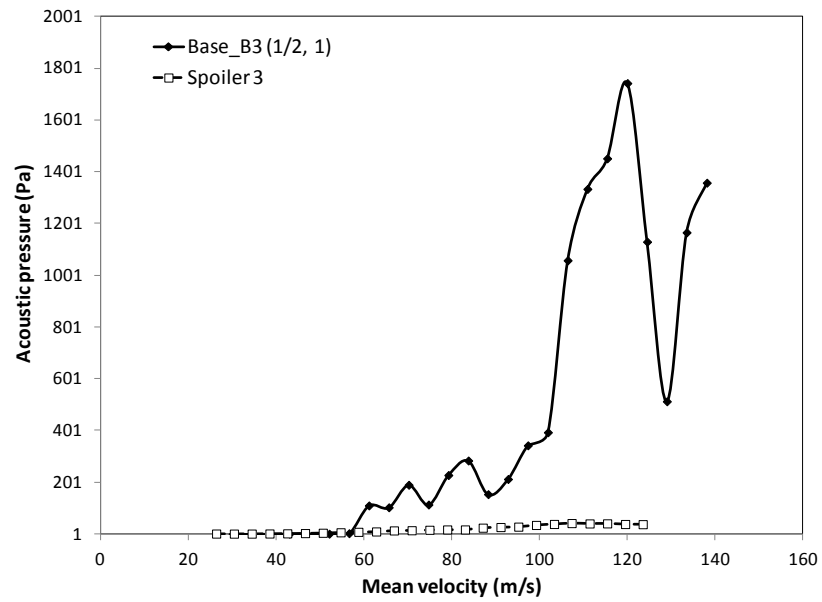


Figure A-12 Influence of spoiler (3) on pressure amplitudes of excited acoustic modes at different flow velocities,  $d=12.5\text{mm}$ ,  $L/d=2$ ,  $d/D=1/12$ , \_\_\_base, - - - spoiler

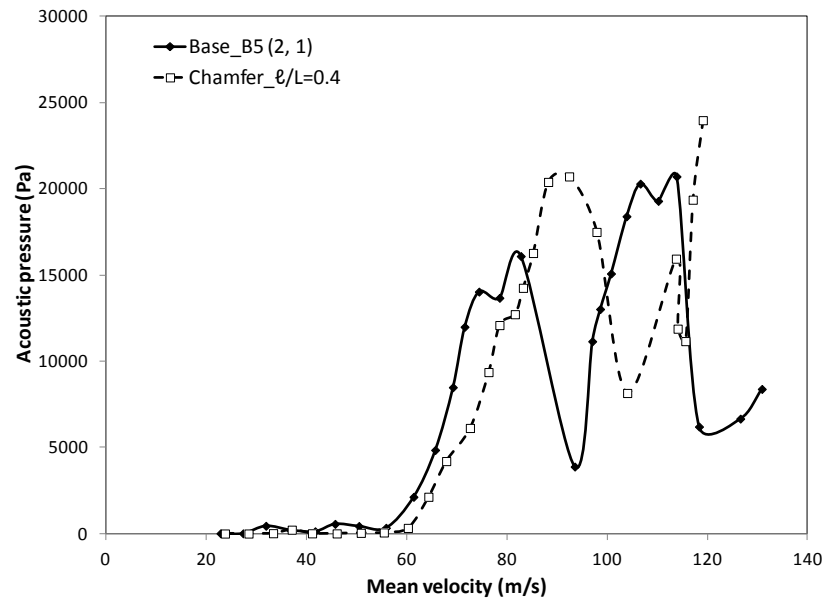


Figure A-13 Influence of chamfer on pressure amplitudes of excited acoustic modes at different flow velocities,  $d=50\text{mm}$ ,  $L/d=0.5$ ,  $d/D=4/12$ , \_\_\_base, - - - chamfer

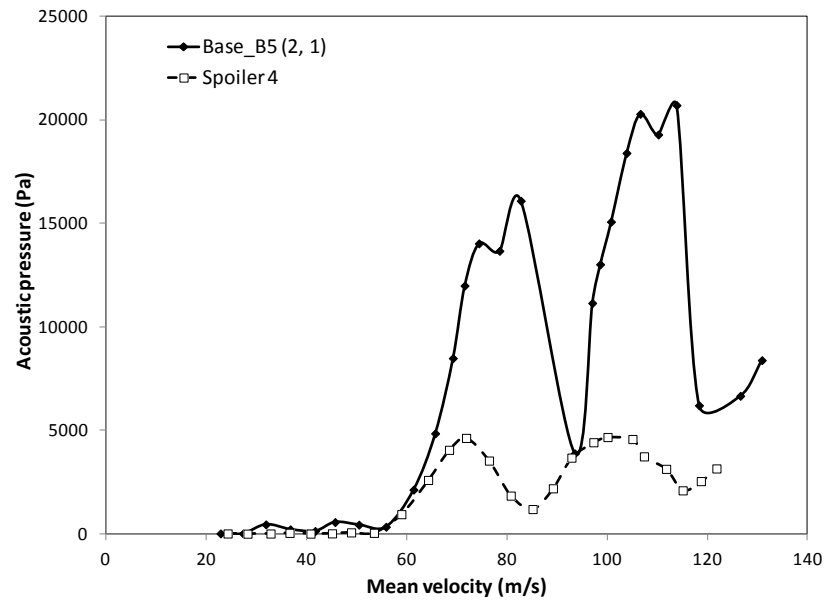


Figure A-14 Influence of spoiler (4) on pressure amplitudes of excited acoustic modes at different flow velocities,  $d=50\text{mm}$ ,  $L/d=0.5$ ,  $d/D=4/12$ , \_\_\_base, - - - spoiler

# Appendix B

## Uncertainty Analysis

---

This appendix provides the uncertainties accompanying the calculation and measurement of different quantities. When these uncertainties become systematic, they are considered small in comparison to the precision of the measurements. Based on Kline and McClintock method for calculation of the random uncertainty, the propagation uncertainty is given by:

$$\delta Y = \sum_{i=1}^n \sqrt{\left(\frac{\partial Y}{\partial X_i}\right)^2} \delta X_i \quad \text{B— 1}$$

Where  $\delta Y$ , is the uncertainty of the dependent variable  $Y$  and  $\delta X_i$ , is the uncertainty of the independent variable  $X_i$ .

For the acoustic pressure measurements, the uncertainty comes from the calibration, the resolution of the pressure transducers and the repeatability in measurements. So the maximum values found during measurements were approximately 4%, 3%, and 5% for calibration, resolution of the pressure transducers and repeatability, respectively. This would result in 7% uncertainty in acoustic pressure when adding these maximum uncertainty values by quadratic summation.

A pitot tube is used to measure mean flow velocity. The pitot tube is connected to differential pressure transducer which has 2% uncertainty calibration. This would lead to 1% uncertainty of velocity measurements. In addition, the standard of deviation in the averaged values from pitot tube is 0.5%. As a result, the mean flow velocity has uncertainty in the range of 1.5%.

Dimensionless acoustic pressure ( $P^* = P^{1/2} \rho V^2$ ) has uncertainty attributed to the uncertainties of acoustic pressure and mean flow velocity. This is given by:

$$\frac{\delta P^*}{P^*} = \sqrt{\left(\frac{\delta P}{P}\right)^2 + \left(2 \frac{\delta V}{V}\right)^2} \quad \text{B - 2}$$

Accordingly, the uncertainty of dimensionless acoustic pressure is 7.5%.

The Strouhal number ( $St = fL/V$ ) is a function of frequency  $f$ , cavity length  $L$ , and mean flow velocity  $V$ . So the uncertainty of Strouhal number is based on the uncertainty of these parameters, and this can be calculated from:

$$\frac{\delta St}{St} = \sqrt{\left(\frac{\delta f}{f}\right)^2 + \left(\frac{\delta L}{L}\right)^2 + \left(\frac{\delta V}{V}\right)^2} \quad \text{B - 3}$$

The minimum resonance frequency in this study is 900 Hz. Also, the resolution of the frequency is 1Hz. So the uncertainty of the frequency is 0.1%. And the cavity length has 1% tolerance. This would give 1.8% uncertainty in Strouhal number.